Applications of perturbation theory in high energy electron diffraction

James, Richard

Award date:
1990

Awarding institution:
University of Bath

APPLICATIONS OF PERTURBATION THEORY IN HIGH ENERGY ELECTRON DIFFRACTION

submitted by Richard James
for the degree of Doctor of Philosophy
of the University of Bath

1990

COPYRIGHT

ProQuest LLC
789 East Eisenhower Parkway
P.O. Box 1346
Ann Arbor, MI 48106-1346

ABSTRACT

This thesis contains two examples of the use of perturbation theory in high energy electron diffraction (HEED). In both cases, information which is hidden in more conventional, fully dynamical calculations is obtained directly from electron micrographs.

Chapter 1 gives a brief introduction to the advantages and disadvantages of HEED as a crystallographic probe. Chapter 2 then contains a derivation of the usual starting equations for HEED, highlighting the approximations and assumptions generally made. These equations are in the form of a low-energy Schrödinger equation, which is then written in appropriate representations for both the numerical and approximate solutions given in Chapters 3 and 4.

Chapter 3 presents a solution to the phase problem of crystallography. A second-order Born expansion of diffracted amplitudes in the three-beam geometry is inverted to give a simple prescription for the measurement of phase triplets in centrosymmetric and non-centrosymmetric crystals. The validity of the approximations made is discussed, and the method is tested for a known, simple non-centrosymmetric structure.

Chapter 4 contains a discussion of "surface resonance" features observed in reflection-HEED (RHEED) patterns. The geometry of these patterns is explained for the first time, by comparison with off-axis transmission patterns from similar orientations. Much of this analysis centres around two-rod perturbation theory, through which it is deduced that most features in 200kV RHEED patterns are not very surface sensitive. A study is also presented of the true nature of the "resonance" and intensity-enhanced features seen in these patterns.

Chapter 5 is the conclusion.

ACKNOWLEDGEMENTS

There are several people who have helped me a great deal with the work presented in this thesis. All of the experimental patterns shown (and many more not shown) were taken by others, usually at my request. For these (as well as for many useful discussions) I am particularly indebted to Andy Wright, and also to Alasdair Preston.

I should also like to thank the members of the School of Physics collectively for their friendship and assistance throughout my stay in Bath. Their contributions to my work have been large and small, direct and indirect, and I am grateful for them all. Thanks are also due to the SERC for (limited) financial assistance, and to the School and University for (unlimited) use of computing and other facilities.

However, my main reason for writing acknowledgements is to thank David Bird. His enthusiastic supervision and discussion have been by far the greatest influence upon the work presented here. His attitude and approach to tackling problems has been instructive and infectious. David has also given a great deal of time to careful reading of draft versions of this thesis. I am sincerely grateful for his help and friendship, and hope that both will continue.

Finally, I should like to stress that despite the assistance of others in this work, the full responsibility for any faults and errors it may contain is mine.

CONTENTS

Chapter 1

INTRODUCTION

The X-ray and the neutron are by far the most useful probes of the solid state available to the crystallographer. Almost all work in solving crystal structures makes use of one or both of them (see for example Bacon 1975, Ladd and Palmer 1977). By contrast, the use of the electron as a crystallographic probe is not nearly so common. This is primarily because electrons, being charged, interact strongly with the crystal, so it is almost inevitable that an incident electron will be scattered more than once (and usually many times) before it leaves the specimen. Thus, although an electron diffraction pattern will contain at least as much information as an X-ray pattern, that information will not be nearly so easy to recover.

There are, however, certain features of electron diffraction which make it a potentially useful crystallographic tool. The most important of these is that an electron beam can easily be focussed to form a very small probe, perhaps only a few tens of Ångstroms across in a modern conventional transmission electron microscope (TEM). This means that electron diffraction patterns can be taken from small, local areas of a specimen. Further, since it is possible to image the region of interest in an electron microscope, these small areas can be chosen in a controlled manner. Thus it is possible to study single domains, small precipitates, defect-free single-crystal regions and so on. Such versatility is not possible using X-rays or neutrons, since both tend to produce a probe

which is physically rather large (~mm),† so the information will be averaged over many grains, defects and so on, if the specimen is not a perfect single crystal. Also, since electrons do not penetrate very far into a solid, they may be a more useful tool for surface physics. Much work has been done using low energy electron diffraction (LEED) at surfaces (see Pendry 1974 for an excellent account of LEED), and to a lesser extent using electrons at kilovolt energies in reflection high energy electron diffraction (RHEED) [the papers in Larsen and Dobson (1988) give a good résumé]. Finally, there may be situations in which electron diffraction simply offers a better method of obtaining information that is either obscured or not available using other techniques.

In this thesis two topics of current interest in high energy electron diffraction (HEED) are approached; one in transmission (THEED) and one in reflection (RHEED). In both cases perturbation theory is used to give a clear physical picture of the diffraction involved. Discussions on the applicability of the approach taken will be left until each example has been introduced, but it should be mentioned here that in both cases particularly appropriate experimental geometries have been used to advantage. In the THEED example, the perturbation approach leads to new and useful crystallographic information which may be deduced directly and simply from an electron micrograph. This study forms the content of Chapter 3. In the reflection example, described in Chapter 4, perturbation theory is used to gain a simple picture of the scattering processes

† Synchrotron sources of X-rays may produce micron-sized probes, but the lack of an imaging facility means that the position of the probe cannot be well controlled.

responsible for features in RHEED patterns, particularly those associated with "surface resonance".

The experimental data which will be analysed are all taken from convergent-beam electron diffraction (CBED) patterns. In CBED, the microscope lenses are adjusted so that a convergent cone of electrons, rather than a parallel beam, is directed towards the specimen. Figure 1.1 shows a schematic of this for the case where the incident beam is focussed on the top surface of a transmission specimen. It is usual (eg Carpenter and Spence 1984) to assume that the probe consists of a set of *independent plane waves* $\exp(i\mathbf{k}.\mathbf{r})$. In truth these waves cannot be completely independent, or it would be impossible to form a focussed probe at all. Thus it is convenient to consider the probe as consisting of a set of mutually independent "pencils" of coherent electrons (see figure 1.1), each associated with a small range of wavevectors about the plane wavevector $\mathbf{k}$. Electrons pass through the specimen, undergoing both coherent scattering events (such as Bragg diffraction) and incoherent events (such as most phonon scattering).

The principal coherent effect of the crystal on the incident plane waves is to Bragg diffract them by reciprocal lattice vectors $\mathbf{g}$. Since each of the incident wavevectors $\mathbf{k}$ is independent of the others, a CBED pattern consists of a set of discs, separated by the vectors $\mathbf{g}$, where similar points within each disc (marked by crosses in figure 1.1) are associated with an individual incident orientation, determined by the direction of the wavevector $\mathbf{k}$. These discs are the CBED equivalent of diffraction spots in a parallel-illumination experiment.

In a sense, then, convergent-beam patterns are a mosaic of the Bragg spot pat-

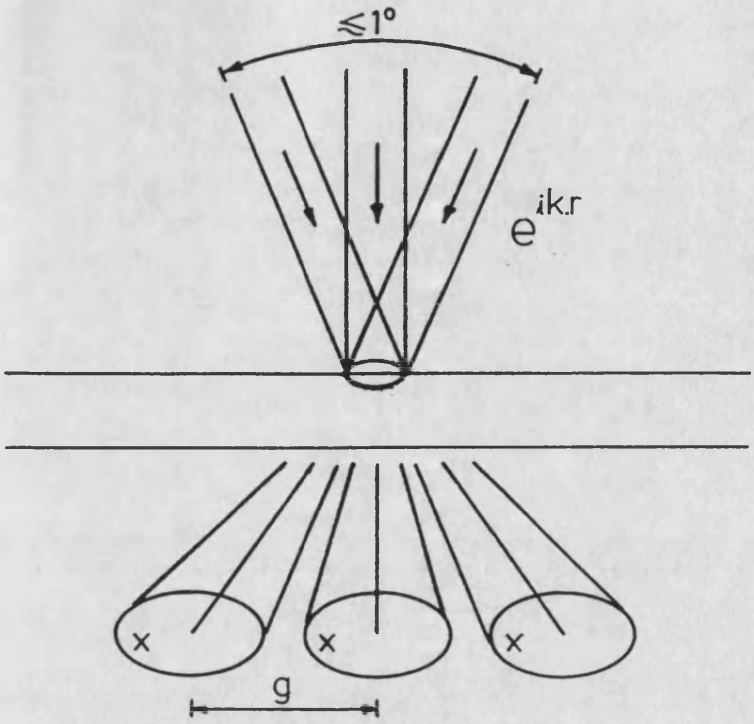

Figure 1.1 Schematic of pencils of coherent radiation combining to form a convergent beam probe, and a crystal specimen diffracting such a probe into discs. Note that the angular width of the incident cone is typically less than, or of the order of 1°.

terns we might expect from each, nearly-parallel pencil of radiation, and as such contain a wealth of information. Indeed, many of the successes of electron diffraction in crystallography have been achieved using CBED techniques. Some of these successes in transmission work have been in the determination of crystal point- and space-groups (Buxton *et al.* 1976), in local lattice strain measurements (eg Jones, Rackham and Steeds 1977, Steeds 1979), in the successful measurement of electronic structure factors (see Zuo, Spence and O'Keeffe 1988, Zuo, Spence and Høier 1989 and Chapter 3), and in the determination of one or

two crystal structures (Vincent, Bird and Steeds 1984a,b).

At first sight, the analysis of HEED would appear to be particularly difficult. A typical incident electron considered here will have kinetic energy ~200keV. Thus, since the electron rest mass is 511keV, the starting point of the analysis should be Dirac's relativistic wave equation (see eg Dirac 1958). In addition, the construction of the scattering potential is far from easy, since in principle it should account for the interaction of a single fast electron with all the individual constituents of the crystal specimen. It is therefore impractical to try and find exact solutions.

Fortunately, it has long been known that most of these difficulties can, to a good approximation, be overcome. As will be discussed in Chapter 2, the most important features of the scattering potential can be incorporated into a local, periodic, single-particle optical potential $V(\mathbf{r})$. Also, if it is assumed that all the scattering is through small angles (as it will be in our applications), the spin effects inherent in the Dirac equation may be ignored, to leave a rather simple starting equation (Fujiwara 1961,1962) which is scalar and identical in form to the low-energy Schrödinger equation. This huge simplification means that all the familiar techniques of single-particle, low-energy quantum mechanics will be at our disposal in the analysis of HEED. It also means that, quite apart from its practical uses, the electron microscope is a splendid environment in which to test the predictions and see the effects of quantum mechanics. As a nice example, much interest has been shown in the geometrical phase factor (Berry 1984) by which a wavefunction is modified under the influence of a slowly varying Hamiltonian. This is a quantum mechanical effect which may be observed (Bird

and Preston 1988) in a diffraction pattern as producing fringe-bending where the incident electrons have their trajectories varied slowly by the bent planes surrounding a dislocation.

As already stated, the major difficulty that cannot normally be bypassed is that the fast electrons are likely to be multiply scattered on their path through a specimen. The quantities of main interest are the amplitudes $A_{\mathbf{g}}$ of the beams Bragg diffracted by the vectors g of the crystal's reciprocal lattice, at the point of exit from the specimen. Due to multiple scattering, there is a dynamical interaction between the states associated with the various g involved (see Chapter 2), so that in general the expressions for the diffracted intensities as a function of incident orientation k and crystal thickness t

$$I_{\mathbf{g}}(\mathbf{k},t) = |A_{\mathbf{g}}(\mathbf{k},t)|^2 \quad . \tag{1.1}$$

(which are of course the quantities observed in experiment) are a complicated mixture of many components. These expressions are therefore not *invertible*; although it is possible to construct a "forward going" theory which successfully predicts the intensities if all the relevant crystal parameters are known, it is in general impossible to go "backwards" and deduce all those parameters from the measured intensities.

There are essentially two ways in which these parameters may be found from experiment. The first is to treat them as variables in a fitting procedure, whereby each is varied independently until the "forward going" intensities match the experimental ones. Unfortunately, it is rarely the case that the only fit parameter is the parameter of interest, so that in practice fitting methods can become

rather laborious to perform. For example, the successful determination of surface structures using these forward-going fitting procedures in LEED is likely to require the numerical simulation of many thousands of possible structures (Pendry 1974).

The alternative approach to this "inverse problem" is to invert approximate expressions for the diffracted intensities. Although this is not a possibility for the analysis of a whole diffraction pattern, it may be that certain features or areas can be chosen in which the diffraction conditions are simplified, so that a completely rigorous approach is not necessary. Such selective analysis is at the heart of the CBED work mentioned earlier. For example, the *symmetry* of CBED patterns is directly related to the symmetry of the crystal, so that space and point groups may be deduced without reference to the intensity values themselves. Since a single CBED pattern contains information from many incident orientations, it has been found that this is one of the best methods there is for symmetry determination (eg Buxton *et al.* 1976). Similarly, the lattice strain measurements are based on an approximate relationship between the relative positions of lines in a CBED pattern and the lattice parameters of the crystal. Although a fitting procedure is then required to deduce the strain, it is a positional rather than an intensity fit, and is therefore relatively easy to perform.

The method adopted in this thesis is to use perturbation theory to derive approximations to the exact diffraction equations in local areas of a CBED pattern. In particular, we shall construct the total diffracted amplitudes using a Born expansion (eg Cowley 1981), considering first the kinematic, single scat-

tering contribution, then the double scattering contributions and so on, until it is apparent that the effects caused by the parameter or feature of interest will be included (to lowest order) in the resulting intensity expression. In some cases, where only the *cause* of a diffraction feature is of interest (see especially Chapter 4), the derivation of such an expression may well lead to a physical understanding of the phenomenon which could not so easily be gleaned from a numerical forward-going technique. Where quantitative information is required, it is hoped that the approximate intensity expression may be inverted to yield explicit formulae for the desired parameter in terms of measurable quantities. These measured parameters may then be used as starting guesses in a fitting procedure, should refinement be required.

As all our analysis will be concerned with approximation methods, Chapter 2 contains a discussion of the assumptions and approximations made in constructing the optical potential $V(\mathbf{r})$ and in deriving the HEED starting equations. Three well documented representations of these equations are then introduced; one of these (the many-beam equations) is not in general invertible, but is of considerable use in making numerical comparison with our approximations. The other two representations are both amenable to perturbation expansion and are appropriate for transmission (the Howie-Whelan equations) and reflection (the Kambe equations) respectively. The chapter is concluded with an introduction to the geometry and general features of the type of CBED patterns used throughout.

Chapter 3 contains an analysis of a transmission diffraction situation in which only three independent beams make significant contributions to the diffracted

amplitudes. It is shown that even this situation is non-invertible in its full dynamical form, but that an analysis based on a second order perturbation expansion does lead to a prescription for the measurement of so-called crystallographic phase invariants. The measurement of such invariants constitutes the best possible solution to the "phase problem of crystallography", as will be explained. The prescription derived for finding these invariants is tested experimentally for a noncentrosymmetric crystal with a known, simple structure.

Chapter 4 uses a distorted-wave Born approximation (eg Schiff 1968) to investigate and explain the geometry and nature of surface resonance lines in convergent beam RHEED patterns taken at an accelerating voltage of 200kV. In this case perturbation theory offers an explanation of the physical processes responsible for the phenomenon which is masked in the numerical analysis of others. Much of the initial explanation of these RHEED features is in fact found by analogy with geometrically similar THEED patterns, which are rather easier to interpret. A comparison between equivalent THEED and RHEED patterns taken from the same (well-understood) materials then leads to a discussion of the surface-sensitivity of RHEED patterns.

Chapter 5 is the conclusion.

Chapter 2

HIGH ENERGY ELECTRON DIFFRACTION

This chapter contains a derivation of the equations that have become the conventional starting point for the dynamical theory of electron diffraction. Particular attention will be paid to the assumptions and approximations made in the derivation, and in the construction of the scattering potential. Having established the notation which will be used throughout the thesis, three representations of the diffraction equations will then be derived which are of particular use in the remaining chapters. Finally, an attempt will be made to explain in rather general terms the geometry of the type of CBED patterns analysed in these later chapters.

2.1 CONSTRUCTION OF THE SCATTERING POTENTIAL

As mentioned in Chapter 1, the crystal potential seen by an incident electron should in principle include the effects from every crystal electron and nucleus, both as individual scatterers and as part of collective excitations. Fortunately, there are features of HEED which make the construction of a realistic and usable scattering potential somewhat easier than might at first be expected. The first of these is that the incident electron is distinguishable from the crystal electrons, by virtue of its high kinetic energy (typically 200keV). This means that the probability of exchange between an incident electron and a crystal electron is negligible, so exchange effects can be ignored completely in our scattering potential V (eg Dederichs 1972). This is a particularly useful simplification since

exchange is non-local (eg Ashcroft and Mermin 1976).

The second useful feature of HEED is that the majority of scattering events are found to be elastic and contribute to the intensity diffracted into Bragg beams. It is these Bragg beams which contain nearly all the information of interest in crystallography, so most of the important details may be incorporated by the construction of a fairly simple periodic potential. In so doing we shall ignore (for the present) the effect of the inelastic scattering events. Although they are less frequent than elastic events, their most important effect is to redistribute electrons among the Bragg beams, and into a "diffuse background" between beams. This redistribution, for which it is difficult to establish a good model, distorts the useful information carried by the Bragg-diffracted electrons, and thus puts an effective limit on the accuracy which can be expected from quantitative electron crystallography. We shall return to inelastic scattering at the end of this section.

Let us first construct the basic periodic potential responsible for Bragg diffraction. It will be assumed that the crystal is perfectly periodic, and to begin with, rigid and static. It is found in practice that the electrons involved in bonding are almost undetectable in HEED experiments (Zuo, Spence and O'Keeffe 1988), so an accurate static potential can be constructed from a sum of the individual neutral atom potentials:

$$V(\mathbf{r}) = \sum_{\mathbf{l}} \sum_{\kappa} v_{\kappa}^{\circ}(\mathbf{r} - \mathbf{l} - \mathbf{r}_{\kappa}), \qquad (2.1.1)$$

where the $\mathbf{l}$ are the lattice vectors, and $\mathbf{r}_{\kappa}$ is the position of the κ^{th} atom in the unit cell. [Unless stated otherwise, 3-dimensional vectors will be written in

lower case script. Thus $\mathbf{r}$ is a 3-dimensional position vector. Later we shall use upper case script to denote 2-dimensional vectors.] The potentials $v_\kappa^\circ(\mathbf{r})$ may be obtained from the electronic and nuclear charge densities of the individual atoms by solving Poisson's equation (eg Ashcroft and Mermin 1976).

Since we are interested in Bragg diffraction, it is most natural to express the periodic potential V in reciprocal space. Thus V is written as the Fourier series

$$V(\mathbf{r}) = \sum_{\mathbf{g}} V_{\mathbf{g}} \exp(i\mathbf{g}.\mathbf{r}) \tag{2.1.2}$$

with

$$V_{\mathbf{g}} = \frac{1}{\Omega_c} \int_{\Omega_c} V(\mathbf{r}) \exp(-i\mathbf{g}.\mathbf{r}) d^3\mathbf{r}, \tag{2.1.3}$$

where the $\mathbf{g}$ are reciprocal lattice vectors and Ω_c is the volume of the unit cell. Note that $|\mathbf{g}| = 2\pi/d$ where d is the appropriate spacing between lattice planes. Bragg diffraction causes the wavevector $\mathbf{k}$ of an electron to be changed elastically by a reciprocal lattice vector $\mathbf{g}$:

$$\mathbf{k} \longrightarrow \mathbf{k} + \mathbf{g}. \tag{2.1.4}$$

The strength of these transitions is governed by the $\mathbf{g}$th "structure factor" $V_{\mathbf{g}}$. From (2.1.1)-(2.1.3) it is found that

$$V_{\mathbf{g}} = \sum_{\kappa} v_\kappa^\circ(\mathbf{g}) \exp\left(-i\mathbf{g}.\mathbf{r}_\kappa\right), \tag{2.1.5}$$

where the "atomic form factors" $v_\kappa^\circ(\mathbf{g})$ are essentially the Fourier transform of the atomic potentials $v_\kappa^\circ(\mathbf{r})$, and are, apart from a few scaling factors, the quantities tabulated by Doyle and Turner (1968), Smith and Burge (1962) and others. Most HEED calculations use these tabulated atomic form factors as the basis of a scattering potential.

Of course it is not the case in practice that a crystalline specimen will be perfectly periodic and static. It will be assumed throughout that it is possible experimentally to find defect-free regions, so non-periodicity in this sense will be of no concern. What cannot be ignored is that at finite temperatures each ion will vibrate about its equilibrium position. Other features which will also contribute are the collective excitation of the ions (phonons) and electrons (plasmons), and electronic transitions within individual atoms.

Most of these scattering processes contribute to the inelastically scattered flux; the exception is the contribution from averaged ionic vibrations (Radi 1970, Dederichs 1972). Let us assume that the mean equilibrium position of each ion is the same as for the static lattice, and that the deviation of the atom κ at lattice site $\mathbf{l}$ is $\mathbf{u}_{\mathbf{l}\kappa}(t)$ and is small compared with interionic spacings. We may then work within the harmonic approximation (Ashcroft and Mermin 1976) to produce a simple analytical correction to the atomic form factors. With this additional displacement included, the incident electrons will see a thermally averaged elastic potential

$$V_{\mathbf{g}} = \sum_{\kappa} v_{\kappa}^{\circ}(\mathrm{g}) \exp(-i\mathbf{g}.\mathbf{r}_{\kappa}) \langle \exp(-i\mathbf{g}.\mathbf{u}_{\mathbf{l}\kappa}) \rangle. \qquad (2.1.6)$$

If it is further assumed that the ionic vibrations are isotropic about the equilibrium positions, then the thermal averaging term $\langle\rangle$ may be written as (eg Dederichs 1972)

$$\langle \exp(-i\mathbf{g}.\mathbf{u}_{\mathbf{l}\kappa}) \rangle = \exp(-M_{\kappa} g^2). \qquad (2.1.7)$$

This whole term is referred to as the Debye-Waller factor. The temperature-dependent part of the factor, M_{κ}, is usually not named, but will be referred to as

the Debye-Waller figure in this thesis. In the notation used here, $M_\kappa = \frac{1}{2}\langle u_{1\kappa}^2 \rangle$. Effective atomic form factors may then be written as

$$v_\kappa(\mathbf{g}) = v_\kappa^\circ(\mathbf{g}) \exp(-M_\kappa g^2) \tag{2.1.8}$$

and these can be used in an elastic scattering potential which takes into account the average thermal motion of the ions. It should be noted that the $v_\kappa^\circ(\mathbf{g})$ are themselves rapidly decreasing functions of g, ($\propto g^{-2}$ at large g - see Doyle and Turner 1968) so that the structure factors $V_\mathbf{g}$ are strongest for the shortest reciprocal lattice vectors, and diffraction through large angles is much weaker than through shallow angles.

So far, then, we have considered the elastic processes. These have been described using a real potential $V(\mathbf{r})$, which contributes to an hermitian Hamiltonian. In §2.3 it will be shown that this leads to flux conserving solutions of the diffraction equations. The other processes mentioned are all inelastic and may cause flux to be lost from Bragg beams (and the experiment as a whole if electrons are scattered out of the microscope apertures). As in optics, these effects may be described using an imaginary part of the crystal potential $iV'(\mathbf{r})$ (Yoshioka 1957), which renders the Hamiltonian non-hermitian, and hence leads to a loss of flux. Because of this loss, $iV'(\mathbf{r})$ is usually referred to as an absorptive potential, even though no electrons have physically been absorbed by the crystal.

Unfortunately, most of the absorptive contributions to the optical potential are extremely difficult to calculate (eg Dederichs 1972), because they tend to be non-local and cannot in general be constructed from individual atomic contributions. Instead they must be found, for example, by first principles calculations

of the electronic structure or the phonon spectrum of a particular material (Bird and King 1990). For this reason, it has become established practice to assume that the imaginary part of the potential is equal to one tenth the real part (Hashimoto, Howie and Whelan 1962), and to treat it as a perturbation in the electron wavefunction eigenvalues. Thus absorption is treated in a phenomenological manner, if at all, and the accuracy obtainable in quantitative electron crystallography is limited. Although it would be preferable to include these effects, the pragmatic advantage of ignoring them at this stage is that with a local scattering potential the Dirac equation remains manageable (see §2.2).

It is convenient to discuss the inelastic scattering of HEED electrons in terms of two basic types of absorption; mean and anomalous. The first, described by the Fourier component $V_{\mathbf{0}}'$, attenuates all the Bragg beams uniformly, and does not therefore cause unwanted redistribution. A large component of $V_{\mathbf{0}}'$ arises from partially coherent plasmon scattering (Howie 1963) and is consequently rather difficult to calculate. In Chapter 4 it is shown that this can cause a major difficulty in RHEED, since different beams have a different path-length inside the crystal and are therefore attenuated by different amounts, even through "mean" absorption. By contrast, in the simplest THEED geometry, with a parallel-sided specimen, all paths through the specimen are approximately the same length, so only the absolute intensities in each beam, and not the relative intensities, are affected. For this reason, methods which rely on the measurement of absolute intensities should be avoided if possible.

It is generally accepted (Dederichs 1972) that the biggest contribution to anomalous absorption, described by the components $V_{\mathbf{g}\neq\mathbf{0}}'$, comes from thermal diffuse

scattering (TDS). This arises from the unaveraged scattering of electrons from vibrating ions. In the simplest (Einstein) model, that of independently vibrating ions, the TDS contribution to $V'_{\mathbf{g}}$ can be described in terms of an integral (Hall and Hirsch 1965) for each atomic component. Although the integral must be evaluated numerically, it is general for all materials (in the limit of harmonic, isotropic vibrations). Humphreys and Hirsch (1968) and Radi (1970) have produced values of the integral for a few specific cases. More recently, Bird and King (1990) have evaluated the integral as a function of the two parameters M_κ and $|\mathbf{g}|$ for all the neutral atoms treated elastically by Doyle and Turner (1968). Thus the atomic scattering may now be expressed in terms of a real, elastic form factor and an imaginary form factor due to TDS in the Einstein model. The results of Bird and King show that $V'_{\mathbf{g}}$ is not proportional to $V_{\mathbf{g}}$, and that in a noncentrosymmetric crystal, the two will not necessarily be in phase. The Bird and King form factors will be used in a semi-quantitative analysis of absorption in both the applications studied in later chapters. Of course, we cannot be fully quantitative due to the neglect of the correlated ionic (phonon) and core excitation contributions to V'. We trust that these will be less important than the TDS included, and that the TDS calculations will give at least some idea of the effect of inelastic scattering in our analysis.

2.2 THE HEED EQUATIONS

The starting equations for the analysis of HEED patterns will now be derived. It will be assumed that the scattering of interest can be described using a local, elastic potential $V(\mathbf{r})$, and that inelastic processes will only be treated after-

wards to give a measure of the reliability of our results. The total energy E of the incident electrons is therefore a conserved quantity, so it is a *scattering* problem which must be addressed, in which the aim is to find the effect of the potential $V(\mathbf{r})$ on the (single particle) wavefunction $\psi(\mathbf{r})$. The method used in the following derivation of the HEED starting equations is based upon that of Bird (1981).

2.2.1 The Fujiwara equation

An electron with a kinetic energy of 200keV travels at about 70% the speed of light c, so its motion should be described using a relativistic wave equation. If it is assumed that a scattering potential can be inserted into the free-particle Dirac equation in much the same way as in the low-energy Schrödinger equation, then (eg Schiff 1968)

$$\left(-i\hbar c\boldsymbol{\alpha}.\nabla_{\mathbf{r}} + \beta m_0 c^2 + V\right)\psi \;=\; E\psi \tag{2.2.1}$$

where the potential $V \equiv 0$ outside the crystal, $\hbar$ and m_0 have their usual meaning, and $\nabla_{\mathbf{r}}$ is the 3-dimensional gradient operator. Note that the total energy E of the incident electron is the sum of its rest mass energy and the kinetic energy given to it by acceleration in the electron microscope. If it is required that for a free particle [$V = 0$] (2.2.1) leads to the classical dispersion relation

$$E^2 \;=\; p^2c^2 + m_0^2c^4, \tag{2.2.2}$$

then for a spin half particle the smallest representation of $\boldsymbol{\alpha}$ and β is as 4 by 4 matrices, which must have a square of unity, and must anticommute in pairs (Schiff 1968). These matrices are most commonly expressed in the block form

$$\beta = \begin{pmatrix} 1 & 0 \\ 0 & -1 \end{pmatrix}; \quad \boldsymbol{\alpha} = \begin{pmatrix} 0 & \boldsymbol{\sigma} \\ \boldsymbol{\sigma} & 0 \end{pmatrix}, \tag{2.2.3}$$

where the $\boldsymbol{\sigma}$ are the 2 by 2 Pauli spin matrices. We see here that spin is automatically included in a genuinely relativistic wave equation. Since these terms in the Hamiltonian are not scalar, ψ itself is not a scalar, but a 4-component spinor. It is convenient for our purposes to decompose ψ into its "positive energy" and "negative energy" parts ψ_a and ψ_b. [These 2-component spinors get their name from the two free-particle solutions to (2.2.1), which each have a spin up and a spin down component, but opposite energy.] This may be done by multiplying out (2.2.1) with the matrices (2.2.3) entered in block form to yield

$$\psi_a = \frac{-i\hbar c}{E - V - m_0 c^2}(\boldsymbol{\sigma}.\nabla_{\mathbf{r}})\psi_b \tag{2.2.4}$$

and

$$\psi_b = \frac{-i\hbar c}{E - V + m_0 c^2}(\boldsymbol{\sigma}.\nabla_{\mathbf{r}})\psi_a. \tag{2.2.5}$$

Substitution of either one of these in the other leads to separate equations for ψ_a and ψ_b which are an exact transformation of the Dirac equation (2.2.1). For the positive energy solution ψ_a, this gives

$$\left(\nabla_{\mathbf{r}}^2 + k^2 - \frac{2m_0\gamma V}{\hbar^2}\right)\psi_a = -\frac{(\boldsymbol{\sigma}.\nabla_{\mathbf{r}}V)(\boldsymbol{\sigma}.\nabla_{\mathbf{r}})}{E - V + m_0 c^2}\psi_a - \frac{V^2}{\hbar^2 c^2}\psi_a, \tag{2.2.6}$$

with a similar expression for ψ_b, apart from the small but crucial difference that the denominator in the first term on the right hand side is $E - V - m_0 c^2$. In this equation, γ is the Lorentz factor $E/m_0 c^2$, and the relativistic wavenumber k (defined as $2\pi/\lambda$) is given by

$$k^2 = \frac{E^2 - m_0^2 c^4}{\hbar^2 c^2} = \left(\frac{m_0 c}{\hbar}\right)^2 (\gamma^2 - 1). \tag{2.2.7}$$

Note that in the first step, $k = p/\hbar$, consistent with the description of the wavefunction outside the crystal as the plane wave $\exp(i\mathbf{k}.\mathbf{r})$. It is now useful

to define a new, parameterised potential

$$U(\mathbf{r}) = \frac{2m_0\gamma}{\hbar^2}V(\mathbf{r}). \tag{2.2.8}$$

We have then arrived at the Fujiwara equation (1961,1962), the traditional starting point for HEED theory,

$$\left(\nabla_{\mathbf{r}}^2 + k^2 - U(\mathbf{r})\right)\psi(\mathbf{r}) = 0, \tag{2.2.9}$$

provided it can be demonstrated that

(a) the right hand side of (2.2.6) can be neglected, and

(b) the negative energy spinor ψ_b plays no significant rôle.

Note that if these provisos are satisfied, the wavefunction ψ will revert to being scalar, since all reference to spin will be lost. Note also that the Fujiwara equation (2.2.9) is of the form of a Schrödinger equation, with U and k^2 acting as the potential energy and total energy respectively. Since k is a wavenumber, it has become reasonably common practice to express HEED energies in units of Å^{-2}. These will be the standard units used in this thesis. It may also be noted in passing that the effective potential in (2.2.8) varies in strength with the incident electron energy, via the relativistic factor γ.

2.2.2 The small-angle scattering approximation

The Fujiwara equation (2.2.9) may be derived from equation (2.2.6) by invoking just one more approximation. Figure 2.2.1 shows a simple schematic of the geometry and nomenclature that will be considered in the analysis of THEED and RHEED. In both cases, the incident cone of electrons is directed along or close to a crystallographic, or zone axis. It will be assumed throughout this

thesis that the crystal surfaces are perfectly flat and infinitely long, and that we may work in the simplest possible specimen geometry, as shown in figure 2.2.1. In transmission, this geometry (referred to as the "symmetric Laue" geometry) assumes the surface normal of the crystal and the zone axis direction to be parallel. [It is perhaps more common to have the surface normal and the zone axis pointing in opposite directions.] The zone axis direction will be denoted by the coordinate z. The remaining two spatial coordinates will be denoted by the vector $\mathbf{R}$, which is perpendicular to z.

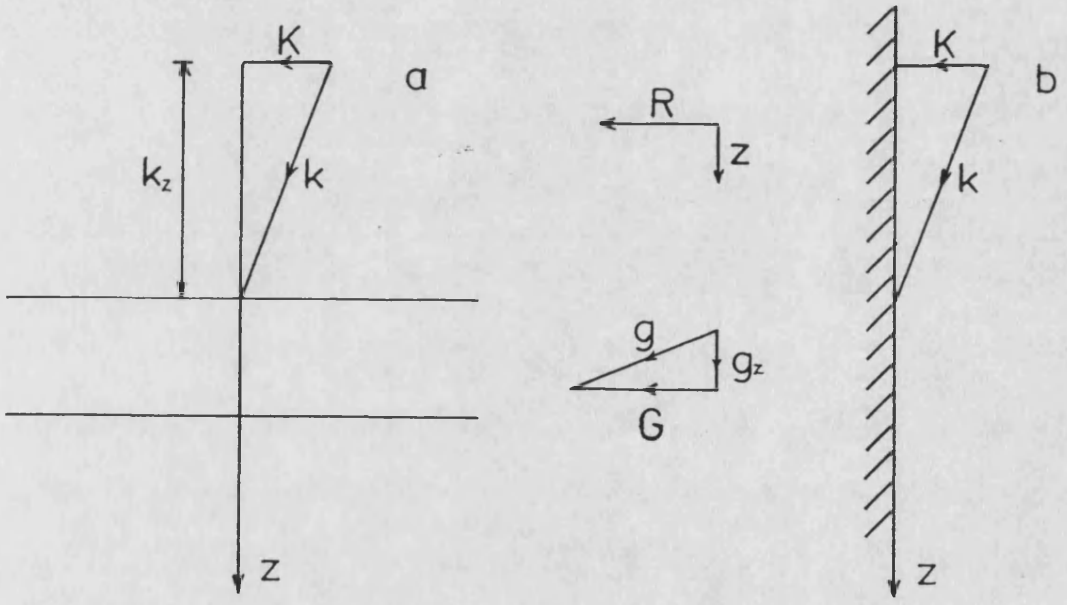

Figure 2.2.1. Schematic of the THEED (a) and RHEED (b) geometries considered in this thesis. Note that z is always taken as the zone axis direction. Upper case letters indicate 2-dimensional vectors perpendicular to this z-direction.

All the 3 dimensional vectors may then be decomposed into components parallel and perpendicular to z. For example, $\mathbf{k} \rightarrow (\mathbf{K},k_z)$, so that the incident orienta-

tion of an electron will basically be given by the coordinate **K** (see figure 2.2.1). Note that we have chosen to keep z as the zone axis in RHEED. It is more usual to keep the surface normal as the consistent direction in the two geometries, but since the common feature of interest here is that all the scattering is through small angles, the nomenclature introduced here is more appropriate. Note finally that by restricting attention to the symmetric Laue geometry in transmission, the boundary conditions needed for the solution of the diffraction equations will be in their simplest possible form.

Now, the range of incidence angles about the z-axis is typically $\sim 1°$, so clearly $k \gg K$. It is also known that the magnitude of the scattering potential U is small compared with the total "energy" k^2, and gets smaller at large angles due to the fall-off of the atomic form factors. As a guide, the largest Fourier component of the potential for a strong scatterer such as gold is $U_0 \sim 10\text{Å}^{-2}$ for 200kV electrons, whereas at this energy $k^2 \sim 6 \times 10^4 \text{Å}^{-2}$. Thus it might be expected (and experiment confirms) that the whole of a HEED pattern is confined to diffraction through small angles. This is a statement of the small-angle scattering approximation (SASA). Mathematically, it may be expressed (for example) as

$$U \ll k^2; \quad |\mathbf{K} + \mathbf{G}| \ll k, \tag{2.2.10}$$

where **G** is the component of the reciprocal lattice vector **g** in the plane of **K**.

It should be noted that the SASA is usually made with reference to transmission microscopy. In this case a result of considering only small angle scattering is that backscattering from the top face of the crystal slab may be neglected. Thus

the "forward scattering approximation" (eg Bird 1989) is made, which is entirely equivalent to the SASA in transmission, but which is so called because of the neglect of electrons reflected back from the entrance surface of the crystal. In order to be consistent for both THEED and RHEED, though, it should be made clear that in both cases we ignore scattering events that in our nomenclature produce a negative k_z, which is why the approximation has been given the name here that it has.

One of the consequences of the SASA is that the longitudinal (ie z) and transverse (ie $\mathbf{R}$) motions will be very different in character. It is therefore convenient to factor out a rapidly varying part $\exp(ikz)$, by writing the wavefunction as

$$\psi(\mathbf{R}, z) \;=\; \exp(ikz)\varphi(\mathbf{R}, z) \tag{2.2.11}$$

where the new wavefunction φ is expected to be slowly varying in z and $\mathbf{R}$. This representation will presently be used in applying the SASA to (2.2.6), and will later help simplify the Fujiwara equation (2.2.9) yet further.

The Fujiwara equation may now be derived, using the representation (2.2.11). Since in (2.2.6) the potential $U = 2m_0\gamma V/\hbar^2$ is by far the smallest term on the left hand side, it need only be shown that the terms on the right hand side are small compared to U, in order that (2.2.6) be a useful starting equation.

The second term is easily compared to the potential. We obtain

$$\frac{V^2/\hbar^2c^2}{2m_0\gamma V/\hbar^2} \;=\; \frac{V}{2E} \tag{2.2.12}$$

which is small by assumption in the SASA. The first term is rather more tricky. To analyse it, we take $|\boldsymbol{\sigma}| \sim 1$ and $E = \gamma m_0c^2 \gg V$ to give

$$\frac{(\boldsymbol{\sigma}.\nabla_{\mathbf{r}}V)(\boldsymbol{\sigma}.\nabla_{\mathbf{r}})\psi_a}{U(E - V + m_0c^2)} \approx \frac{|\nabla_{\mathbf{r}}V\nabla_{\mathbf{r}}\psi_a|\hbar^2}{2m_0\gamma V(1+\gamma)m_0c^2} = \frac{|\nabla_{\mathbf{r}}V\nabla_{\mathbf{r}}\psi_a|}{k^2}\frac{(\gamma^2-1)}{2\gamma(1+\gamma)} \tag{2.2.13}$$

where the definition of U (2.2.8) and k (2.2.7) have been used.

With V expressed as the Fourier series (2.1.2), it is clear that $|\nabla_{\mathbf{r}} V| \leq g_{max}|V|$, where g_{max} is the length of the largest scattering vector under consideration. Since all scattering is through small angles the size of $g_{\mathbf{max}}$ is governed by the change in the transverse component of the wavevector; it therefore follows that $|\nabla_{\mathbf{r}} V| \sim KV$. Also, from (2.2.11) it is assumed that the greatest spatial variation in ψ is in the z-direction and is contained within the extracted exponential term. We therefore write $\nabla_{\mathbf{r}}\psi \sim \partial\psi/\partial z \sim k\psi$, so that (2.2.13) becomes

$$\frac{(\boldsymbol{\sigma}.\nabla_{\mathbf{r}} V)(\boldsymbol{\sigma}.\nabla_{\mathbf{r}})\psi_a}{U(E - V + m_0c^2)} \sim \frac{K}{k}, \tag{2.2.14}$$

where the terms involving γ are of order unity, and have been omitted. Thus the first term in (2.2.6) may be neglected within the SASA. As an aside, a cone angle of 1° implies $k \sim 100K$, so spin effects should be detectable in HEED experiments at a level of 1% of the "spinless" potential U. It would be an interesting exercise to treat spin as a perturbation on U, using methods similar to those of the later chapters of this thesis, to try and predict some way in which spin effects might be seen in an electron microscope.

Proviso (a) has now been satisfied, but what of (b)? Using the same approximations as above, it is seen that (2.2.5) gives

$$\psi_b \approx \frac{-i\hbar c}{m_0c^2(1+\gamma)}.\frac{m_0c}{\hbar}\sqrt{\gamma^2-1}\psi_a = -i\frac{\sqrt{\gamma^2-1}}{1+\gamma}\psi_a. \tag{2.2.15}$$

At 200keV, this yields $\psi_b \sim 0.4\psi_a$. Thus the spinor ψ_b is not negligible in terms of its size, but since (to the accuracy of our approximation) it is proportional to ψ_a, it contains no new information. As a consequence, the major effects of both

ψ_a and ψ_b can incorporated into a single scalar wavefunction ψ which will satisfy (2.2.9), and which must be properly normalised to allow for the amalgamation of ψ_a and ψ_b. In practice this may be done by choosing the amplitude of an incident plane wave as unity.

To summarise, then, the Fujiwara equation (2.2.9) has now been derived by neglecting terms (specifically those involving spin) which are of the order of 1% of the potential U. It is customary at this point (eg Bird 1989) to introduce the "forward scattering approximation", by writing the wavefunction as in (2.2.11). In truth, however, this approximation has already been used in getting this far. It is therefore only a natural extension to substitute (2.2.11) into (2.2.9) to give

$$\left[-\nabla_{\mathbf{R}}^2 + U(\mathbf{R},z)\right]\varphi(\mathbf{R},z) \;=\; 2ik\frac{\partial\varphi}{\partial z} + \frac{\partial^2\varphi}{\partial z^2}. \qquad (2.2.16)$$

Now, for a plane wave solution with $k \gg K$, $\frac{\partial\varphi}{\partial z} \sim \frac{K^2}{k}\varphi$. The second of the terms on the right-hand side of (2.2.16) is therefore $\sim (\frac{K}{k})^2$ smaller than the first, and is ignored, leaving

$$\left[-\nabla_{\mathbf{R}}^2 + U(\mathbf{R},z)\right]\varphi(\mathbf{R},z) \;=\; 2ik\frac{\partial\varphi}{\partial z}. \qquad (2.2.17)$$

The major consequence of ignoring the φ'' term is that the free-space solution becomes

$$\varphi(\mathbf{R},z) \;=\; \exp(i\mathbf{K}.\mathbf{R})\exp\left(\frac{-iK^2z}{2k}\right), \qquad (2.2.18)$$

so that the free electron sphere $k_z = \sqrt{k^2 - K^2}$ is replaced by a parabola $k_z = k - K^2/2k$, and backwards travelling waves ($k_z < 0$) are not permitted. For these reasons, the approximation is known both as the parabolic and the forward scattering approximation.

Equation (2.2.17) is the most useful for the analysis of HEED, as will be shown later. It is identical in form to the time-dependent low-energy Schrödinger equation

$$\left[-\frac{\hbar^2}{2m_0}\nabla_{\mathbf{r}}^2 + V(\mathbf{r},t)\right]\varphi(\mathbf{r},t) = i\hbar\frac{\partial\varphi}{\partial t} \qquad (2.2.19)$$

except that the time variable t is replaced by the depth z of an electron in the specimen, and the remaining 2 space dimensions $\mathbf{R}$ play the rôle of $\mathbf{r}$. We are therefore able to make use of the techniques of low-energy quantum mechanics in subsequent analysis of HEED, starting from (2.2.17). This is, of course, the reason why high-energy electrons appear to exhibit low-energy single-particle quantum mechanics in the microscope, with the interesting quirk that the equivalent of Planck's constant is a variable!

2.2.3 The projection approximation

The final approximation which will be of general use is the projection approximation. To see how it arises, let us first introduce a useful geometric construction for visualising diffraction geometry. As a note of caution, it should be realised that what follows is a kinematic or "zero-potential" argument. However, the general principles still apply in dynamical situations, so the construction is used to keep the explanation simple. At 200keV, the wavenumber of an incident electron is $k = 250\text{Å}^{-1}$, which is much larger than a typical spacing between reciprocal lattice points, $g \sim 1\text{Å}^{-1}$. As stated in Chapter 1, Bragg diffraction changes the electron wavevector $\mathbf{k}$ to $\mathbf{k}' = \mathbf{k} + \mathbf{g}$, and conserves energy, and hence the value of $|\mathbf{k}| = k$. Thus the locus of all possible final wavevectors $\mathbf{k}'$ is a sphere of radius k, which passes through the reciprocal lattice origin and which is centred

at a position $-\mathbf{k}$ from the origin. Appreciable diffraction will occur into those $\mathbf{k}+\mathbf{g}$ which lie close to the surface of the sphere. This spherical construction is usually referred to as the Ewald or reflecting sphere (see for example Hirsch *et al.* 1965).

Now, most diffraction patterns are taken at a crystallographic or zone axis. Such an axis describes a direction in the crystal perpendicular to a set of reciprocal lattice layers, as shown in figure 2.2.2.

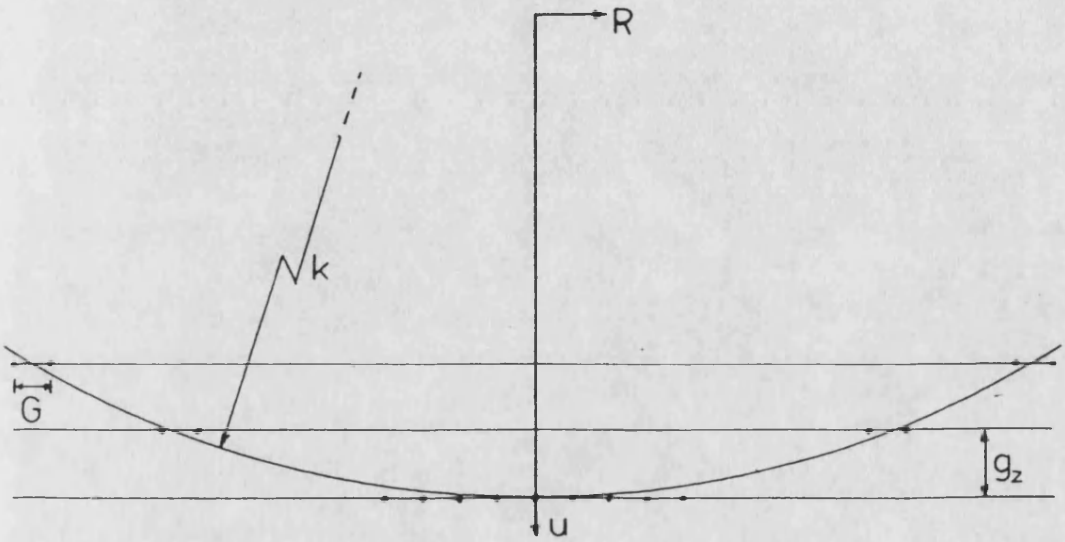

Figure 2.2.2 The separation of the reciprocal lattice into layers perpendicular to the zone axis. The strongest diffraction is observed in the central, zero-layer region.

The vectors $\mathbf{G}$ in the zeroth layer (containing the reciprocal lattice origin) satisfy $\mathbf{G}.\mathbf{u}=0$, where $\mathbf{u}$ is the direction vector of the zone axis. The upper layers are identical to the zeroth, (apart from a possible offset) and are uniformly spaced by g_z in the zone axis direction. The potential may therefore be written

$$U(\mathbf{r}) = \sum_{layers\ n} \exp(ing_z z) U^{(n)}(\mathbf{R}), \qquad (2.2.20)$$

where the "conditional projected potentials" are given by (eg Bird 1989)

$$U^{(n)}(\mathbf{R}) = \frac{1}{d}\int_0^d dz \ \exp(-ing_z z)U(\mathbf{r}). \qquad (2.2.21)$$

Here d is the spacing $2\pi/g_z$ between planes perpendicular to the zone axis. Since the Ewald sphere radius (k) is so much larger than typical reciprocal lattice basis vectors, many zero layer reflections will be excited at a zone axis. Thus the zeroth layer will usually extend out to a region of the diffraction pattern where the rapid fall-off of the potential U with scattering angle will have taken effect. For this reason, it may be assumed that most of the important diffraction occurs in the zeroth layer (the so-called zeroth order Laue zone, or ZOLZ). It is therefore customary to make the projection approximation, in which only the $n = 0$ term is included in (2.2.20), and the first and higher order Laue zones (FOLZ and HOLZ) are either ignored or treated as a perturbation to the ZOLZ diffraction (Buxton 1976). In the projection approximation, then, equation (2.2.17) becomes

$$\left[-\nabla_{\mathbf{R}}^2 + U^{(0)}(\mathbf{R})\right]\varphi(\mathbf{R}, z) = 2ik\frac{\partial\varphi}{\partial z}. \qquad (2.2.22)$$

This, finally, is our starting point for subsequent HEED analysis. In making the projection approximation, the "time" dependence of the potential U is lost (though of course it remains on the right hand side). For this reason (2.2.22) is now *separable* into $\mathbf{R}$ and z parts, which will be of considerable use in the following section. From now on we shall work entirely in the projection approximation, so that our basic scattering potential will be the true projected potential

$$U(\mathbf{R}) = U^{(0)}(\mathbf{R}) = \sum_{\mathbf{G}} U_{\mathbf{G}} \exp(i\mathbf{G}.\mathbf{R}), \qquad (2.2.23)$$

where

$$U_{\mathbf{G}} = \frac{1}{A_c} \int_{A_c} U(\mathbf{R}) \exp(-i\mathbf{G}.\mathbf{R}) d\mathbf{R}. \qquad (2.2.24)$$

Here A_c is the area of the 2-dimensional projected unit cell. The incident beam impinging upon a specimen in this projected geometry is just the plane wave $\varphi(\mathbf{R}, z)$, as given in (2.2.18).

2.3 REPRESENTATIONS OF THE HEED EQUATIONS

The diffraction equation (2.2.22) is not in a particularly useful form for the analysis which follows in Chapters 3 and 4. Since the incident and observed electrons are well described using plane waves, and the periodic potential U lends itself to a plane wave expansion, it is natural that the wavefunction inside the crystal should itself be expanded using a plane wave basis. Thus the representations that will be given below are based on reciprocal space arguments. Each is used widely in HEED (the first two in transmission, and the third in reflection), though it should not be assumed that such arguments are always the most suitable. Indeed, at strong zone axes, where very many plane waves would have to be included in an accurate expansion of the wavefunction, it may be that only two or three Bloch states are of importance, so a real-space approach would be more illuminating (eg Bird 1989). In the work presented here, however, areas in the outer regions of zone-axis diffraction patterns are chosen for analysis, where it will prove appropriate to treat all or part of the potential U perturbatively. Hence in the following work the reciprocal space methods are found to be the more useful.

2.3.1 The many-beam equations.

We begin with a commonly used THEED representation which is akin to the nearly free electron model of solid state theory (eg Ashcroft and Mermin 1976). Indeed, this model was invented and used for the analysis of HEED (Bethe 1928) before it was applied in its now familiar rôle. Although it will be shown that the many-beam equations are not useful as a means of expressing U as a perturbation term, they do lend themselves to a full numerical solution of the diffraction equations, in which all the dynamical interactions between the different diffracted beams are implicitly included. They are therefore useful for the purposes of comparison between our approximate results and a more exact theory. They are also in a convenient form to highlight the general processes of extracting diffracted amplitudes, treating absorptive potentials and so on.

Equation (2.2.22) is separable. Substituting $\varphi(\mathbf{R}, z) = \tau(\mathbf{R}).Z(z)$ into (2.2.22) gives (eg Howie 1966, Berry 1971)

$$\left[-\nabla^2_{\mathbf{R}} + U(\mathbf{R})\right] \tau^{(j)}(\mathbf{R}) \;=\; s^{(j)}\tau^{(j)}(\mathbf{R}) \tag{2.3.1}$$

and

$$2ik\frac{dZ^{(j)}}{dz} \;=\; s^{(j)}Z^{(j)} \;\Longrightarrow\; Z^{(j)} \propto \exp\left(\frac{-is^{(j)}z}{2k}\right). \tag{2.3.2}$$

In these equations s is the separation constant. From the form of (2.3.1), it is clear that s plays the rôle of an energy eigenvalue in a 2-dimensional eigenvalue equation. The variables s, τ and Z are therefore given the label (j) to indicate that such an eigen-equation will have more than one solution. To be more specific, (2.3.1) is exactly in the form of the time-independent Schrödinger equation in two dimensions. Since the potential $U(\mathbf{R})$ in this equation is periodic,

the solutions to (2.3.1) must be 2 dimensional Bloch waves, which we write as $\tau^{(j)}(\mathbf{K}', \mathbf{R})$. Here $\mathbf{K}'$ is a 2-dimensional Bloch wavevector, and (j) labels the different bands, or branches as they are termed in HEED. The 2-dimensional band-structure $s^{(j)}(\mathbf{K}')$ forms the "dispersion surface" in HEED parlance, and is often referred to as the transverse energy (Buxton 1976). As in 3-dimensional band theory, the periodicity of U means that we may work either in a reduced or extended zone scheme, as we wish. This point will be returned to in Chapter 4. Note that there will be frequent references in that chapter to "bound states". What is actually meant is that a 2-dimensional state τ is localised by the 2-dimensional potential, though in 3 dimensions the overall state is not bound within the crystal.

There are of course many ways in which (2.3.1) can be solved (Ashcroft and Mermin 1976). In the many-beam representation, the Bloch states are expanded as a sum of plane waves

$$\tau^{(j)}(\mathbf{K}', \mathbf{R}) = \sum_{\mathbf{G}} C_{\mathbf{G}}^{(j)}(\mathbf{K}') \exp\{i(\mathbf{K}' + \mathbf{G}).\mathbf{R}\}, \qquad (2.3.3)$$

where the $\mathbf{G}$ are the ZOLZ vectors, and the $C_{\mathbf{G}}^{(j)}$, which give the amount of each plane wave in the state (j), are usually referred to as Bloch wave coefficients. Substitution of (2.3.3) into (2.3.1) gives

$$\sum_{\mathbf{G}} \left[(\mathbf{K}' + \mathbf{G})^2 - s^{(j)}(\mathbf{K}') + U(\mathbf{R})\right] C_{\mathbf{G}}^{(j)}(\mathbf{K}') \exp\{i(\mathbf{K}' + \mathbf{G}).\mathbf{R}\} = 0. \quad (2.3.4)$$

We now apply a sifting technique familiar in all Fourier analysis (eg Riley 1974). Both sides of the equation are multiplied through to the left by the orthogonal plane wave $\exp\{-i(\mathbf{K}' + \mathbf{G}').\mathbf{R}\}$ and integrated over one period (in this case

the projected unit cell area A_c). This gives

$$\sum_{\mathbf{G}} \left\{ \left[(\mathbf{K}' + \mathbf{G})^2 - s^{(j)} \right] \delta_{\mathbf{G},\mathbf{G}'} + \frac{1}{A_c} \int d\mathbf{R} \exp\left\{ i(\mathbf{G} - \mathbf{G}').\mathbf{R} \right\} U(\mathbf{R}) \right\} C_{\mathbf{G}}^{(j)} = 0. \tag{2.3.5}$$

From (2.2.24) it is seen that the integral in (2.3.5) is just the Fourier component (or structure factor) $U_{\mathbf{G}'-\mathbf{G}}$. We choose to ignore the refractive component U_0 in this transmission representation since it has only a uniform (on-diagonal) effect on all the solutions. Consequently, each eigenvalue $s^{(j)}$ will describe an energy relative to U_0 rather than to the vacuum. Putting $U_{\mathbf{G}'-\mathbf{G}}$ into (2.3.5) yields the many-beam equations (eg Humphreys 1979)

$$\sum_{\mathbf{G}} \left\{ \left[(\mathbf{K}' + \mathbf{G})^2 - s^{(j)}(\mathbf{K}') \right] \delta_{\mathbf{G},\mathbf{G}'} + U_{\mathbf{G}'-\mathbf{G}} \right\} C_{\mathbf{G}}^{(j)}(\mathbf{K}') = 0. \tag{2.3.6}$$

This is a standard matrix equation which may be solved for the $s^{(j)}$ and $C_{\mathbf{G}}^{(j)}$ by diagonalisation at any orientation vector $\mathbf{K}'$. The size (n) of the many-beam matrix is determined by the number of independent beams, n, considered. In principle, $n \to \infty$ for a perfect representation, but good convergence of the solutions may be achieved in most situations by including a computationally manageable number of beams (typically $\sim$ 100 at a strong zone axis.) The simplest diffraction, involving the incident beam and only one diffracted beam (ie $n = 2$) is exactly soluble (see §2.4). For $n > 3$, there is no general analytic solution, and the diagonalisation must be performed numerically.

The desired amplitudes $A_{\mathbf{G}}$ are found from the $s^{(j)}$ and $C_{\mathbf{G}}^{(j)}$ by matching the wavefunction at the crystal surfaces. As stated before, these surfaces are at $z = 0$ and $z = t$ in the symmetric Laue transmission geometry. From the

earlier separation of variables, the wavefunction φ in the crystal can be written

$$\varphi = \sum_{\mathbf{K}'} \sum_{j} \varepsilon^{(j)}(\mathbf{K}') \tau^{(j)}(\mathbf{K}', \mathbf{R}) \exp\left(\frac{-is^{(j)}z}{2k}\right) \qquad (2.3.7)$$

where the $\varepsilon^{(j)}$ are just a set of expansion coefficients giving the excitation amplitudes of the different Bloch waves.

As the governing equation (2.2.22) is first order in z, only wavefunction amplitudes need be matched. At $z = 0$, φ is just the incident plane wave, which for convenience is assumed to have unit amplitude. Only waves with $\mathbf{K} = \mathbf{K}'$ can be excited (Snell's Law), so, using the plane wave expansion of the Bloch waves (2.3.3),

$$\varphi(z = 0) = \exp(i\mathbf{K}.\mathbf{R}) = \sum_{j,\mathbf{G}} \varepsilon^{(j)}(\mathbf{K}) C_{\mathbf{G}}^{(j)}(\mathbf{K}) \exp\{i(\mathbf{K} + \mathbf{G}).\mathbf{R}\}. \qquad (2.3.8)$$

The sifting procedure is this time performed with an orthogonal Bloch wave, to sift out an expression for the $\varepsilon^{(j)}$. Using the orthogonality of the coefficients $C^{(j)}$, this yields the particularly simple result $\varepsilon^{(j)}(\mathbf{K}) = C_{\mathbf{0}}^{(j)*}(\mathbf{K})$, where the asterisk denotes complex conjugation. It should be noted here that since the Bloch wavevector $\mathbf{K}$ is determined by the orientation of the incident electrons, and no restriction is imposed as to which values this orientation may take, the excitation amplitudes $C_{\mathbf{0}}^{(j)*}(\mathbf{K})$ are automatically expressed in an extended zone representation. However, the $C_{\mathbf{G}}^{(j)}$ into which the incident electrons couple are periodic and can be expressed in either a reduced or an extended scheme, though to ensure consistency with the Bloch wavevector $\mathbf{K}$ the latter is more commonly used.

At the exit face $z = t$, only plane waves are produced, with amplitudes $A_{\mathbf{G}}(\mathbf{K}, t)$.

Thus the wavefunction $\varphi(z=t)$ is given by

$$\sum_{j,\mathbf{G}} C_{\mathbf{0}}^{(j)*} C_{\mathbf{G}}^{(j)} \exp\{i(\mathbf{K}+\mathbf{G}).\mathbf{R}\} \exp\left(\frac{-is^{(j)}t}{2k}\right) = \sum_{\mathbf{G}} A_{\mathbf{G}} \exp\{i(\mathbf{K}+\mathbf{G}).\mathbf{R}\}. \tag{2.3.9}$$

Again we sift, this time to find the diffracted amplitudes $A_{\mathbf{G}}$. This gives

$$A_{\mathbf{G}}(\mathbf{K},t) = \sum_{j} C_{\mathbf{0}}^{(j)*}(\mathbf{K}) C_{\mathbf{G}}^{(j)}(\mathbf{K}) \exp\left(\frac{-is^{(j)}t}{2k}\right). \tag{2.3.10}$$

From these amplitudes the diffracted intensities may be calculated as $I_{\mathbf{G}} = |A_{\mathbf{G}}|^2$ at any incident orientation $\mathbf{K}$. Note that since the C form a complete, orthonormal set (Humphreys 1979), the total diffracted intensity $I = \sum_{\mathbf{G}} |A_{\mathbf{G}}|^2$ can be shown from (2.3.10) to be unity. This confirms that for a real scattering potential, the diffraction equation (2.2.22) is flux conserving. Programs already exist which will diagonalise the many-beam equations, and calculate diffracted amplitudes and intensities. In our work the many-beam analysis is performed using programs based on those of Baker (1982).

It has been assumed thus far that $U(\mathbf{R})$ is real. If this is not the case, the above analysis must be performed with rather more care. Let us write the many-beam matrix as H, such that $HC^{(j)} = s^{(j)}C^{(j)}$. If $U(\mathbf{R})$ is real, then H is hermitian, since in this case $U_{\mathbf{G}} = U^*_{-\mathbf{G}}$ - see (2.1.2). Since hermitian matrices are self-adjoint, it makes no difference whether we multiply to the left or the right in manipulating the quantum mechanical equations. However, if $U(\mathbf{R})$ is complex, the structure factors for $\mathbf{G}$ and $-\mathbf{G}$ are no longer conjugate to one another, so H becomes non-hermitian. The left-hand and right-hand eigenvectors of a non-hermitian matrix are not in general the same (eg Wilkinson 1965). Denoting the left-hand set of Bloch wave coefficients by $\widehat{C}^{(j)}$, it is found

that $\widehat{C}^{(j)}H = s^{(j)*}\widehat{C}^{(j)}$. In practice the $\widehat{C}^{(j)}$ may be found by diagonalisation of the adjoint matrix $H^\dagger$ to the right. The outcome of all this is that $\widehat{C}$ rather than C should be used each time our equations are multiplied to the left by a Bloch wave.

The other important feature of a non-hermitian Hamiltonian is that the eigenvalues are no longer real. The imaginary potential $U'(\mathbf{R})$ will produce imaginary components of the eigenvalues; if measured from the vacuum energy, these imaginary eigenvalues will give rise to exponentially decaying (ie *absorbed*) amplitudes. Relative to the mean absorptive potential U'_0, some of the imaginary parts of the eigenvalues will be negative and some positive. This is the redistributive anomalous absorption referred to in §2.1. In the non-hermitian case, then, the diffracted amplitudes become

$$A_{\mathbf{G}} = \sum_j \widehat{C}_{\mathbf{0}}^{(j)*}(\mathbf{K}) C_{\mathbf{G}}^{(j)}(\mathbf{K}) \exp\left(\frac{-is_R^{(j)}t}{2k}\right) \exp\left(\frac{-s_I^{(j)}t}{2k}\right), \qquad (2.3.11)$$

where $s_R^{(j)}$ and $s_I^{(j)}$ are the real and imaginary part of the jth eigenvalue of the matrix H. In this case the presence of non-zero imaginary eigenvalues $s^{(j)}$ means that the sum $\sum_{\mathbf{G}} |A_{\mathbf{G}}|^2$ does not give unity. As expected, a complex scattering potential leads to solutions of the diffraction equations which do not conserve flux.

Since the Bloch waves have been written as a sum of plane waves (2.3.3), the many-beam equations are a normal mode expansion of the diffraction equations, in which the only dependence of the wavefunction on the depth z in the crystal is found in the oscillatory component $Z(z)$. Consequently, the expansion coefficients C and $\widehat{C}$ do not vary with z, so an expression for the diffracted amplitudes

cannot be built up from a single scattering contribution, double scattering and so on, but must be calculated all at once by diagonalisation of the whole matrix. In other words, the many-beam representation does not lend itself to a Born expansion solution of the diffraction equations. This is because a Born expansion requires there to be some "chronology" to the scattering events; in transmission, for example, we trace out the path of an incident beam from $z = 0$, then follow two wavefunctions (scattered and unscattered) after an event at some intermediary depth $z = z'$, and so on, until the exit face $z = t$ is reached. In order that this approach be possible, it is necessary that the excitation amplitudes of the various waves or beams have a depth dependence. Likewise in RHEED, a suitable method for a series expansion must include excitation amplitudes which may be associated with *individual* states of the fast electron. Approximate total amplitudes may then be constructed by considering the the coupling between as many of these states as required. The next two sections introduce a representation for each of the two geometries which can be used in Born series expansions.

2.3.2 The Howie-Whelan equations

The first geometry treated is that of transmission. The expansion of the wavefunction φ will therefore include excitation amplitudes which are z-dependent. We shall of course work in projection, and for the present treat the scattering potential $U(\mathbf{R})$ as real, and perfectly periodic. The usual development of the diffraction equations in this case is in terms of the equations of Howie and Whelan (1961). In their formalism, under the conditions outlined above, the electron

wavefunction would be constructed as the sum

$$\varphi(\mathbf{R}, z) = \sum_{\mathbf{G}} a_{\mathbf{G}}(z) \exp\{i(\mathbf{K}+\mathbf{G}).\mathbf{R}\}. \qquad (2.3.12)$$

That is, the behaviour in the transverse ($\mathbf{R}$) directions is described using plane waves, with the potential U causing Bragg diffraction by the zero-layer reciprocal lattice vectors. All of the z-dependence is absorbed into the wave amplitudes $a_{\mathbf{G}}(z)$. This z-dependence essentially consists of two components; the amplitude of the $\mathbf{G}^{th}$ beam at height z, and a propagator giving the evolution of this beam as it passes through the remainder of the crystal.

In the particular application which follows in Chapter 3, it is appropriate to assume that the latter (propagation) dependence can simply be written down. To do this, note that the free-space solution (2.2.18) to the diffraction equation (2.2.22) has an oscillatory z-dependence $\exp(-iK^2z/2k)$. Since each diffracted beam propagates below the crystal in a similar way, the wavefunction is expanded as

$$\varphi = \sum_{\mathbf{G}} a_{\mathbf{G}}(z) \exp\{i(\mathbf{K}+\mathbf{G}).\mathbf{R}\} \exp\left(\frac{-i(\mathbf{K}+\mathbf{G})^2 z}{2k}\right), \qquad (2.3.13)$$

where the $a_{\mathbf{G}}$ are now just the amplitudes of each beam at height z. The desired amplitudes $A_{\mathbf{G}}$ at the bottom of the crystal are then clearly given by $a_{\mathbf{G}}(t)$. Note that the extraction of an oscillatory depth dependence is entirely equivalent to the common practice in time-dependent quantum mechanics of assuming an oscillatory time evolution $\exp(-i\omega t)$. Indeed, in this particular form, the representation we shall produce is exactly that used in time-dependent perturbation theory (eg Schiff 1968), for the case of a potential U perturbing the

free-space stationary eigenstates $\exp\{i(\mathbf{K}+\mathbf{G}).\mathbf{R}\}$. However, since the change in formalism from that of Howie and Whelan is only slight, it is still natural to refer to the final equations below as the Howie-Whelan equations.

To derive these equations, the wavefunction (2.3.13) is substituted into (2.2.22), and an orthogonal plane wave used to sift out the required variable, as in the last section. The result is

$$\frac{da_{\mathbf{G}}}{dz} = \frac{1}{2ik}\sum_{\mathbf{G}'} a_{\mathbf{G}'}U_{\mathbf{G}-\mathbf{G}'}\exp\left(\frac{i\left\{(\mathbf{K}+\mathbf{G})^2-(\mathbf{K}+\mathbf{G}')^2\right\}z}{2k}\right). \qquad (2.3.14)$$

These are the version of the Howie-Whelan equations which will be used in the analysis of three-beam diffraction (in which only three independent beams are involved) in Chapter 3. As will be seen there, one of the attractions of these equations is that when applied in a perturbation framework, they provide a particularly simple picture of dynamical diffraction, which is completely obscured in other approaches such as the many-beam representation. Note that the Howie-Whelan equations are first order in the amplitudes $a_{\mathbf{G}}$.

2.3.3 The Kambe equations

We now turn to the problem of finding a useful representation of the diffraction equations in the RHEED geometry. In doing so it will be necessary to highlight the crucial differences between RHEED and THEED. Most of these differences derive from the general relationship between spatial symmetry and momentum conservation (see for example Lax 1974). Referring to figure 2.2.1(a), it is clear that in transmission, assuming an infinitely long, perfectly periodic crystal, there is translational symmetry in the $\mathbf{R}$ direction. This implies that the momentum in this direction, $\mathbf{K}$, must be conserved to within a reciprocal lattice vector $\mathbf{G}$,

as mentioned before. In the z-direction, however, the translational symmetry is interrupted by the two crystal surfaces, so k_z is not conserved. In projection k_z is given by the difference between the total energy k^2 and the (variable) transverse energy $s^{(j)}$, via $k_z^2 = k^2 - s^{(j)}$. In the RHEED geometry [figure 2.2.1(b)], there are no interruptions in the z-direction, so there must be k_z conservation. Outside the crystal there is perfect symmetry under infinitesimal z displacements, implying absolute conservation of k_z. Inside the crystal, periodicity gives translational symmetry, and conservation of k_z to within a reciprocal lattice vector component g_z. Since the projection approximation is still being used, within the RHEED geometry of figure 2.2.1, all vectors with $g_z \neq 0$ are ignored, so we can say without ambiguity that k_z is completely conserved. Thus the z-dependence of the wavefunction $\varphi(\mathbf{R}, z)$ can be written down as the free-space solution $\exp(-iK^2 z/2k)$, and factored out to leave the z-independent function $\psi(\mathbf{R})$ satisfying

$$\left[-\nabla_{\mathbf{R}}^2 + U(\mathbf{R})\right] \psi(\mathbf{R}) \;=\; K^2 \psi(\mathbf{R}). \qquad (2.3.15)$$

This equation is of the form of the time-*in*dependent Schrödinger equation, as should be expected since the depth dependence has been removed from the problem. Thus RHEED in projection is very much a 2-dimensional version of LEED (Pendry 1974), apart from a few details to which we return in Chapter 4. Note that (2.3.15) is a true scattering equation, in which the eigenvalue (K^2) is *fixed*, and the aim is to find the effect of the scattering potential U on the wavefunction ψ.

There is just one more translational symmetry to consider. If the transverse vector $\mathbf{R}$ is broken down into a component x in the surface normal direction

and y in the surface parallel direction (see figure 4.1.3), then clearly K_y will be conserved to within a G_y. However, the presence of the surface in the x-direction leads once again to a relaxation of momentum conservation. Instead of the reciprocal lattice consisting of points with position vectors **G**, it now consists of rods perpendicular to the surface (see eg McRae 1979 and Chapter 4). The natural way to expand the wavefunction ψ is therefore to assume plane-wave behaviour in the y-direction, as in the Howie-Whelan equations, and to put all the x-dependence in expansion coefficients for the wavefunction on each rod G_y. We therefore write

$$\psi(x,y) = \sum_{G_y} \psi_{G_y}(x) \exp\{i(K_y + G_y)y\}. \tag{2.3.16}$$

Having chosen to split the wavefunction in this way, it is natural to do the same with the potentials, which are therefore written as

$$U(x,y) = \sum_{G_y} U_{G_y}(x) \exp(iG_y y). \tag{2.3.17}$$

The $U_{G_y}(x)$ will be referred to as rod potentials. Thus, unlike in the transmission cases above, U_0 is not a constant, but a function describing the shape of the potential in the surface-normal direction in the crystal, as seen on the zeroth rod. The states $\psi_{G_y}(x)$ are the eigenstates of the rod potentials, and need not therefore be plane waves.

If (2.3.16) is substituted into (2.3.15), and the same Fourier sifting is performed as before, this time over a y period, the resulting coupled equations are the Kambe equations (Kambe 1967):

$$\frac{d^2\psi_{G_y}}{dx^2} + K_x^2(G_y)\psi_{G_y} = \sum_{G'_y} U_{G_y - G'_y}(x)\psi_{G'_y}(x) \tag{2.3.18}$$

where

$$K_x^2(G_y) = K^2 - (K_y + G_y)^2 . \qquad (2.3.19)$$

These equations are second order in the amplitudes ψ_{G_y}, and as such describe a genuine scattering problem. The treatment of RHEED (especially by perturbation methods) is therefore suited to the use of Green's functions (eg Economou 1983). In the RHEED analysis of Chapter 4, the approximate wavefunction on a given rod will consist of contributions which started on that rod, and others which have been scattered into and out of other rods, via the inter-rod potentials $U_{G_y - G'_y}$. As will be shown there, the physical features of interest can be explained by the inclusion of just two rod potentials, so the resulting amplitude expressions within this formalism are not difficult to interpret.

2.4 THE BASIC GEOMETRY OF CBED PATTERNS

This final section of the chapter contains a brief explanation of how the basic features in a CBED pattern arise. The intention is to ease the explanation of the specific experimental geometries employed in later chapters. It should be emphasised, however, that the explanation which follows is not a conventional one for HEED, since it will be based upon the assumption that the diffraction is weak. A measure of the strength of diffraction at which such an assumption will fail is outlined later.

2.4.1 The Bragg condition and weak diffraction

Let us first consider purely geometrical effects. In the weak diffraction limit, the only regions of reciprocal space associated with elastic scattering will be those lying on a Bragg condition. The loci of all the positions describing a Bragg (or,

more exactly, a Laue) condition are the plane bisectors of the reciprocal lattice vectors $\mathbf{g}$ (eg Ashcroft and Mermin 1976). If an electron with wavevector $\mathbf{k}$ passes through this reciprocal lattice, its direction may be changed by Bragg scattering, but its wavenumber $k = |\mathbf{k}|$ may not. Thus for a given $\mathbf{k}$ and $\mathbf{g}$, the locus of all possible Bragg conditions is the circular intersection of the plane bisector of $\mathbf{g}$ and a sphere of radius k centred on the reciprocal space origin. This is shown schematically in figure 2.4.1 for two reciprocal lattice vectors $\pm\mathbf{g}$. Note that the spherical construction in this figure is *not* a conventional Ewald sphere, since its origin and that of the reciprocal lattice coincide.

The two circles inscribed on the sphere, corresponding to the Bragg conditions for diffraction by $+\mathbf{g}$ (A in figure 2.4.1) and $-\mathbf{g}$ (B) form a pair of "tramlines" in reciprocal space, separated by the distance AB$= |\mathbf{g}|$. The pair is symmetrical about a great circle of the sphere, in a plane perpendicular to $\mathbf{g}$ and passing through O. A similar set of tramlines will be inscribed on the sphere for all other pairs of reflections. Since the reciprocal lattice vectors $\mathbf{g}$ lie on a 3-dimensional lattice, these tramlines will inscribe the sphere in figure 2.4.1 at many well-defined angles and separations. Inevitably some sets of tramlines will intersect; the centres of regions at which this occurs are zone axes. Since in reality the sphere is so large, the tramline arcs around a zone axis are approximately straight lines. As will shortly be explained, these lines are seen as "Kikuchi" lines in experimental patterns, regardless of the incident electron illumination. A zone axis is associated with two or more intersecting pairs of Kikuchi lines.

Once a zone axis has been chosen (z in figure 2.4.1), these straight lines may be described as forming the ZOLZ, FOLZ and so on. Note that since k varies with

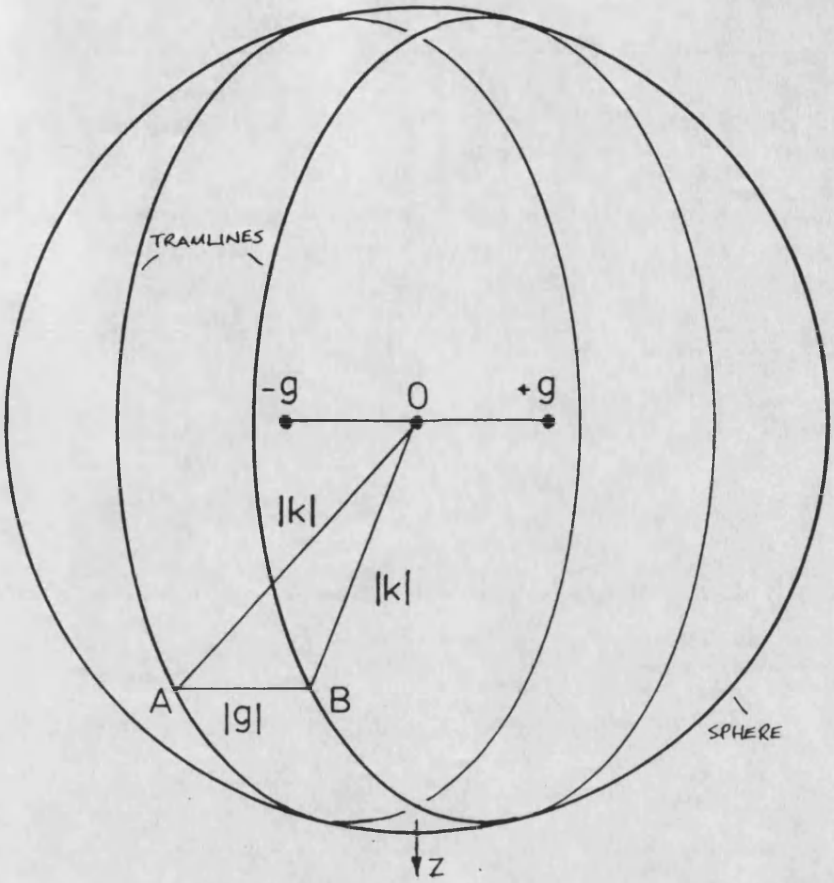

Figure 2.4.1 Diagram showing that the Bragg condition for the pair of reciprocal lattice vectors $\pm\mathbf{g}$ describes a pair of "tramlines" inscribed on a sphere of radius k. The spacing between the tramlines is AB$= |\mathbf{g}|$.

the incident electron energy, and the positions of the plane bisectors do not, the relative layout of the ZOLZ and HOLZ lines will change with energy. In projection, different positions in the 2-dimensional geometry may be described in terms of a 2-dimensional vector **K**.

Let us now introduce incident electrons into the system. In zone-axis diffraction, the scattering close to the axis is usually so strong that the kinematic tramlines described above are essentially irrelevant to the structure of the

pattern. However, if the diffraction is weak, as assumed, the elastically scattered electrons must lie on orientations along the tramlines. Figure 2.4.2 illustrates the most notable features observed when a convergent-beam probe is incident upon a pair of intersecting tramlines. [As an aside, it should be mentioned that in this weak-beam limit, there is no need to worry about whether the convergent-beam discs are overlapping; this will be returned to in Chapter 3.] The incident probe shown is symmetric with respect to the tramlines AA' and BB'. Thus the Bragg scattering between the two (inside the circular incident probe) is symmetrical and superimposed each on the other, to produce no net effect. By contrast, electrons between F and F' will produce a "deficit" line in the "bright-field" disc as electrons are diffracted by g onto the "excess line" EE' in the "dark field".

If only weak, elastic scattering were possible, then, only the bold deficit and excess lines in figure 2.4.2. would appear in a pattern. In fact, intensity variations do appear as "Kikuchi" lines along other portions of the tramlines which are not excited directly. Kikuchi lines are caused by the Bragg diffraction of inelastically scattered electrons; an inelastic scattering event will cause a whole range of secondary orientations to be weakly excited, some of which will then be at a Bragg condition. Thus the diffuse background caused by inelastic scattering will be highlighted by Kikuchi lines lying exactly on the tramlines. Since most of this diffuse scattering is in the forward direction, Kikuchi lines tend to be strongest close to the incident probe. Also, since the electrons responsible for Kikuchi lines may have come from many incident orientations, their effects are incoherent with direct Bragg diffraction. In regions such as EE' where both

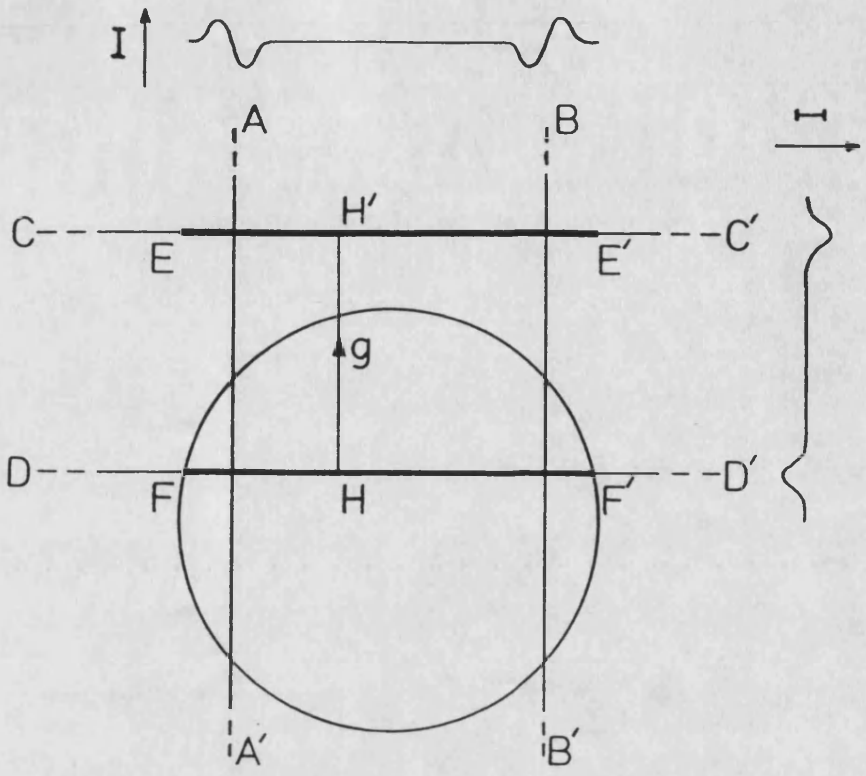

Figure 2.4.2. Schematic of some of the features which arise in a weak-beam CBED pattern. The circle represents the incident probe. See text for details.

Bragg and Kikuchi lines contribute, the two should be added in intensity.

It should be noted that the shape of the intensity profile across a Kikuchi line will depend on whether the underlying tramlines are excited symmetrically or asymmetrically by the incident electron probe (eg Reimer 1984). Typical profiles for the two cases are sketched in figure 2.4.2. The Kikuchi "band" AA', BB' is excited symmetrically, giving rise to a different intensity profile to that along the asymmetrically excited CC', DD' band. In practice, the sign of the intensity changes depends on the crystal thickness and the scattering angle. However, the cause of the profile is not important here (see eg Reimer 1984, Bird and Wright

1989).

2.4.2 Two-beam diffraction

This section is concluded with a brief outline of the features governing the strength of Bragg diffraction in a given pattern. Let us consider a portion of the incident probe close to the Bragg condition $\mathbf{K} = -\mathbf{g}/2$ (at H in figure 2.4.2) for diffraction by $\mathbf{g}$. If this orientation is situated in a part of the pattern well away from the Bragg condition of other reflections, an analysis of the diffraction locally need consider only the beams $\mathbf{0}$ and $\mathbf{g}$. The "two-beam theory" which results is well documented (eg Humphreys 1979) and need not be repeated here. The important point to note is that even with only two beams to consider, the situation is not as simple as the familiar kinematic diffraction theory (see Cowley 1981) in which only one diffraction process is allowed to occur, after which the beams become forever separated. In a proper analysis (as can be performed analytically by expansion of the many-beam equations (2.3.6) in this two-beam case), electrons can be scattered back and forth between the $\mathbf{0}$ and $\mathbf{g}$ beams. Thus multiple scattering produces a dynamical relationship between beams, leading to different distributions of intensity between the beams at different depths z. In two-beam theory the diffracted intensity for the $\mathbf{g}$ beam (neglecting absorption) may be shown to be

$$I_{\mathbf{g}} = \frac{U^2}{U^2 + W^2} \sin^2 \frac{\sqrt{U^2 + W^2}\, t}{2k}, \qquad (2.4.1)$$

with $I_{\mathbf{0}} = 1 - I_{\mathbf{g}}$ expressing flux conservation. In this equation, U is the modulus of the structure factor $U_{\mathbf{g}}$, t is the crystal thickness, and W, the "deviation parameter", is a measure of the deviation of the incident orientation from the

exact Bragg condition. Explicitly, in the two-beam case, $W = \mathbf{g}.\delta\mathbf{K}$, where $\delta\mathbf{K}$ is the actual deviation in terms of the incident electron orientation.

From (2.4.1) it is seen that the tramlines introduced earlier have a *width*, determined by the strength of the diffraction. A measure of this strength which will be used extensively in Chapter 3 is the dimensionless quantity

$$\beta = \frac{Ut}{2k}, \tag{2.4.2}$$

which is just the argument in (2.4.1) at the exact Bragg condition $W = 0$. If the width of each line becomes comparable with the tramline spacing $|\mathbf{g}|$, or if there are a sufficiently large number of excited reflections in the bright field that it is no longer clear that two-beam tramlines exist, then an approach based upon kinematic line constructions is no longer valid.

Due to the sinusoidal thickness dependence of the two-beam intensity (2.4.1), there will be depths z at which the diffracted intensity returns to zero. The first of these is termed the extinction distance, and plays the rôle of a mean free path in diffraction theory. It is usually denoted by ξ, and defined at the exact Bragg condition ($W = 0$); from (2.4.1) and (2.4.2) it is then clear that

$$\xi = \frac{2\pi k}{U} = \frac{\pi t}{\beta}. \tag{2.4.3}$$

For a "typical" crystal illuminated by 200keV electrons, ξ is of the order of a few 100Å for the shortest reciprocal lattice vectors. Since a "typical" transmission specimen is perhaps 1000Å thick, it is to be expected that zone-axis diffraction produces multiple scattering, and must therefore be described using a dynamical theory. Since the drive behind the work in this thesis is to build up a picture

of diffraction features starting from the simplest, kinematic arguments, it is clear that some care must be taken to ensure a perturbative analysis is worth pursuing.

2.5 SUMMARY OF THE IMPORTANT EQUATIONS

A few of the equations derived in this chapter will frequently be referred to in later ones. They are therefore listed here for easy reference. The basic equation to be solved throughout is the "high-energy Schrödinger equation" in projection

$$\left[-\nabla_{\mathbf{R}}^2 + U^{(0)}(\mathbf{R})\right] \varphi(\mathbf{R}, z) \;=\; 2ik\frac{\partial \varphi}{\partial z}. \tag{2.2.22}$$

In both transmission (Chapter 3) and reflection (Chapter 4), approximate solutions to (2.2.22) will be found. In the former, the approximations are developed through the Howie-Whelan equations

$$\frac{da_{\mathbf{G}}}{dz} \;=\; \frac{1}{2ik}\sum_{\mathbf{G}'} a_{\mathbf{G}'} U_{\mathbf{G}-\mathbf{G}'} \exp\left(\frac{i\left\{(\mathbf{K}+\mathbf{G})^2 - (\mathbf{K}+\mathbf{G}')^2\right\} z}{2k}\right), \tag{2.3.14}$$

and in the latter via the Kambe equations

$$\frac{d^2\psi_{G_y}}{dx^2} + K_x^2(G_y)\psi_{G_y} \;=\; \sum_{G_y'} U_{G_y - G_y'}(x)\psi_{G_y'}(x) \tag{2.3.18}$$

where

$$K_x^2(G_y) \;=\; K^2 - (K_y + G_y)^2 . \tag{2.3.19}$$

In both cases, the transmission many-beam equations will be used to provide a fully dynamical solution with which to compare our approximations. In the hermitian case they are given by

$$\sum_{\mathbf{G}} \left\{ \left[(\mathbf{K}' + \mathbf{G})^2 - s^{(j)}(\mathbf{K}')\right] \delta_{\mathbf{G},\mathbf{G}'} + U_{\mathbf{G}'-\mathbf{G}} \right\} C_{\mathbf{G}}^{(j)}(\mathbf{K}') \;=\; 0. \tag{2.3.6}$$

Chapter 3

A METHOD FOR THE MEASUREMENT OF CRYSTALLOGRAPHIC PHASE

3.1 INTRODUCTION

This chapter contains a perturbative solution to the THEED equation (2.2.22) starting from the Howie-Whelan representation (2.3.14). The solution will be constructed for the so-called three-beam geometry, in which only three independent Bragg beams play a significant rôle. As will be discussed in due course, three-beam diffraction offers the simplest opportunity for the solution of the phase problem of crystallography, familiar in X-ray analysis (see eg Ladd and Palmer 1977). The chapter therefore begins with an explanation of how this problem arises, and of the ways in which it may be "solved" by deducing the value of combinations of crystallographic phase, known collectively as phase invariants. §3.2 then introduces an experimental technique which provides many examples of the three-beam geometry, all associated with rather weak Bragg reflections. It is the Fourier components of the scattering potential, or structure factors, associated with these weak beams which are then treated as a perturbation in the Howie-Whelan equations. This enables the equations to be expanded as a Born series which, when truncated, yields a surprisingly simple prescription for the *measurement* of three-beam phase invariants. Most of the other attempts to extract these invariants from experiment, some of which will be mentioned later, are based upon dynamical analysis of at least part of the problem; these

methods are non-invertible, even for three beams. The method described here is therefore believed to be one of only two methods presently available which does not rely on *fitting* procedures for its success (see Shen and Collela 1988 for the other), and which is generally applicable to both centrosymmetric and noncentrosymmetric crystals. Since the description of the diffraction is approximate, §3.3 contains a study of the likely effect of ignoring higher-order terms in the Born expansion, and of the way in which absorption will affect the features of interest. The method is then tested experimentally for a noncentrosymmetric crystal of known, simple, structure. Much of the content of this chapter has been reported (somewhat briefly) in the papers by Bird, James and Preston (1987), James and Bird (1987) and Bird and James (1988).

3.1.1 The phase problem

For the moment, it will be convenient to exclude the possible effects of absorption, a non-symmetric Laue geometry and so on, and work with the simplest possible model, in which the incident electrons impinge on an infinite, parallel-sided, perfectly periodic crystal. The influence of some of the neglected features on the final results of the analysis will be given in §3.3, though it should be mentioned here that no change in the structure of what follows will be necessary for those discussions. The 3-dimensional scattering potential seen by the incident electrons will therefore be taken as [see (2.1.2) and (2.2.8)]

$$U(\mathbf{r}) = \frac{2m_0\gamma}{\hbar^2}V(\mathbf{r}) = \sum_{\mathbf{g}} U_{\mathbf{g}} \exp(i\mathbf{g}.\mathbf{r}). \qquad (3.1.1)$$

Here the $\mathbf{g}$ are reciprocal lattice vectors and the structure factors $U_{\mathbf{g}}$ are complex quantities constructed by the coherent addition of the form factor $u_\kappa(\mathbf{g})$ of each

atom κ at position $\mathbf{r}_\kappa$ in the unit cell:

$$U_{\mathbf{g}} = \sum_{\kappa} u_\kappa(\mathbf{g}) \exp(-i\mathbf{g}.\mathbf{r}_\kappa) \equiv |U_{\mathbf{g}}| \exp(i\phi_{\mathbf{g}}). \qquad (3.1.2)$$

These $u_\kappa(\mathbf{g})$ are scaled from the quantities $v_\kappa(\mathbf{g})$ of §2.1 as is $U(\mathbf{r})$ from the crystal potential $V(\mathbf{r})$, and may include a Debye-Waller factor. They are therefore real quantities (since absorption is ignored), so the phase $\phi_{\mathbf{g}}$ of each structure factor $U_{\mathbf{g}}$ arises entirely from the geometrical phase difference between different atoms in the unit cell, though of course each contribution is weighted by the appropriate atomic form factor. If, as is usually the case for X-rays, the extinction distance for Bragg scattering is much greater than the specimen thickness, only single scattering is likely, so the amplitude $A_{\mathbf{g}}$ scattered from the incident direction by $\mathbf{g}$ is just proportional to $U_{\mathbf{g}}$. Then the single scattering or kinematic intensity observed in experiment is

$$I_{\mathbf{g}} = |A_{\mathbf{g}}|^2 \propto |U_{\mathbf{g}}|^2. \qquad (3.1.3)$$

In solving a crystal structure the aim is to reconstruct the potential U to determine the nature (u_κ) and position ($\mathbf{r}_\kappa$) of each atom in the unit cell. Under single scattering conditions, though, (3.1.3) indicates that observed intensities yield only structure factor amplitudes $|U_{\mathbf{g}}|$ and all reference to the phase $\phi_{\mathbf{g}}$ is lost. This is the phase problem of crystallography; it is a problem because it hinders the reconstruction of $U(\mathbf{r})$, and arises because of the weak scattering of X-rays by a typical crystalline specimen. As an aside, it should be mentioned that the measurement of *any* structure factor phases would be useful. In the so-called direct methods of crystallography (see eg Woolfson 1971) the phase problem is tackled by permuting various phase relationships, each with a given

probability distribution, until the most probable combination is found. It is therefore likely that if some of the phases or phase relationships could be input into the direct method programs, some of the levels of permutation would be unnecessary, and a self-consistent set of phases would be found more quickly. Even very approximate phases (to within the correct quadrant) should be of some use in this respect.

3.1.2 Phase invariants and three-beam diffraction

It is clear from the expressions (3.1.1) and (3.1.2) for the elastic scattering potential $U(\mathbf{r})$ that a shift of the real space origin $\Delta\mathbf{r}$ will cause a change in the value of a single structure factor phase:

$$\phi_{\mathbf{g}} \longrightarrow \phi_{\mathbf{g}} - \mathrm{g}.\Delta\mathbf{r}. \tag{3.1.4}$$

It is therefore not surprising that all reference to $\phi_{\mathbf{g}}$ is lost in kinematic or two-beam diffraction, since *no* measurable quantity in a periodic system can depend on the choice of origin. Of course, if the probe size were smaller than the size of the unit cell, the specimen would not be periodic with respect to the incident beam, so phase differences across the unit cell should be detectable. Such probe sizes have now been achieved, and their use in phase determination is being investigated (eg Rodenburg 1989), but they are not available in conventional microscopes. Hence in the régime we shall consider, in which the probe covers many unit cells, absolute structure factor phase is a meaningless quantity. In order to glean any phase information at all from a diffraction pattern, combinations of phases must be considered which are origin independent. These combinations are referred to as "phase invariants".

This requirement that *combinations* of beams must be considered for phase information to be preserved is more-or-less equivalent to requiring there to be beating between two coherent waves in the formation of a hologram. In the case of interest here, it turns out that the necessary "beating" is achieved by picking a geometry in which electrons are diffracted into the same final orientation by more than one set of Bragg reflections. The simplest geometry which produces this situation is the three-beam geometry (Lipscomb 1949), sketched in figure 3.1.1. † The essence of the geometry is that there are two sets of intersecting tramlines, associated with the Bragg reflections **g** and **h**. As in the two-beam geometry of §2.4, electrons with an incident wavevector terminating on or close to the **g** (**h**) "deficiency" tramline will be diffracted by **g** (**h**), [and back again if $U_{\mathbf{g}\,(\mathbf{h})}$ is sufficiently strong].

However, at orientations of the incident wavevector on or close to A in figure 3.1.1, electrons may be diffracted both by **g** *and* **h**. Since reciprocal lattice vectors form a closed set, $(\mathbf{g}-\mathbf{h})$ is also a possible reflection, so some of the electrons diffracted by **h** from A to B will be further diffracted by $(\mathbf{g}-\mathbf{h})$ from B to C. The flux arriving at C will therefore have come in part from direct diffraction by **g**, and part from double diffraction by **g** and then $(\mathbf{g}-\mathbf{h})$. If the structure factors are sufficiently strong, there will also be contributions to the amplitude $A_{\mathbf{G}}$ from more complicated routes around the triangle ABC.

† In electron diffraction, a somewhat artificial distinction is made between elastic and absorptive potentials, so there are combinations of elastic and absorptive structure factor phases which are origin independent, in what appears to be a two-beam geometry (Taftø 1983, 1987; Bird and Wright 1989).

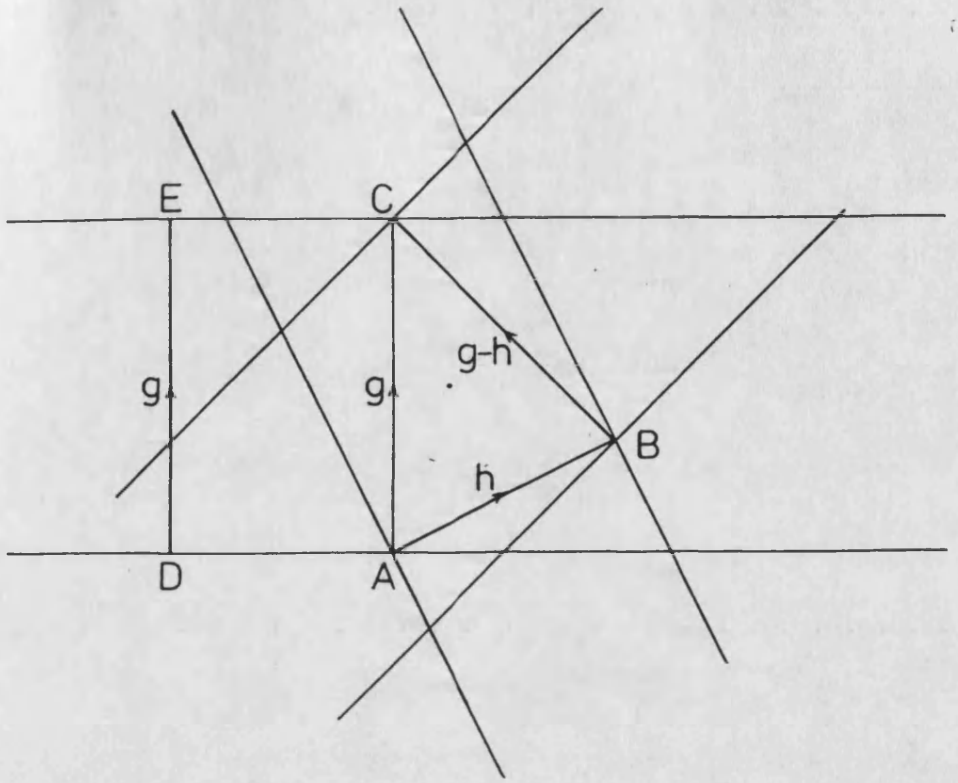

Figure 3.1.1. Portion of reciprocal space where three sets of tramlines intersect. An incident probe may be placed anywhere on this "Kikuchi" pattern (see §2.4). For example, if A is illuminated by incident electrons, both the **g** and **h** reflections are excited, and three-beam effects will be observed at B and C. If D is in the incident beam, only two beam interactions between D and E will occur.

Such routes will be neglected in the formation of our prescription, but will be considered again in §3.3. As all the incident electrons have come from or close to A, all this Bragg scattering is considered coherent, so the amplitudes arriving at C from the two different routes will add in amplitude, giving rise to beating between their phases. It will be seen later that if the combination of routes from A to C close the triangle ABC, then the intensity observed at C will contain phase information. This is a general result; whenever two sets of tramlines intersect, these three-beam interactions will occur.

To see the form which the three-beam phase invariant, or "phase triplet" will take, it is instructive to take an informal look at the weak scattering limit, in which diffracted amplitudes are proportional to structure factors. As has just been stated, the amplitude $a_{\mathbf{g}}$ diffracted by g in figure 3.1.1 will interfere at C with the two-step amplitude $a_{\mathbf{h}}a_{\mathbf{g}-\mathbf{h}}$. Hence the total amplitude scattered by g will be of the form

$$A_{\mathbf{g}} \propto U_{\mathbf{g}} + \alpha U_{\mathbf{h}} U_{\mathbf{g}-\mathbf{h}} + \cdots = U_{\mathbf{g}} \left(1 + \alpha \frac{U_{\mathbf{h}} U_{\mathbf{g}-\mathbf{h}}}{U_{\mathbf{g}}} \right) + \cdots \tag{3.1.5}$$

with α some algebraic factor. This expression represents the first two terms in a Born expansion of the amplitude (eg Cowley 1981) diffracted from A to C in figure 3.1.1. The observed intensity (at C) is given by the modulus squared of the amplitude:

$$I_{\mathbf{g}} \propto |U_{\mathbf{g}}|^2 \left\{ 1 + 2\Re \left[\alpha \frac{U_{\mathbf{h}} U_{\mathbf{g}-\mathbf{h}}}{U_{\mathbf{g}}} \right] + \cdots \right\}. \tag{3.1.6}$$

This crude analysis shows that the first correction term to the basic kinematic result (3.1.3) contains a combination of the three basic structure factors of interest. From the definition (3.1.2) of structure factor phase, it is seen that the overall phase of this first correction term is

$$\theta = \phi_{\mathbf{h}} + \phi_{\mathbf{g}-\mathbf{h}} - \phi_{\mathbf{g}}. \tag{3.1.7}$$

This combination of phases is *not* affected by a shift of the real-space origin, and is therefore a phase invariant, which will produce an anomaly of some sort in the observed intensity around the area C in figure 3.1.1. The aim of this chapter is to develop a technique which facilitates the measurement of phase

triplets θ directly from an electron micrograph. It is found that the method allows measurement of triplets to an accuracy of better than $\pm 15°$.

It should be mentioned immediately that the notion of determining phase triplets from a three-beam geometry is not new. The first attempt to do so (using X-rays) was by Lipscomb (1949). Since X-rays are scattered so weakly by crystals, the intensity anomaly caused by a phase triplet tends to be very small, so there have been considerable experimental difficulties encountered, even in the observation of these phase effects (eg Shen and Collela 1986). In addition, theoretical analysis (eg Juretschke 1982, 1984, 1986; Thorkildsen 1987) has been complicated by consideration of X-ray polarisation and the finite size of the specimen. The first of these makes the governing equation vectorial rather than scalar. The second complicates the boundary conditions as not all diffracted X-rays exit from the "bottom" of the sample.

Kambe (1957) pointed out that since electrons are scattered much more strongly by a crystal than are X-rays, three-beam intensity anomalies should be more readily detectable in THEED patterns. He showed that for a centrosymmetric crystal the determination of phase triplets is rather simple, and also suggested ways to recognise (if not measure) values of θ in noncentrosymmetric crystals. On the basis of this, several determinations have been made of centrosymmetric phase triplets using both X-rays and electrons (eg Hart and Lang 1961, Marthinsen and Høier 1986, Post and Ladell 1987).

In a centrosymmetric crystal, with the unit cell origin as the centre of symmetry, there is an atom of the same species at both $+\mathbf{r}_\kappa$ and $-\mathbf{r}_\kappa$. Thus, if there are

$2N$ atoms in the unit cell, the gth structure factor may be written [see (3.1.2)]

$$U_{\mathbf{g}} = \sum_{\kappa=1}^{N} u_{\kappa}(\mathrm{g}) \left[\exp(-i\mathbf{g}.\mathbf{r}_{\kappa}) + \exp(i\mathbf{g}.\mathbf{r}_{\kappa})\right] = \sum_{\kappa=1}^{N} 2u_{\kappa}(\mathrm{g}) \cos(\mathbf{g}.\mathbf{r}_{\kappa}). \qquad (3.1.8)$$

Since absorption is for the moment being ignored, this is a real quantity. Each structure phase $\phi_{\mathbf{g}}$, and each phase triplet θ, must therefore be either 0 or π in a centrosymmetric crystal. There are consequently only two types of intensity anomaly, which we shall see later are particularly easy to distinguish, in a weak-beam limit.

An extension of the method to the determination of general values of θ requires rather more analysis. Unfortunately, there seems to have been a tendency to assume (both for electrons and X-rays) that since the production of three-beam anomalies requires more than single scattering, the analysis must basically be dynamical. Thus at least two of the three beams are usually treated "exactly", and only the third as a perturbation (see eg Kambe 1957, Juretschke 1982, Høier and Marthinsen 1983, Marthinsen and Høier 1986, 1988, Shen 1986). Although it is quite natural (and usually necessary) to treat electron diffraction using dynamical theory, it is slightly surprising that only Thorkildsen (1987) seems to have given an entirely perturbative analysis of the three-beam diffraction of X-rays. Although Thorkildsen presents a forward-going theory which produces almost identical anomalies to those described below, the extra complications incurred by his treating X-rays means that inversion is not possible. As a consequence, none of the intensity expressions produced by these methods are invertible, in that a simple explicit expression for general θ in terms of simple measurable quantities cannot be produced. The best methods available all

require the knowledge of other parameters, especially the structure factor amplitudes of the reflections involved (Shen and Collela 1986, 1988), and usually at least one fitting procedure (Marthinsen and Høier 1988, Zuo Spence and Høier 1989).

The different approach given here derives from the simple result (3.1.6) that a second order Born expansion of the diffracted amplitude leads to a phase-preserving intensity. It is found that an expansion truncated at the second amplitude term *is* invertible, leading to a simple prescription for phase triplet measurement in both noncentrosymmetric and centrosymmetric crystals. Since zone-axis electron diffraction will rarely be well described by a second order Born expansion, it will be necessary to choose the experimental geometry rather carefully in order that the method be applicable. The next section begins with an introduction to such a geometry, which is then analysed to produce the promised prescription.

3.2 A PERTURBATIVE ANALYSIS OF 3-BEAM DIFFRACTION

3.2.1 The experimental geometry

The approximate diffracted amplitude $A_{\mathbf{g}}$ constructed in (3.1.5) by the addition of a single ($\mathbf{g}$) and a double ($\mathbf{h}, \mathbf{g}-\mathbf{h}$) diffraction route represents the first two terms in a Born series expansion of the true $A_{\mathbf{g}}$ in three-beam diffraction. As has been said, this would not normally be considered a good approximation in zone axis THEED which (close to the axis at least) is generally far too strong for U to be treated as a perturbation of $-\nabla^2_{\mathbf{R}}$, and involves too many strongly coupled beams to justify the inclusion of only three of them.

One of the ways to avoid these objections to a perturbative analysis is to use an experimental geometry which provides weaker diffraction than at zone axes, and with fewer beams involved. Weak diffraction may be achieved by working at large diffracting angles, since the potentials $U_{\mathbf{g}}$ fall off rapidly with g; from §2.1, the constituent $u_\kappa(\mathrm{g}) \sim \exp(-M_\kappa g^2)/g^2$ (M_κ is the Debye-Waller figure) at large g. The local regions chosen for analysis will therefore be situated well away from a strong zone axis. Although a conventional CBED technique could easily be used off-axis to excite the region around a three-beam point, the particular experimental technique used here is one developed in Bristol by Roger Vincent (Vincent and Bird 1986) which, as we shall see, provides *many* weakly diffracting three-beam situations for analysis, some of which can be made genuinely three-beam (and not four or more) by adjustment of the microscope voltage.

A "Vincent pattern" is a large convergence-angle convergent beam electron diffraction pattern taken parallel (usually) to a crystallographic axis. The convergence semi-angle of the incident probe is adjusted to be equal to (or slightly less than, in practice) the angular radius μ_1 of the first order Laue zone (FOLZ). Since the illumination is parallel to a zone axis, the reciprocal lattice may be thought of as split into layers. It turns out that a Vincent pattern, though it contains multiple overlapping discs in the zeroth layer, separates the diffraction associated with different layers n into annuli bounded by the higher order Laue zone (HOLZ) angles μ_n and μ_{n+1}. The deficit and excess lines of normal CBED patterns become chords of the FOLZ and HOLZ circles respectively. Vincent and Bird (1986) showed that the interaction between these deficit and excess lines is well approximated by kinematic theory, so our description of diffraction

in terms of the tramlines of §2.4 is appropriate out in these regions.

Figure 3.2.1 shows a 200kV Vincent pattern taken from the [6$\bar{5}$3] axis of InP, and a simulation of the pattern produced by assuming all lines to be in their kinematic positions (Preston 1987).

This particular pattern was taken with a convergence semi-angle of approximately 60% of the FOLZ radius, though the simulation has a rather larger probe so as to simulate those portions of tramlines excited by the strong diffuse regions surrounding the elastic circular region. Note that the length of the upper-layer excess lines excited elastically is determined by the length of the deficit line chord in the zero-layer, incident probe region, and that along most of the excited length the intensity is approximately constant. The deficit lines are not visible in the experimental pattern due to overexposure of the negative. The width of the simulated excess lines is intended to give some indication of the strength of the two-beam interaction associated with each set of tramlines. The other lines shown in the simulations are zero-layer tramlines, which have no elastic excitation outside the incident probe, but are seen as Kikuchi bands in the diffuse background surrounding the probe.

The regions of the pattern of interest here are those regions where an excess elastic line crosses such a diffuse Kikuchi line. At these points there is a noticeable anomaly in the two-beam intensity along the excess line; if there are only three independent beams involved, it will be shown that the shape of these intensity anomalies is governed by the value of the relevant phase triplet θ for the particular triangle of vectors considered. It is these anomalies, associated with rather weak diffraction routes which we shall analyse by perturbation theory.

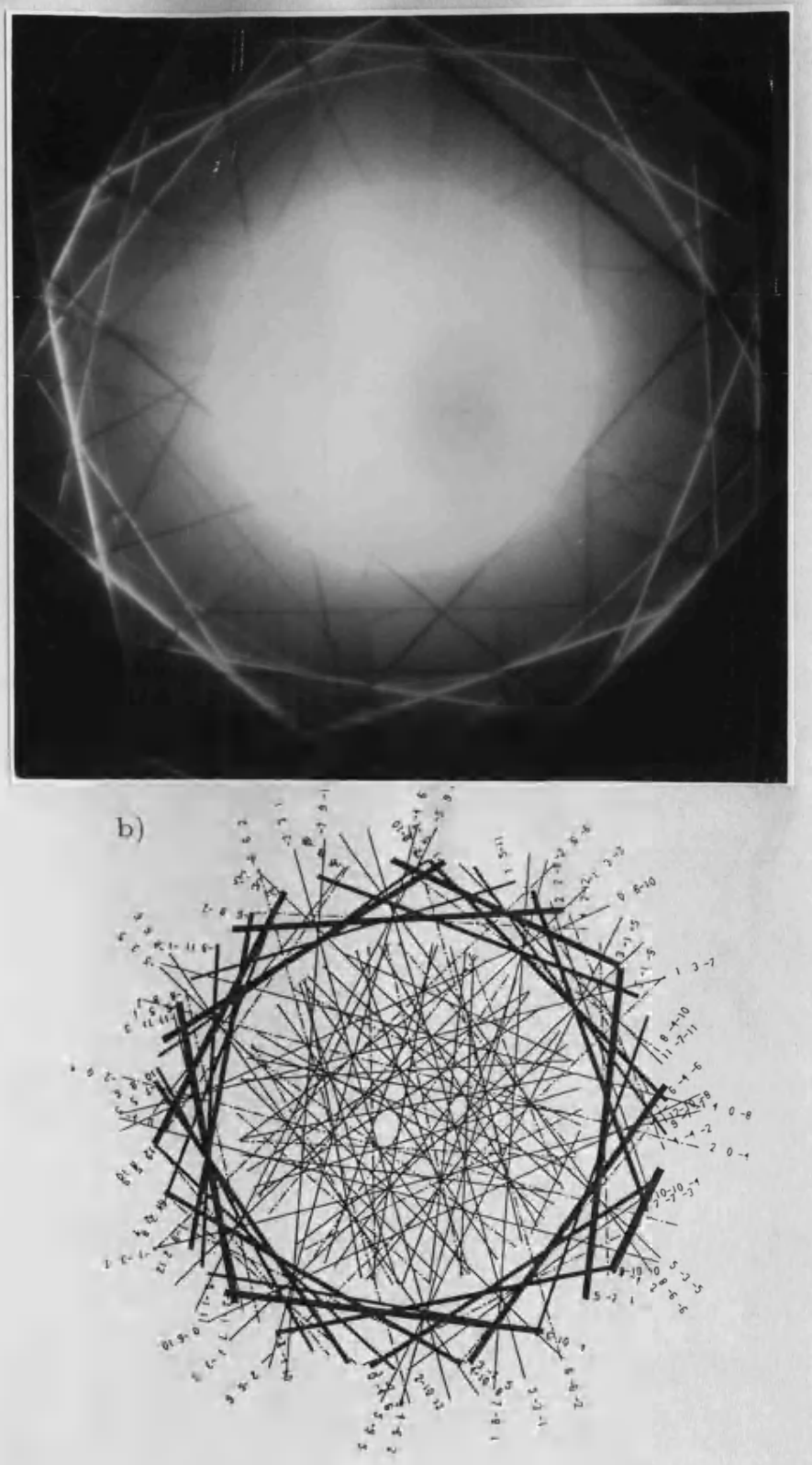

Figure 3.2.1. (a) 200kV Vincent pattern from InP[$6\bar{5}3$] (courtesy A G Wright). (b) Kinematic simulation of this pattern. The lines running across the whole pattern are zero-layer Kikuchi lines. The rest are HOLZ deficit and excess lines. Each of the latter is given a width representative of its kinematic diffraction strength.

Note from figure 3.1.1 that A is inside the inner, circular region, and B and C lie at the intersection of two different HOLZ excess lines across a given Kikuchi band. Note also that by choosing $\mathbf{g} - \mathbf{h}$ to be a zero-layer Kikuchi band, there is no primary excitation between B and C in figure 3.1.1, so the only three-beam effect observed at C will be that caused by primary excitation at A. If $\mathbf{g} - \mathbf{h}$ were not chosen in this way, then three-beam effects originating from B would also be seen at C.

The real advantage of using Vincent patterns is that there are so many three-beam anomalies excited in a single pattern; indeed the reason for choosing a relatively high-index axis such as $[6\bar{5}3]$ is to avoid there being so many excess lines that a "clean" (in that three, and only three, beams are involved) intersection with a zero-layer Kikuchi band cannot be found. To an extent this can be made easier both by adjusting the microscope voltage and by tilting up the Kikuchi band of interest. The first of these measures will alter the electron wavenumber k, and so move the upper layers relative to the zero layer. The second measure will reduce the number of extraneous lines in the region of interest. Of course, if these measures are used solely to produce one clean three-beam intersection, there is no longer any particular advantage over the use of off-axis conventional CBED patterns, except that these may prove harder to index.

Since the three-beam geometry contains only three vectors, it must clearly be planar. Furthermore, the plane of these vectors is approximately perpendicular to the incident beam direction. (Even a "large convergence-angle" CBED pattern has electrons scattered by just two or three degrees at most, so even though $\mathbf{g}$ and $\mathbf{h}$ are in fact FOLZ vectors, there is little error in describing them

as ZOLZ vectors of some other nearby, high-index axis.) Thus we simplify the analysis by using a 2-dimensional scattering potential $U(\mathbf{R})$ akin to the zero-layer projected potential of §2.2 and work in a symmetric Laue geometry, in which $\mathbf{R}$ is assumed exactly parallel to the crystal surfaces and perpendicular to the zone axis direction z. Kästner (1987) has reported that the effect of working in a general, nonsymmetric Laue geometry is usually rather small. One simple correction which can be made for a nonsymmetric Laue geometry is if the crystal is parallel-sided but tilted slightly. Then the effective depth of the specimen seen by the fast electrons will be increased.

Our starting equation will therefore be the separable THEED equation (2.2.22) with a real potential:

$$\left[-\nabla^2_{\mathbf{R}} + U(\mathbf{R})\right]\psi \;=\; 2ik\frac{\partial\psi}{\partial z}, \tag{3.2.1}$$

with boundary conditions at the depths $z = 0$ and $z = t$.

3.2.2 Full many-beam analysis

It would appear that since only three independent beams are involved, the most sensible method for the solution of (3.2.1) would be to use the many-beam equations (2.3.6). These would produce a cubic expression in the eigenvalues $s^{(j)}$; cubic equations are exactly soluble, and the many-beam equations implicitly include all terms in any perturbation series, so it would seem strange not to use them directly to solve the problem. In practice this is not possible, since the cubic polynomial is messy to solve, and leads to an intensity expression which, though correct, is prohibitively difficult to invert. However, the many-beam equations can be of considerable use in the analysis of the higher order terms

which will inevitably be ignored in the perturbative analysis which will follow. In particular, the value of phase triplet predicted by approximate intensity expressions to any order may be compared with that from "idealised experimental data" provided by the many-beam equations, to deduce the systematic error incurred in truncating the series. It is convenient to introduce the many-beam representation at this stage since it illustrates rather nicely how the problem may be parameterised using just six dimensionless terms.

With the potential $U(\mathbf{R})$ for the moment real, the hermitian version of the many-beam equations (2.3.6) is appropriate. Before expanding these equations to produce the actual 3×3 secular equation which must be solved, there are considerable simplifications which can be made; for these we refer to the planar three-beam geometry sketched in figure 3.2.2.

As in the two-beam case of §2.4, the reciprocal space origin O is not nearly so convenient to use as is an origin at the exact Bragg condition orientation. We therefore define

$$\mathbf{K} = \mathbf{K_0} + \delta\mathbf{K} \tag{3.2.2}$$

where $\mathbf{K_0}$ is the incident orientation of the exact three-beam point (at A in figure 3.2.2). Note now that $\delta\mathbf{K}$ also describes the deviation from the point of *observation* of three-beam effects, at either B or C in the figure. A certain amount of duplicity will therefore ensue, in describing A, B and C as "three-beam" points, since the deviation from each may be described using the same coordinate; in truth A is the only genuine three-beam point, as it the only one inside the incident probe. With the incident orientation $\mathbf{K}$ written this way, the

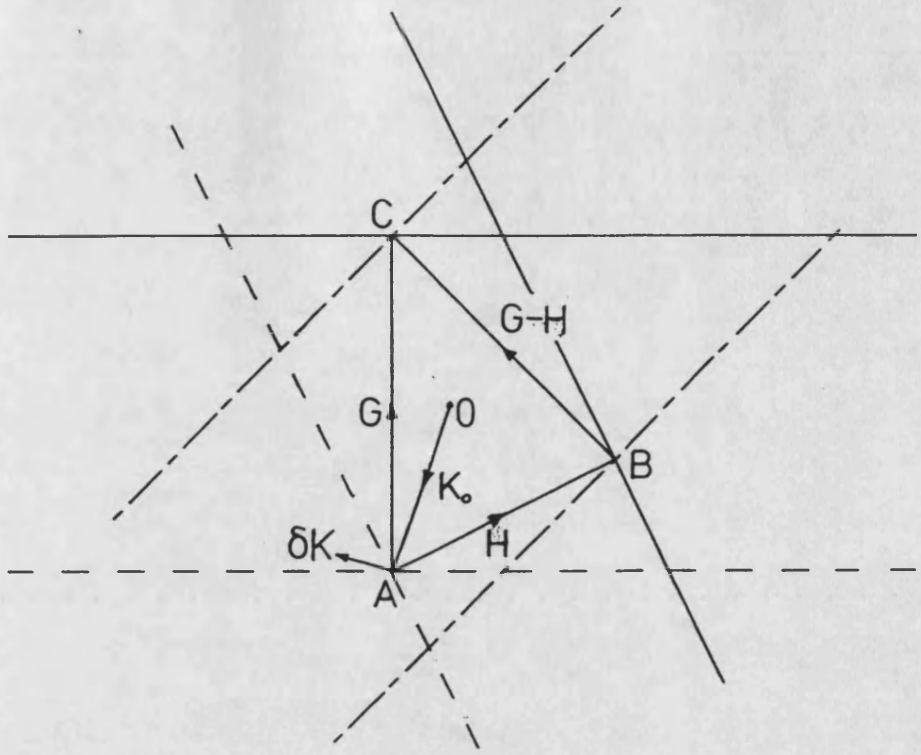

Figure 3.2.2. The geometry of a Vincent pattern three-beam point. Dashed lines indicate incident orientations, full lines represent excess diffracted lines, and dot-dashed lines represent zero-layer Kikuchi lines. O is the reciprocal space origin.

diagonal terms in the many-beam equations become

$$(\mathbf{K}+\mathbf{G}')^2 = [(\mathbf{K_0}+\mathbf{G}')+\delta\mathbf{K}]^2 = (\mathbf{K_0}+\mathbf{G}')^2 + 2(\mathbf{K_0}+\mathbf{G}').\delta\mathbf{K} + \delta\mathbf{K}^2 \tag{3.2.3}$$

where $\mathbf{G}'$ is $\mathbf{0}, \mathbf{G}$ or $\mathbf{H}$. Now, from the definition of tramlines in §2.4, or by inspection of figure 3.2.2, it is seen that OA=OB=OC, so $(\mathbf{K_0}+\mathbf{G}')^2 = \mathbf{K_0}^2$ for all three $\mathbf{G}'$. Thus the only variable term down the diagonal of the many-beam matrix is $2\mathbf{G}'.\delta\mathbf{K}$. All the other terms are constant, and are therefore irrelevant to the structure of the solution, as they can be absorbed into the overall z-dependent phase $\exp(-is^{(j)}z/2k)$, as was the refractive potential U_0

in the derivation of the many-beam equations.

The diagonal terms are now in a form very similar to that of the two-beam deviation parameter $W = \mathbf{G}.\delta\mathbf{K}$. In this three-beam case, it is convenient to express the deviation of the incident electron wavevector from the exact three-beam point, using the parameters

$$x = \mathbf{H}.\delta\mathbf{K}\frac{t}{2k} \qquad y = \mathbf{G}.\delta\mathbf{K}\frac{t}{2k} \tag{3.2.4}$$

which are essentially the same as W, but with the slight difference that they are made dimensionless quantities by multiplication of the $t/2k$ factor. Here t is the crystal thickness and k the wavenumber of the incident electrons. As an aid to interpretation, note that the line $y = 0$ defines the two-beam tramline for diffraction by $\mathbf{G}$, and that along this line, $+x$ points *into* the Kikuchi band $\mathbf{G} - \mathbf{H}$.

Having rendered the deviation parameters dimensionless, it is natural to do the same to the potentials $U_{\mathbf{G}}$. Thus we define

$$\beta_{\mathbf{G}'} = \frac{|U_{\mathbf{G}'}|t}{2k} = \frac{\pi t}{\xi_{\mathbf{G}'}} \tag{3.2.5}$$

where $\mathbf{G}'$ now takes the values $\mathbf{G}, \mathbf{H}$ and $\mathbf{G} - \mathbf{H}$, and ξ is the two-beam extinction distance of §2.4. These "diffraction strengths" β turn out to be the most natural perturbation expansion parameters, so it is these which should be kept as small as possible for our approach to be valid. As we shall see, $\beta = 1$ will represent the "turnover" value, above which a Born expansion is inappropriate. [This clearly implies, not surprisingly, that another way to achieve weak diffraction is to reduce t or increase k, neither of which is particularly easy experimentally.]

Expansion of the many-beam equations (2.3.5) using these dimensionless parameters x, y and β yields the secular equation for three-beam diffraction

$$\begin{vmatrix} -s & \beta_{\mathbf{G}}\exp(-i\phi_{\mathbf{G}}) & \beta_{\mathbf{H}}\exp(-i\phi_{\mathbf{H}}) \\ \beta_{\mathbf{G}}\exp(i\phi_{\mathbf{G}}) & 2y-s & \beta_{\mathbf{G}-\mathbf{H}}\exp(i\phi_{\mathbf{G}-\mathbf{H}}) \\ \beta_{\mathbf{H}}\exp(i\phi_{\mathbf{H}}) & \beta_{\mathbf{G}-\mathbf{H}}\exp(-i\phi_{\mathbf{G}-\mathbf{H}}) & 2x-s \end{vmatrix} = 0, \qquad (3.2.6)$$

where the s is not the same as in (2.3.6) because of the absorption of extra terms into the leading diagonal. Expansion of this cubic equation in s would show that three-beam diffraction is described entirely, and generally, by the six parameters x, y, the three β and the phase triplet

$$\theta = \phi_{\mathbf{H}} + \phi_{\mathbf{G}-\mathbf{H}} - \phi_{\mathbf{G}}. \qquad (3.2.7)$$

However, the intensity expression produced by such an expansion of the many-beam equations cannot be inverted to give an explicit expression for θ in terms of some or all of the other five parameters.

Since each component of the determinant (3.2.6) has been scaled by the factor $t/2k$, and since the normalisation of the Bloch wave coefficients C is not affected by this scaling, the resulting many-beam diffracted amplitude will be given by (see 2.3.10)

$$A_{\mathbf{G}}(x,y) = \sum_{j=1}^{3} C_{\mathbf{0}}^{(j)*}(x,y)C_{\mathbf{G}}^{(j)}(x,y)\exp\left\{-is^{(j)}(x,y)\right\}, \qquad (3.2.8)$$

and may simply be scaled for another thickness t' (say) by multiplication of the term in braces by t'/t. Figure 3.2.3 shows a typical three-beam intensity anomaly computed from the many-beam equations. This "exact" anomaly will later be compared with a perturbation approximation to it.

Note that in the plots of intensity as a function of orientation, x and y will be drawn as if they are orthogonal. This is in fact never the case in the geometry

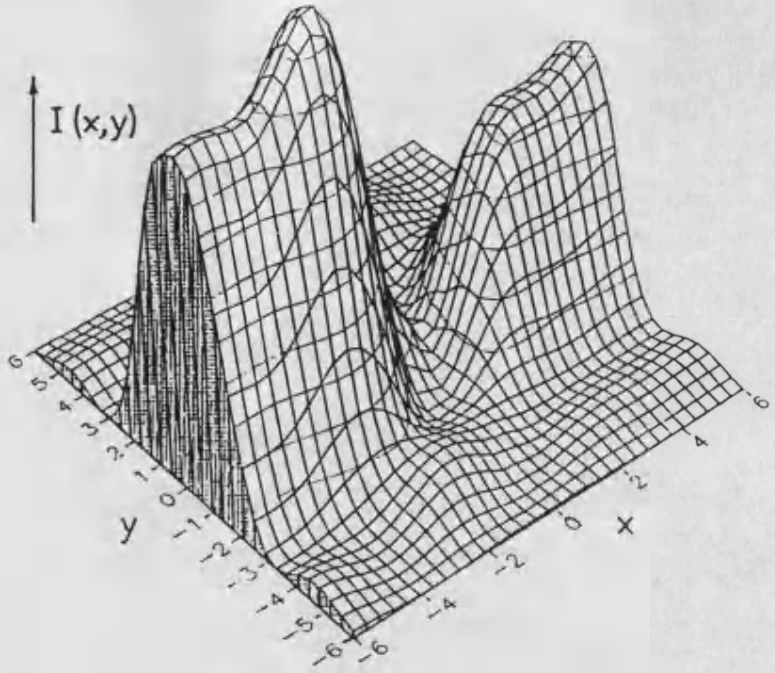

Figure 3.2.3. A typical Vincent pattern three-beam intensity anomaly computed from the many-beam equations. The input parameters are $\beta_{\mathbf{G}} = 0.4, \beta_{\mathbf{H}} = 0.6, \beta_{\mathbf{G}-\mathbf{H}} = 0.8$ and $\theta = 140°$. $x = 0, y = 0$ is the exact three-beam point, and $y = 0$ defines the excess line for diffraction by $\mathbf{G}$.

we consider, but since the diffraction has been completely parameterised, and is therefore described in its most general terms, it is convenient to keep the interaxial angle constant. In practice a better simulation to experiment can easily be achieved by a simple shear of the axes. The fact that the plots are general means that, for example, the width of the basic excess line $y = 0$ appears to be independent of the strength of the $\mathbf{G}$ reflection. It is, of course, a relatively straightforward procedure to convert the parameterised results back into the original variables and coordinates, if required.

3.2.3 Development of the perturbation expressions

We now go on to derive a Born series expansion for three-beam diffraction, based

on the Howie-Whelan equations of §2.3.2. As was mentioned there, the particular form of expansion used is entirely analogous to that used in the time-dependent perturbation theory of low-energy quantum mechanics (eg Schiff 1968), where the unperturbed Hamiltonian is here taken to be the kinetic energy term $\widehat{H}_\circ = -\nabla^2_{\mathbf{R}}$ with eigenstate

$$\psi_\circ = \exp(i\mathbf{K}.\mathbf{R})\exp(-iK^2z/2k) \tag{3.2.9}$$

and the perturbation is the (elastic) potential $U(\mathbf{R})$, causing changes in the transverse wavevectors $\mathbf{K} \rightarrow \mathbf{K} + \mathbf{G}$. Note that the perturbation is not itself depth-dependent, so what we shall derive is the depth *evolution* of the electron wavefunction as is passes through, and is scattered by, the crystal. As promised, the starting point for the analysis is the Howie-Whelan equations (2.3.14):

$$\frac{da_{\mathbf{G}}}{dz} = \frac{1}{2ik}\sum_{\mathbf{G}'} a_{\mathbf{G}'}(z)U_{\mathbf{G}-\mathbf{G}'}\exp(i\Delta_{\mathbf{G}\mathbf{G}'}z/2k), \tag{3.2.10}$$

where

$$\Delta_{\mathbf{G}\mathbf{G}'} = \left\{(\mathbf{K}+\mathbf{G})^2 - (\mathbf{K}+\mathbf{G}')^2\right\}. \tag{3.2.11}$$

The sum in this three-beam case is over the vectors $\mathbf{0}, \mathbf{G}$ and $\mathbf{H}$, with the condition $\mathbf{G} \neq \mathbf{G}'$ imposed so that the refractive contribution $U_{\mathbf{0}}$ is ignored. The same parameterisation will presently be introduced here as was used in the many-beam representation, which will again simplify the equations considerably.

In keeping with time-dependent perturbation theory, the contributions to $a_{\mathbf{G}}$ (say) are now separated into different "orders". In this case the order of a contribution refers to the number of individual Bragg reflections which combine to produce net reflection by $\mathbf{G}$. Thus the zeroth order terms represent the initial

or boundary conditions, the first order terms kinematic (ie single scattering) diffraction and so on. The separation is achieved by writing $U \rightarrow \lambda U$ and expressing

$$a_{\mathbf{G}} = \sum_{s=0}^{\infty} \lambda^s a_{\mathbf{G}}^{(s)}. \tag{3.2.12}$$

This is assumed an analytic function of λ for $0 \leq \lambda \leq 1$. The series (3.2.12) is substituted in (3.2.10), the coefficients of corresponding powers of λ equated, and finally λ is set equal to 1. The substitution yields

$$\frac{da_{\mathbf{G}}^{(0)}}{dz} = 0 \tag{3.2.13}$$

and

$$\frac{da_{\mathbf{G}}^{(s+1)}}{dz} = \frac{1}{2ik} \sum_{\mathbf{G}'} a_{\mathbf{G}'}^{(s)} U_{\mathbf{G}-\mathbf{G}'} \exp(i\Delta_{\mathbf{G}\mathbf{G}'} z/2k). \tag{3.2.14}$$

The "initial" condition in this "time"-dependent problem is just the amplitude of the wavefunction ψ at the entrance surface of the crystal. In the symmetric Laue geometry, with the incident beam taken to be the plane wave ψ_o of (3.2.9), this will give

$$a_{\mathbf{G}}^{(0)}(z=0) = \delta_{\mathbf{G},\mathbf{0}} \tag{3.2.15}$$

where δ is the Kronecker delta. Substitution of (3.2.15) into (3.2.14) leads to an integral for $a_{\mathbf{G}}^{(1)}$ in terms of $a_{\mathbf{G}}^{(0)}$. Once $a_{\mathbf{G}}^{(1)}$ is known, it may form the basis for a similar integral for the second order amplitude $a_{\mathbf{G}}^{(2)}$, and in general the $(s+1)$th term may be found by integration from the sth term. The approximate amplitude to any order n may then be found by truncating the series $a = a^{(0)} + a^{(1)} + \cdots$ at the $a^{(n)}$ term. Such a truncation will produce an amplitude correct to order n in the diffraction strengths β, and since from (3.2.15) only the

straight-through beam has a zeroth order component, will lead to an intensity expression for ($\mathbf{G} \neq \mathbf{0}$) correct to order $n+1$ (see §3.3.1).

Now, for the three-beam expansion of the Howie-Whelan equations, the same parameters may be used as were introduced for the many-beam representation, namely x, y, β, θ. However, because the production of the $(s+1)$th term involves an integral over z of the (s)th term, and the parameterisation involves only the total thickness t, these parameters are easiest to introduce at the last step of the calculation.

Attention will now be limited to net diffraction by $\mathbf{G}$ rather than $\mathbf{H}$; that is from A to C in figure 3.2.2. This choice is completely arbitrary. We begin by noting that with the origin shifted by $\mathbf{K_0}$, $\Delta_{\mathbf{GG'}} = 2(\mathbf{G}-\mathbf{G'}).\delta\mathbf{K}$ [see (3.2.3)].† Using the initial condition (3.2.15) to remove the $\mathbf{G'}$ summation for the $s=0$ term in (3.2.14) leads to the integral for the first order amplitude diffracted by $\mathbf{G}$

$$a_{\mathbf{G}}^{(1)}(t) = \frac{1}{2ik}\int_0^t dz\, U_{\mathbf{G}} \exp\left(i2\mathbf{G}.\delta\mathbf{K}\frac{z}{2k}\right). \qquad (3.2.16)$$

When integrated, all the terms may be written in their parameterised form. It is convenient to define the function $f(X) = \sin(X)/X$, which frequently occurs in the resulting amplitudes. This occurrence is not surprising since $f(X)$ is the basic slit-diffraction response function familiar in kinematic diffraction theory

† With this simplification, the Howie-Whelan equations (3.2.10) may be derived using the better approximation $\delta K \ll k$ rather than $K \ll k$ used in the small angle scattering approximation of Chapter 2, provided k is replaced by $k_z = \sqrt{k^2 - K_0^2}$.

(eg Cowley 1981). The integrated first order amplitude is

$$a_{\mathbf{G}}^{(1)}(t) \;=\; -i\beta_{\mathbf{G}} \exp(i\phi_{\mathbf{G}}) \exp(iy) f(y). \tag{3.2.17}$$

A similar process may be used to find the higher order amplitudes. The second order amplitude $a_{\mathbf{G}}^{(2)}(t)$ arises from integration of the two first order terms $a_{\mathbf{0}}^{(1)}(z)$ and $a_{\mathbf{H}}^{(1)}(z)$. The first of these is zero, and the second identical in form to $a_{\mathbf{G}}^{(1)}(z)$. It is therefore a straightforward process to derive $a_{\mathbf{G}}^{(2)}(t)$, which after parameterisation is

$$a_{\mathbf{G}}^{(2)}(t) = \frac{i\beta_{\mathbf{H}}\beta_{\mathbf{G}-\mathbf{H}} \exp i(\phi_{\mathbf{H}} + \phi_{\mathbf{G}-\mathbf{H}})}{2x} \left\{ \exp(iy) f(y) - \exp i(y-x) f(y-x) \right\}. \tag{3.2.18}$$

As expected, these expressions contain the dependence on the $U_{\mathbf{G}}$ suggested in §3.1.2, plus a geometrical factor akin to the dynamical shape factor of Moodie (1972). Hence the resulting intensity expression found from these two amplitudes will introduce the desired phase triplet θ. We therefore choose to truncate the amplitude series at the second term so that the resulting (third order) intensity expression will be the simplest possible to invert. The implications for the practical application of the method of ignoring all higher order terms is examined in §3.3.1. Combining the amplitudes (3.2.17) and (3.2.18) gives an approximate total amplitude

$$A_{\mathbf{G}} \approx a_{\mathbf{G}}^{(1)} \left[1 - \frac{\beta_{\mathbf{H}}\beta_{\mathbf{G}-\mathbf{H}}}{\beta_{\mathbf{G}}} . \frac{\exp(i\theta)}{2x} . \left\{ 1 - \exp(-ix) \frac{f(y-x)}{f(y)} \right\} \right]. \tag{3.2.19}$$

The approximate intensity may then be calculated from the modulus squared of this amplitude. To third order in the parameters β (the fourth order term

$|a^{(2)}|^2$ is dropped) the intensity is found to be

$$I_{\mathbf{G}}(x,y) = \beta_{\mathbf{G}}^2 f^2(y) + \beta_{\mathbf{G}}\beta_{\mathbf{H}}\beta_{\mathbf{G}-\mathbf{H}} f(x)f(y)f(y-x)\sin\theta - \beta_{\mathbf{G}}\beta_{\mathbf{H}}\beta_{\mathbf{G}-\mathbf{H}}\frac{f^2(y)}{x}\left\{1 - \frac{f(y-x)}{f(y)}\cos x\right\}\cos\theta. \tag{3.2.20}$$

Due to the parameterisation pursued throughout, this is a general expression, applicable to all three-beam diffraction. The same expression may be converted to describe the three-beam anomaly to diffraction by **H** (observable at B in figure 3.2.2), by interchanging all references to **G** and **H**, including the x and y coordinates.

Figure 3.2.4 shows generic plots of the three geometrical factors involved in (3.2.20). The first is the kinematic approximation to the excess line profile, centred along the line $y = 0$.

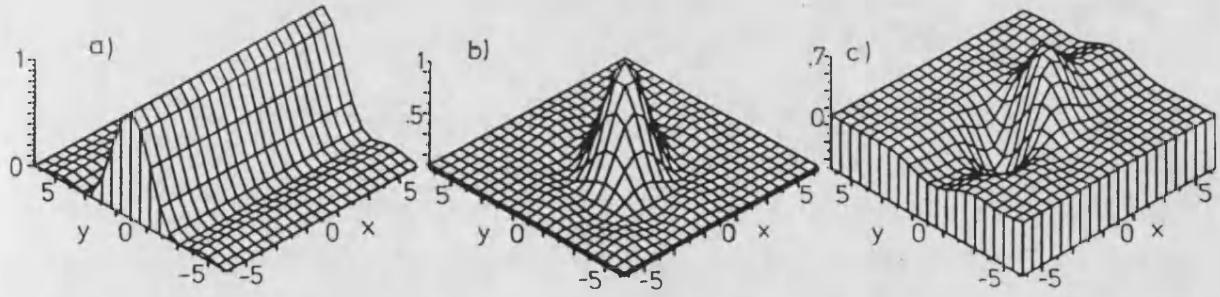

Figure 3.2.4. The three terms (kinematic, $\sin\theta$ and $\cos\theta$ respectively) of the approximate intensity expression (3.2.20).

The two phase-dependent terms are seen to produce an intensity anomaly to this excess line around the exact three-beam point $x = 0$, $y = 0$. The shape of this anomaly will be shown to be a unique function of the desired phase triplet θ. As a specific example, note that for a centrosymmetric crystal, in which θ is either 0 or π, the $(\sin\theta)$ term vanishes, and the sign of the $(\cos\theta)$ term will be different

for $\theta = 0$ and $\theta = \pi$; the two cases are therefore easily distinguishable. This is consistent with the strong diffraction observations of Kambe (1957). Figure 3.2.5 is the approximation to the "exact" anomaly of figure 3.2.3, for the same diffraction strengths β and phase triplet θ.

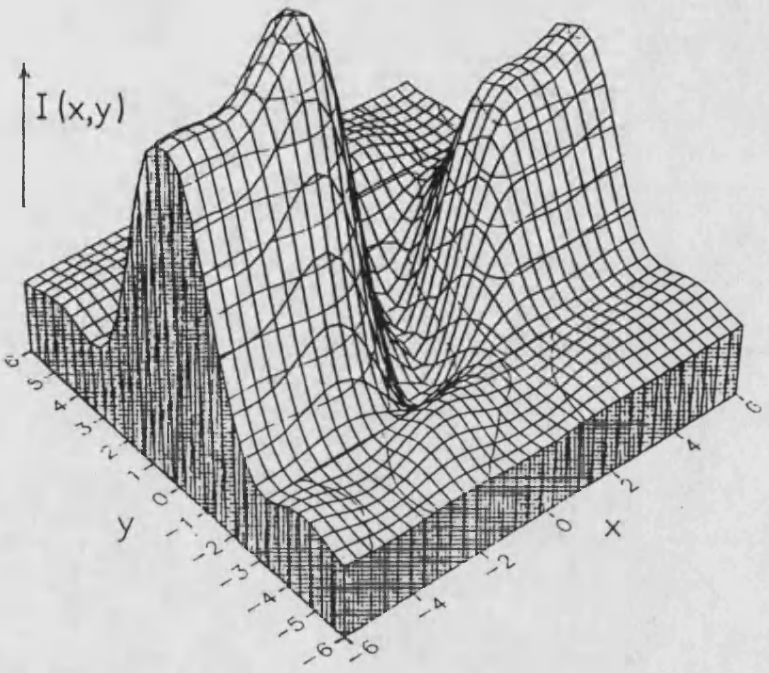

Figure 3.2.5. Approximate intensity anomaly for the same diffraction parameters as figure 3.2.3. Note that the zero level is some way up the vertical axis, due to the approximation producing negative intensities.

In general the exact and approximate intensity anomalies are found to be very similar up to $\beta \sim 1$. This point will be returned to in §3.3.1.

3.2.4 A simple prescription for phase measurement

The task now is to invert (3.2.20) to express θ in terms of simple measurable quantities. Since (3.2.20) contains so few parameters, it is clear that these measurable quantities can only be intensity, diffraction strength, or values of the

orientation coordinates x and y. Of these, by far the most preferable to use in a measurement prescription are the orientations x and y, since they are manifested as *displacements* in a CBED pattern, and as such can easily be related to other known displacements in a pattern, such as the distance between an excess and deficiency line. Of the others, absolute intensities are unreliable due to the effects of absorption, and even relative intensities suffer from problems due to the nonlinear nature of photographic processes. [All the patterns taken in this thesis have been recorded on film.] Finally, it would be preferable not to have to know structure-factor amplitudes before being able to measure structure-factor phases, so the β are not ideal as measurable quantities in a θ prescription. As mentioned in the introduction to this chapter, all of the other techniques for phase invariant measurement published so far *do* require the structure amplitudes to be included in the analysis, usually as fitting parameters.

One of the more striking features of the approximate anomalies in figures 3.2.4 and 3.2.5 is that all the strong maxima and minima lie along the ridge of the excess line, $y = 0$. If the diffraction strengths involved become large ($\beta \gg 1$), this is no longer true, and the crossing Kikuchi and excess lines tend to "hybridise" into two hyperbolically asymptotic lines (eg Kambe 1957, Marthinsen and Høier 1986). In Vincent patterns, however, the principal features do appear to lie along the excess tramline ridge, $y = 0$. Setting $y = 0$ in (3.2.20), the phase dependent terms become

$$\Delta I_{\mathbf{G}}(x,0) \;=\; \beta_{\mathbf{G}}\beta_{\mathbf{H}}\beta_{\mathbf{G}-\mathbf{H}} \left\{ \frac{f(2x)-1}{x} \cos\theta + f^2(x) \sin\theta \right\}. \qquad (3.2.21)$$

Figure 3.2.6 shows a series of plots of the term in braces in this ridge intensity anomaly for various values of θ.

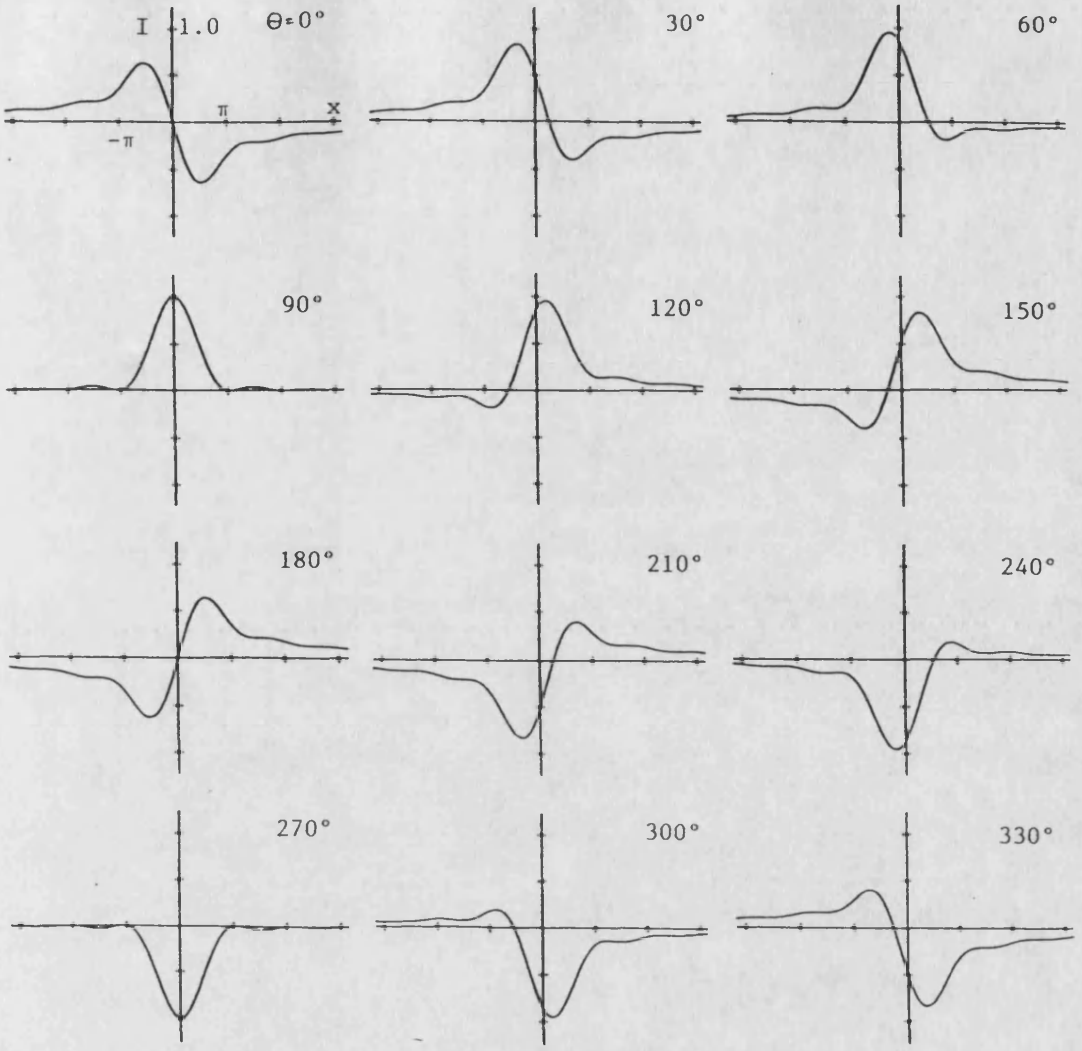

Figure 3.2.6. Excess line ($y = 0$) intensity anomalies about the exact three-beam point $x = 0$, as a function of phase triplet θ. x positive goes into the Kikuchi band.

As promised, the shape of each anomaly is uniquely determined by θ, so it should be possible to produce a one-to-one correspondence between some measurement of this shape and a value of θ. One possibility would be to look at the relative fall-off of the anomaly intensity either side of the three-beam point, but this would of course require the measurement of relative intensities. The most striking feature of the ridge anomalies in figure 3.2.6 is that the positions of the principal

maximum and minimum are both monotonically increasing functions (mod 2π) of θ, suggesting that the positions of these extrema might lead to a "distance-only" measurement prescription. Differentiating the term in braces in (3.2.21) gives

$$\frac{\partial \Delta I(x,0)}{\partial x} \propto \frac{\cos\theta}{x^2}\left[1 - \frac{\sin 2x}{x} + \cos 2x\right] + \frac{\sin\theta}{x^2}\left[\frac{1}{x}(\cos 2x - 1) + \sin 2x\right] \tag{3.2.22}$$

which is of course zero at maxima and minima. The trivial solution is for $x \to \pm\infty$; that is, the intensity profile well away from the three-beam point returns to that of a normal excess line. The right hand side of (3.2.22) is also zero when

$$\tan\theta = \frac{\frac{\sin 2x_e}{x_e} - \cos 2x_e - 1}{\frac{1}{x_e}(\cos 2x_e - 1) + \sin 2x_e} \tag{3.2.23}$$

where x_e denotes an extremum value of x. Expansion of the double angle terms in this expression yields

$$\tan\theta = -\cot x_e = \tan\left(x_e - \frac{\pi}{2}\right), \tag{3.2.24}$$

or, since the tangent function has period π,

$$\theta = x_e + \left(n - \frac{1}{2}\right)\pi \tag{3.2.25}$$

(n is an integer). This is a remarkably simple result, which is completely obscured in the full many-beam analysis. What it implies is that of all the six parameters involved in three-beam diffraction, a simple approximate linear relationship exists between the desired phase triplet and the single orientation parameter x. As a bonus, that parameter describes *distances* in an electron micrograph. Thus a value of θ can in principle be measured without the knowledge

of the structure factor amplitudes, crystal thickness or microscope voltage, and without the measurement of intensities. If attention is limited to the principal extrema, closest to the exact three-beam point, then it is found (see figure 3.2.6) that $n = 0$ for the minimum x_{min} and $n = 1$ for the maximum x_{max}. Thus the actual prescription for phase measurement is

$$\theta = x_{min} - \frac{\pi}{2} = x_{max} + \frac{\pi}{2}. \tag{3.2.26}$$

That is, we need only find the position of either the maximum or minimum in a three-beam anomaly relative to the exact three-beam point (the centre of the Kikuchi line in our case) to determine the value of a phase triplet. In addition, of course, we need to define a distance scale in the micrograph (x is a dimensionless coordinate). If the position of both the maximum and minimum is detectable, then this is done simply by observing that from (3.2.26)

$$|x_{max} - x_{min}| = \pi. \tag{3.2.27}$$

Defining the actual distance between the maximum and minimum as Δx, the measured value of θ in radians will then be given as

$$\theta = \left(\frac{x_{max}}{\Delta x} + \frac{1}{2}\right)\pi = \left(\frac{x_{min}}{\Delta x} - \frac{1}{2}\right)\pi, \tag{3.2.28}$$

where x_{max}, x_{min} and Δx are now all in micrograph units. Note again from figure 3.2.6 that the determination of phase triplets in centrosymmetric crystals is very easy in the weak-beam case, since the anomaly is bright either on the inside ($\theta = \pi$) or outside ($\theta = 0$) of the Kikuchi band.

In practice, figure 3.2.6 shows that either the maximum or the minimum may be rather weak. In this case it is wise to trust only the position of the stronger

extremum (see §3.3), so the distance scale must be set by other means. One possibility is to use the two-beam rocking curve fringes of some other excess line in the pattern. Since the shape and spacing of these fringes is well understood, they may serve as a bridge between actual deviation parameters and measurable distances in the micrograph. Such a definition of distance constitutes an effective measurement of the crystal thickness [see (3.2.4) and §3.4].

To summarise, then, a prescription for the measurement of crystallographic phase invariants has been derived, based on a second order Born expansion of three-beam diffraction. The prescription (3.2.26, 3.2.28) requires only the measurement of the position of the maximum and/or minimum in the three-beam intensity anomaly, relative to the exact three-beam point. As will discussed in §3.4, the most difficult task in practice is to locate the position of the exact three-beam point $x = 0$, as this lies in the "centre" of the diffusely scattered Kikuchi line, and this centre is not easy either to define or to detect. Before going on to this, however, it is necessary to know the sensitivity of these extremal positions to the higher order terms in the Born expansion, and to absorption. The next section is therefore given to a study of this sensitivity.

3.3 FURTHER ANALYSIS OF THREE-BEAM DIFFRACTION

This section addresses some of the points raised earlier in the chapter but not discussed in any detail. In particular, an analysis is performed of the likely error induced in the prescription (3.2.26) by the neglect both of the higher order terms in the Born expansion, and of an absorptive contribution to the scattering potential.

3.3.1 The effect of higher order perturbation terms

The prescription derived in §3.2 is so simple that the truncation of the amplitude series at the second term is justifiable on the grounds that it leads to an interesting result. It is necessary, however, that we know just how useful and applicable this result is in experimentally realisable situations. If all the β involved are very small then clearly the prescription as it stands will produce reliable values of θ. In practice, the necessity to be able to detect both the excess line over the diffuse background and the centre of the Kikuchi line requires that some of the β involved may be at least of order unity.

This first section discusses at some length the effect on the prescription of the higher order terms in the perturbation expansion. In particular, the effects on the diffracted excess line intensity of the next amplitude term $a_{\mathbf{G}}^{(3)}$ is studied, and the idea of a mean diffraction strength $\overline{\beta}$ introduced, which makes possible a general systematic error analysis using the numerical many-beam intensities.

We begin with an aside on the nomenclature for the *order* of an an approximation. Since only the straight-through beam has a zeroth order amplitude term $a_{\mathbf{0}}^{(0)}$, the *first* order amplitude term for diffraction into $\mathbf{G}$ (say) will give intensities correct to *second* order in the β. In general, if the amplitude is expanded to order m, the resulting dark-field intensity (ie $I_{\mathbf{G}\neq\mathbf{0}}$) will be good to order $m+1$. Thus the prescription of §3.2 is based on the inversion of a *third* order intensity expression.

As already stated, $a_{\mathbf{G}}^{(n)}$ gives the total amplitude diffracted into $\mathbf{G}$ via all n-step routes, where for three-beam diffraction the possible steps are $\pm\mathbf{G}, \pm\mathbf{H}$ and

$\pm(\mathbf{G}-\mathbf{H})$. Since $a^{(n)}$ is the nth term in a series expansion, it may be written in the form

$$a^{(n)} \propto \frac{P_n \overline{\beta}^n Z_n}{n!}, \tag{3.3.1}$$

where $\overline{\beta}$ is some mean diffraction strength (to be defined later), Z_n is essentially the shape function of the diffraction feature (see Moodie 1972), and P_n is the number of possible n-step routes starting at the three-beam point (A in figure 3.3.1), and terminating on the **G** excess tramline (C). The $n!$ term comes from the repeated integration of the exponentials $\exp(i\Delta_{\mathbf{GG'}}z/2k)$ in (3.2.14). It is reasonable to expect that $Z_n \sim 1$, and for experimental reasons the mean diffraction strength will also be of order unity. Thus the rate of convergence of the Born series depends on the behaviour of the ratio $P_n/n!$ as n increases.

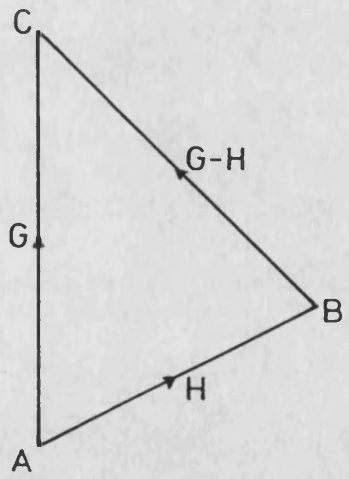

Figure 3.3.1. Three-beam geometry. Electrons incident at A have P_n n-step routes by which they may reach the point of observation C.

To find P_n, note that at each node of the triangle ABC in figure 3.3.1 there are two possible steps to other nodes. Therefore, the total number of n-step routes beginning at A (as each must) is 2^n. Of these, P_n terminate at C, and $(2^n - P_n)$

at either A or B. Since the only way to produce an $(n+1)$th route terminating at C is to have the first n steps terminating at A or B, it follows that

$$P_{n+1} = 2^n - P_n. \tag{3.3.2}$$

This inductive definition (for which $P_0 = 0$) may be written as a geometric progression in powers of (-2), yielding the explicit expression

$$P_n = \frac{1}{3}[2^n - (-1)^n]. \tag{3.3.3}$$

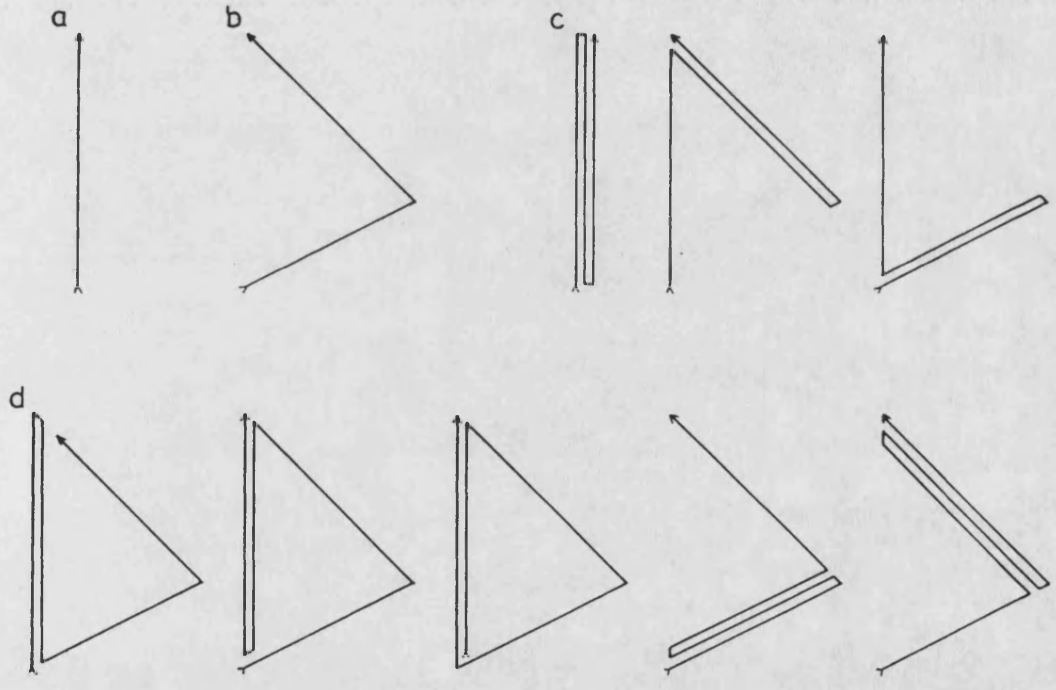

Figure 3.3.2. Possible n-step routes from A to C in figure 3.3.1 for n equal to (a)1, (b)2, (c)3 and (d)4.

Perhaps not surprisingly, P_n is the nearest integer to $2^n/3$. Figure 3.3.2 shows the possible n-step routes for n up to 4. It is clear that the higher order amplitude and intensity terms will quickly become difficult to manage analytically due to

the large number of contributions, so truncation of the amplitude series at a higher term would not lead to an invertible intensity expression.

Since these higher order terms cannot be incorporated into the prescription, it only remains to find what effect they will have on measured values of the phase triplet. Table 3.3.1 shows the values of $P_n/n!$ for different n, which for $Z_n = 1$ and $\overline{\beta}$=1 represents the relative strength of the nth order amplitudes. It is clear from this that the possible effects of at least the third order amplitude term on the prescription of §3.2 should be understood. Towards the end of this section the full many-beam solution to the three-beam diffraction equations will be used to investigate the effect of *all* higher order terms, but there is first some advantage in taking an analytical and pictorial look at how such terms arise.

n	1	2	3	4	5	6	7
P_n	1	1	3	5	11	21	43
$P_n/n!$	1	0.5	0.5	0.208	0.092	0.029	0.009

Table 3.3.1. The number of nth order amplitude routes for net diffraction by **G**, and the relative strength of each for unit β and shape function.

The first intensity term neglected in §3.2 is fourth order in β. Just as the third order intensity was constructed from the $a^{(1)}$ and $a^{(2)}$ terms, so may the intensity term $I^{(m)}$ be constructed from combinations of $a^{(s)}$ and $a^{(r)}$ for any $s + r = m$. Thus the fourth order intensity $I_{\mathbf{G}}^{(4)}$ is constructed by the combination of the second order route with itself $(a^{(2)}.a^{(2)})$ and the first order route with the three third order routes $(a^{(1)}.a^{(3)})$ of figure 3.3.2.

Now, a phase-dependent intensity expression must include the combination of

phases $+\theta$ or $-\theta$, as defined in (3.2.7). This can only be achieved if all three reflections $\mathbf{G}, \mathbf{H}$ and $\mathbf{G}-\mathbf{H}$ are excited, since the phase of each appears in (3.2.7). Consequently, phase-dependent intensities will always be associated with combinations of amplitude diagrams (figure 3.3.2) which give a closed triangle. For example, the $a^{(1)}$ and $a^{(2)}$ diagrams combine to give a single closed triangle. By contrast, none of the fourth order combinations closes the triangle, so none of the fourth order terms will be phase dependent. This means that the fourth order terms will have less effect on the shape of the three-beam anomaly, and hence on the position of the extrema, than at first expected. Similarly, from figure 3.3.2, it is clear that *all* the fifth order contributions are phase dependent, though these are considerably smaller than the third order terms, even for $\beta \sim 1$. The sixth and higher order intensities are found to contain mixtures of phase dependent and independent terms.

For the moment attention will be confined to the fourth order intensity term. From the pictorial arguments above, there will be four such terms. However, one of these is irrelevant to the discussion here; the combination of the first order term and the first third order term contains only the $\pm\mathbf{G}$ reflections, producing an intensity term proportional to $\beta_{\mathbf{G}}^4$, which is just the second term in the expansion of the two-beam intensity (2.4.1) at the exact Bragg condition $W = 0$:

$$I_{\mathbf{G}} = \sin^2 \beta_{\mathbf{G}} = \beta_{\mathbf{G}}^2 - \frac{1}{3}\beta_{\mathbf{G}}^4 + \cdots \tag{3.3.4}$$

All two-beam terms must be constant along the excess line ridge $y = 0$, so they cannot alter the position of the extrema of interest, and are therefore of no further interest in this context.

It is a straightforward though messy process to integrate the $a^{(2)}$ to produce the $a^{(3)}$ terms, and hence the relevant fourth order intensity anomalies $I^{(4)}$. The results are shown graphically in figure 3.3.3. These plots are generic shape functions; they should be multiplied by $\beta_{\mathbf{H}}^2\beta_{\mathbf{G}-\mathbf{H}}^2, \beta_{\mathbf{G}}^2\beta_{\mathbf{H}}^2$ and $\beta_{\mathbf{G}}^2\beta_{\mathbf{G}-\mathbf{H}}^2$ respectively to produce intensities.

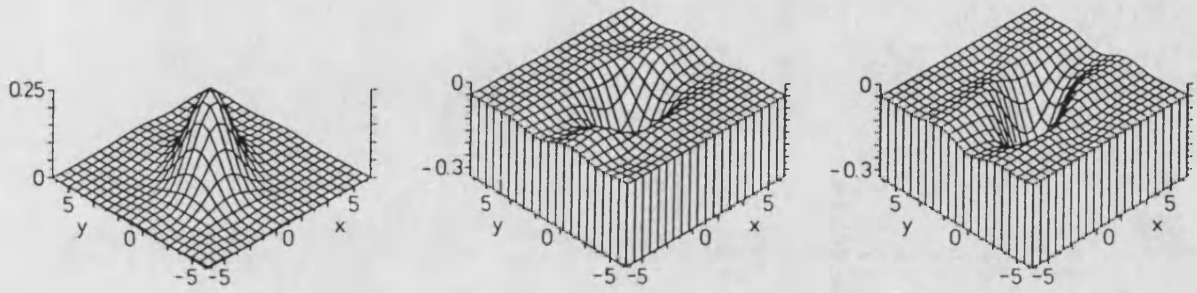

Figure 3.3.3. Generic fourth order intensity anomalies around a three-beam point. Each is independent of the phase triplet θ.

As expected, the fourth order intensities are phase independent, and each produces an intensity "blip", centred around the exact three-beam point which is of different sign for the different terms. Algebraically, the fourth order *ridge* intensity (ignoring the two-beam term) is

$$I_{\mathbf{G}}^{(4)}(x,0) = \beta_{\mathbf{H}}^2\beta_{\mathbf{G}-\mathbf{H}}^2\left[\frac{1-f(2x)+f^2(x)}{4x^2}\right] - \beta_{\mathbf{G}}^2\left(\beta_{\mathbf{H}}^2+\beta_{\mathbf{G}-\mathbf{H}}^2\right)\left[\frac{1-f(2x)}{2x^2}\right], \tag{3.3.5}$$

where again $f(X) \equiv \sin(X)/X$. The terms in braces are plotted in figure 3.3.4. Each is a positive even function with a maximum at $x = 0$ and a similar shape for all x.

The overall effect of the fourth order intensity is therefore to produce a symmetrical blip, centred at the three-beam point whose peak height may be found

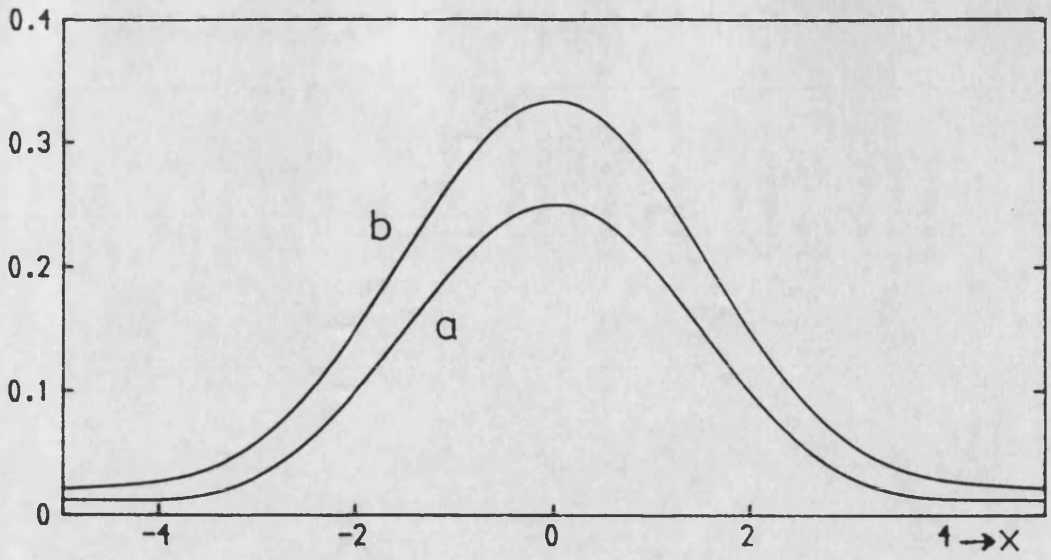

Figure 3.3.4. The generic shape factors for the fourth order ridge intensity (3.3.5). (a) and (b) are the terms in braces in the order they appear in the equation.

by taking the limit $x \to 0$ of (3.3.5):

$$I_{\mathbf{G}}^{(4)}(0,0) = \frac{1}{4}\beta_{\mathbf{H}}^2\beta_{\mathbf{G}-\mathbf{H}}^2 - \frac{1}{3}\beta_{\mathbf{G}}^2\left(\beta_{\mathbf{H}}^2 + \beta_{\mathbf{G}-\mathbf{H}}^2\right). \tag{3.3.6}$$

Since the width of the fourth order terms is comparable with the separation (π) between the third order maximum and minimum, it is to be expected that the positions of these extrema will be shifted. Assuming this fourth order shift to be the dominant source of systematic error due to truncation, then the important parameter is the size of the fourth order blip, (3.3.6). It is then clear that it is the *combination* of the β (3.3.6), and not the individual β themselves which must be kept to manageable proportions. In practice, the Kikuchi-band vector $\mathbf{G} - \mathbf{H}$ tends to be rather short in order for the centre of the diffuse Kikuchi line to be detectable (see §3.4), so $\beta_{\mathbf{G}-\mathbf{H}}$ may well be greater than 1, but this need not cause major difficulties, unless the fifth order terms (which are again phase dependent) or higher also become large.

We now wish to make a numerical analysis of the systematic error incurred in the prescription of §3.2. To achieve this, x_{max} and x_{min} are computed as the maximum and minimum positions in the full numerical three-beam intensity profile along $y = 0$, for various β and true (or input) θ values θ_{in}. From these a phase is determined θ_{out} as would be measured in the ideal experiment. If all three β are known, this procedure will lead to a *correction* to the measured phase triplet, so producing a more accurate answer. If the β are not known, it would be desirable to have some notion of the expected size of error $\Delta\theta$ for experimentally reasonable diffraction strengths. To this end we introduce a mean diffraction strength $\overline{\beta}$. A natural way to define such a mean is suggested by the result (3.3.6); if the fourth order terms dominate the error, then $|I_{\mathbf{G}}^{(4)}(0,0)|$ is the significant parameter. We therefore set all $\beta = \overline{\beta}$ in (3.3.6), giving $I_{\mathbf{G}}^{(4)}(0,0) = -\frac{5}{12}\overline{\beta}^4$. The right hand side of (3.3.6) is then multiplied by $-\frac{12}{5}$ to produce a mean value of β which preserves the magnitude of the (supposedly dominant) fourth order blip:

$$\overline{\beta}^4 = |\frac{4}{5}\beta_{\mathbf{G}}^2\left(\beta_{\mathbf{H}}^2 + \beta_{\mathbf{G}-\mathbf{H}}^2\right) - \frac{3}{5}\beta_{\mathbf{H}}^2\beta_{\mathbf{G}-\mathbf{H}}^2|. \qquad (3.3.7)$$

The following analysis is therefore performed with chosen values of $\overline{\beta}$ and θ_{in} inserted in the many-beam secular equation (3.2.6). The maximum and minimum ridge intensities are found numerically and a θ_{out} value "measured" exactly using the prescription of §3.2. As mentioned in that section, there are basically two methods of determining phase from this prescription, corresponding to different methods of defining a distance scale in the micrograph. The first is to use some feature other than the three-beam anomaly to define distance scales. This yields a different θ_{out} from the two principal extrema as soon as higher order effects are

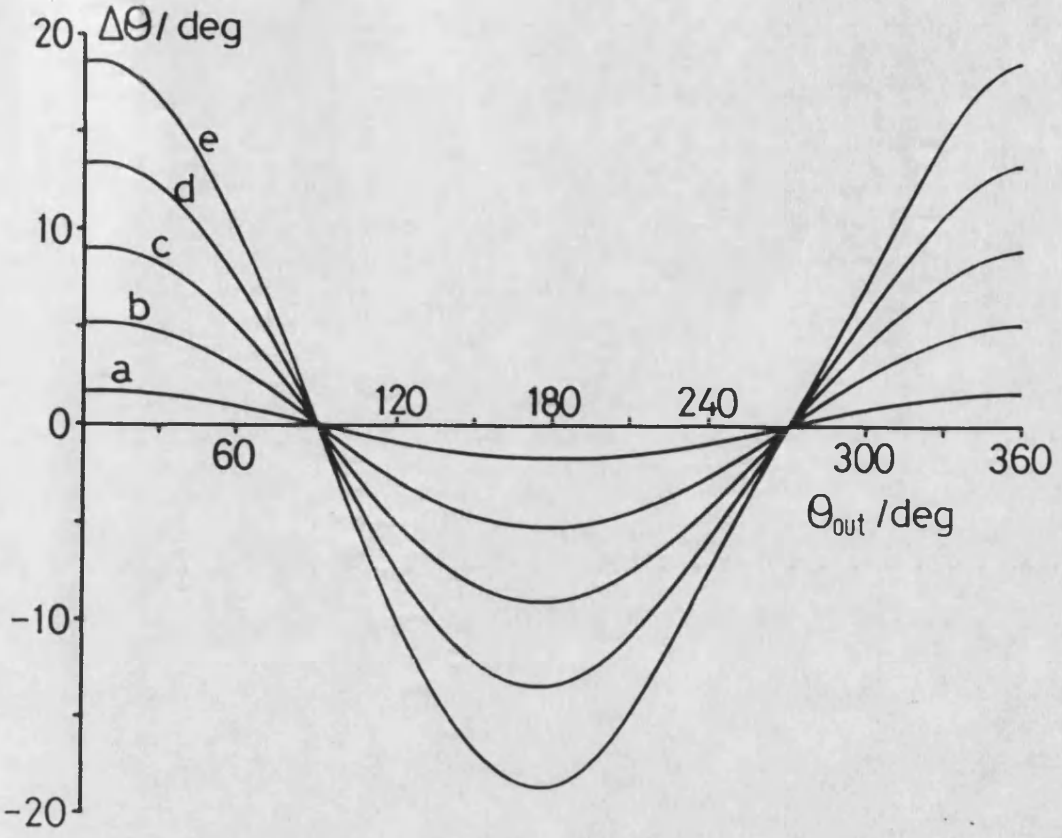

Figure 3.3.5. Error curve derived using three-beam theory to provide ideal "experimental" data. (a) to (e) are for $\overline{\beta}$=0.1, 0.3, 0.5, 0.7 and 0.9 respectively.

detectable. Therefore an error curve of $\Delta\theta = \theta_{in} - \theta_{out}$ against θ_{out} will be two-valued, and in any one quadrant the correct choice of extremum must be made to achieve the optimum accuracy. The advantage of this method is that only one extremum need be detected to produce a θ_{out} value; in practice the stronger extremum will give the more reliable result. The second method to determine θ is to use the definition of distance (3.2.27), and let $\Delta x = |x_{max} - x_{min}|$, whence

$$\theta_{out} = \left(\frac{x_{max}}{\Delta x} + \frac{1}{2}\right)\pi = \left(\frac{x_{min}}{\Delta x} - \frac{1}{2}\right)\pi. \qquad (3.3.8)$$

This prescription gives identical results from both x_{max} and x_{min} irrespective

of higher order effects, so that the deduced error curve is single-valued and particularly easy to use. Figure 3.3.5 shows error curves for $\overline{\beta}$ up to 0.9. Similar curves have been computed with $\beta_{\mathbf{G}}$, $\beta_{\mathbf{H}}$ and $\beta_{\mathbf{G}-\mathbf{H}}$ allowed to be different; the size and sign of the error $\Delta\theta$ is found to be very similar to those for the corresponding mean strength $\overline{\beta}$ defined in (3.3.7), particularly for $\beta \leq 1$. This indicates that fourth order effects are the most important of those ignored, as expected, and justifies the use of the parameter $\overline{\beta}$. If the mean diffraction strength can be kept below unity, figure 3.3.5 shows that the systematic error should not exceed $\pm 15°$ or so. Furthermore, as has been stated, a numerically *corrected* value of θ may be produced if all three β are known, by adding $\Delta\theta$ to experimentally measured values of θ_{out}. Finally, it has also been found that if the more favourable extremum is chosen when using the first prescription the errors from the two methods are almost identical.

3.3.2 Absorption

As discussed in Chapter 2, the effects of absorption are introduced in HEED in terms of an imaginary potential $iU'(\mathbf{r})$. For the most part, a rigorous determination of the form of U' is impossible, so that in practice absorption is treated "phenomenologically" (eg Humphreys 1979), if at all. This puts a limit on the accuracy of quantitative crystallography using electrons. Obviously, a measurement of crystallographic phase is quantitative, so we should have at least some feel for the effects on our prescription of the absorptive potential.

The usual approach to absorption is to assume U' to be small compared with U and to treat it as a perturbation (Hashimoto, Howie and Whelan 1962). Then

in projection the first order change in the energy eigenvalue $s^{(j)}$ of the two-dimensional eigenstate $\tau^{(j)}$ [see (2.3.1) and (2.3.2)] is computed as (eg Schiff 1968)

$$\Delta s^{(j)} = i\langle\tau^{(j)}(\mathbf{R})|U'(\mathbf{R})|\tau^{(j)}(\mathbf{R})\rangle. \tag{3.3.9}$$

The eigenstate itself is also changed to first order (though this is usually ignored) as

$$\Delta\tau^{(k)} = i\sum_{j\neq k}\frac{\langle\tau^{(j)}|U'|\tau^{(k)}\rangle}{s^{(k)}-s^{(j)}}\tau^{(j)}. \tag{3.3.10}$$

These equations can of course be transformed into reciprocal space if this is more convenient for calculation, by expanding the $\tau^{(j)}$ as the Bloch sum (2.3.3), for example.

Although the corrections Δs and $\Delta\tau$ contain within in them the effect of U' on the structure factor phases ϕ, it is more illuminating in this case to study the effect rather more directly. As a first step, it is instructive to make the common assumption in HEED (eg Humphreys and Hirsch 1968) that $U' = 0.1U$. Then each structure factor can be written

$$U_{\mathbf{G}} \rightarrow U_{\mathbf{G}} + iU'_{\mathbf{G}} = U_{\mathbf{G}}(1 + i0.1) \approx U_{\mathbf{G}}\exp(i0.1). \tag{3.3.11}$$

That is, the effect of the absorptive potential is to introduce a phase shift of about 6° to each structure factor, and hence to the phase triplet θ, since two of the ϕ in the triplet are positive, and one negative.

There is, unfortunately, no reason why the absorptive part of the potential should be proportional to the elastic part. Thus the argument of the above paragraph is of no quantitative use at all. In general, U and U' will not be

proportional, nor even in phase, in noncentrosymmetric crystals. This has been demonstrated nicely by Bird and King (1990) for the case of thermal diffuse scattering (TDS) using the Einstein independent atom approximation. The values obtained for θ using our method must be those of the full electron structure factors including U' since ours is a measurement technique, leading to *inversion* of the problem. Were we to use the imaginary potentials as parameters in a fitting procedure, it should be possible to determine the phase triplet due to the elastic part of the potential only. This should be borne in mind since it is the elastic potential which is more readily related to the crystal parameters of interest via (3.1.2), and U' only obscures this relation in the general case where the two components are not in proportion or phase.

Let us define a total structure factor for a particular Bragg reflection as

$$U^{tot} = U\exp(i\phi) + iU'\exp(i\phi') \tag{3.3.12}$$

and perform a rather better analysis of the first order modulus and phase changes in U due to U'. This may be done by writing

$$U^{tot} = U\exp(i\phi)\left\{1 + \frac{U'}{U}\exp i\left(\frac{\pi}{2} + \phi' - \phi\right)\right\}, \tag{3.3.13}$$

then expanding the second of the exponentials, truncating the series and re-exponentiating to yield, correct to order U'/U, (Bird 1990)

$$U^{tot} \approx U\exp(i\phi)\left[1 + \frac{U'}{U}\sin(\phi - \phi')\right]\left[\exp\left\{\frac{iU'}{U}\cos(\phi - \phi')\right\}\right]. \tag{3.3.14}$$

In this equation the term outside brackets is the elastic structure factor, which is modulated by the two terms in brackets; the first an amplitude change, and

the second a phase change. In centrosymmetric crystals the real and imaginary parts of the potential are either in phase or anti-phase, for the same reasons that $\phi = 0$ or π (see §3.1.2). Hence $\phi - \phi' = 0$ or π, and there is no first order structure amplitude change, and only a phase change of U'/U radians, or $\sim 6°$ for $U'/U = 0.1$. This is just a restatement of the result of (3.3.11). For the general noncentrosymmetric case, however, there is a first order change to both the phase and amplitude of a structure factor due to the absorptive contributions. This is the effect that Zuo Spence and Høier (1989) overlooked in trying to make precise measurements of phase triplets in CdS, by a fitting method (see Bird, James and King 1989). Only the modulus of U' is allowed to vary, so that their fitted phase triplet (claimed to be accurate to 0.9°) would *not* give as good a fit on the set of vectors described by $\mathbf{g} \rightarrow -\mathbf{g}$, as they claim it should. The authors miss this difference because they consider only the first order eigenvalue change Δs, and ignore the eigenstate change $\Delta\tau$. Note that in practice, the Doyle and Turner (1968) elastic form factors predict structure factor phases which are altered by up to 20° in some noncentrosymmetric crystals by the inclusion of the TDS form factors of Bird and King (1990).

Diffuse scattering

As will be seen in the next section, one of the major difficulties encountered in the actual measurement of phase invariants by the method presented here is in locating the position of the exact three-beam point $x = 0$. As the method stands, this must be achieved by finding the position of the Kikuchi line profile associated with $\mathbf{G} - \mathbf{H}$ at which it crosses the three-beam point $x = 0$. As an on-axis, zero-layer feature, this band is of the symmetrical variety discussed in

§2.4, and therefore has a profile [see figure 2.4.2] not dissimilar to some of the three-beam intensity anomalies. The first problem is therefore that the Kikuchi band profile should be subtracted (incoherently) from the measured anomaly. This may be achieved by scanning a line parallel and close to the excess line of interest, and assuming that the variation of the diffuse background between the two positions is small. Unfortunately, of course, this process assumes the film to have a linear response to intensity.

It is found in practice (see §3.4) that a weak extremum in the three-beam anomaly may well become smeared by this subtraction, but that a strong extremum stays essentially where it is. The real problem comes in deciding where in the Kikuchi line profile one should draw the "centre", giving the position $x = 0$, since the feature may be too weak to detect any appreciable profile at all. Even if it is detectable, there is usually no obvious and general prescription for deciding which part of the profile corresponds to the exact two-beam Bragg condition, as required. For this reason, the difficulty is minimised by choosing rather short vectors $\mathbf{G} - \mathbf{H}$, with values of $\beta_{\mathbf{G}-\mathbf{H}}$ somewhat larger than ideal. If this were not necessary, the method would be much more satisfactory since the effect of higher order terms would be much less noticeable. It is therefore suggested that a study be made of the possible ways to use an *elastic* feature to define the position of the exact three-beam point, since this would improve the method on two counts; larger $\mathbf{G} - \mathbf{H}$ vectors could be used, and $x = 0$ could be found more accurately. Of course, the reason we chose $\mathbf{G} - \mathbf{H}$ to be a Kikuchi band was so that only one three-beam anomaly, and not two, is observed. If the price to pay for the improvement of the method is that two anomalies must

be investigated at once, it is no longer obvious that the intensity profile can be inverted in terms of just one parameter! As an aside, preliminary calculations (Wright 1989) indicate that the asymmetric Kikuchi lines underlying all the Vincent pattern excess lines will have little or no effect on the prescription.

It should be said that these discussions do not constitute a quantitative analysis of absorption. No account is taken of the effects caused by plasmons or core excitations, and it is difficult to see how to do so. Even the TDS form factors used to determine the phase and amplitude changes to the elastic structure factors are themselves are based on the perturbation integrals of Hall and Hirsch (1965), and as such are still only an approximation to the true situation. However, as mentioned before, it is hoped that the results of an analysis based on TDS calculations will at least have given an indication of the overall effects of inelastic scattering.

3.4 MEASUREMENT OF PHASE TRIPLETS IN InP

It is not the intention in this thesis to use a derived prescription for phase measurement as tool in the determination of an unknown crystal structure; such work is about to be pursued elsewhere (Exelby and Vincent 1989). Instead, the aim is to show that a simple prescription *can* be derived, and that (in principle) it may be applied for such a purpose. To this end, this section gives a "worked example" of how the prescription works (or does not work) in practice, with the intent of highlighting some of the subtleties involved. It should be stressed, however, that this is not a rigorously developed experimental analysis, but simply a preliminary study. It is believed that with some care the reliability

of the results given here could be significantly improved upon.

The material chosen for study is InP. The III-V semiconductors tend to be relatively easy to prepare for transmission microscopy, and all have the simple zincblende structure at room temperature, which may be described as a face-centred cubic lattice with a two-point basis at $(0,0,0)$ and $(\frac{1}{4},\frac{1}{4},\frac{1}{4})$. By choice it is assumed that In is at $(0,0,0)$, and P at $(\frac{1}{4},\frac{1}{4},\frac{1}{4})$. The particular attraction of InP is that it is the "least centrosymmetric" of the common III-V materials, in that it exhibits phase triplets furthest from 0 or π. This is basically because of the large difference between the atomic numbers, and hence the scattering strength, of the two atomic species involved.

Figure 3.4.1 is a long camera length portion of a 200kV Vincent pattern taken from close to the $[6\bar{5}3]$ axis of InP, at room temperature.
Essentially this pattern is a magnification of part of the Vincent pattern in figure 3.2.1. This magnification is useful, since the prescription requires a scan to be made along the excess line $y = 0$; in practice this scan must be of finite width, so it is desirable that a given width corresponds to small deviations in the y-direction.

The particular anomaly to be studied is where the $\mathbf{G} = (77\bar{3})$ excess line crosses the $\mathbf{G} - \mathbf{H} = (20\bar{4})$ Kikuchi band. The anomaly directly across the band from this one is due to the crossing of the $\mathbf{H} = (571)$ excess line. Note that already we have assumed a certain polarity of the crystal in naming the pole as $[6\bar{5}3]$ and not $[\bar{6}5\bar{3}]$, etc. It will become obvious whether this choice is correct once θ is measured, since the two polarities give quite different values in this case.

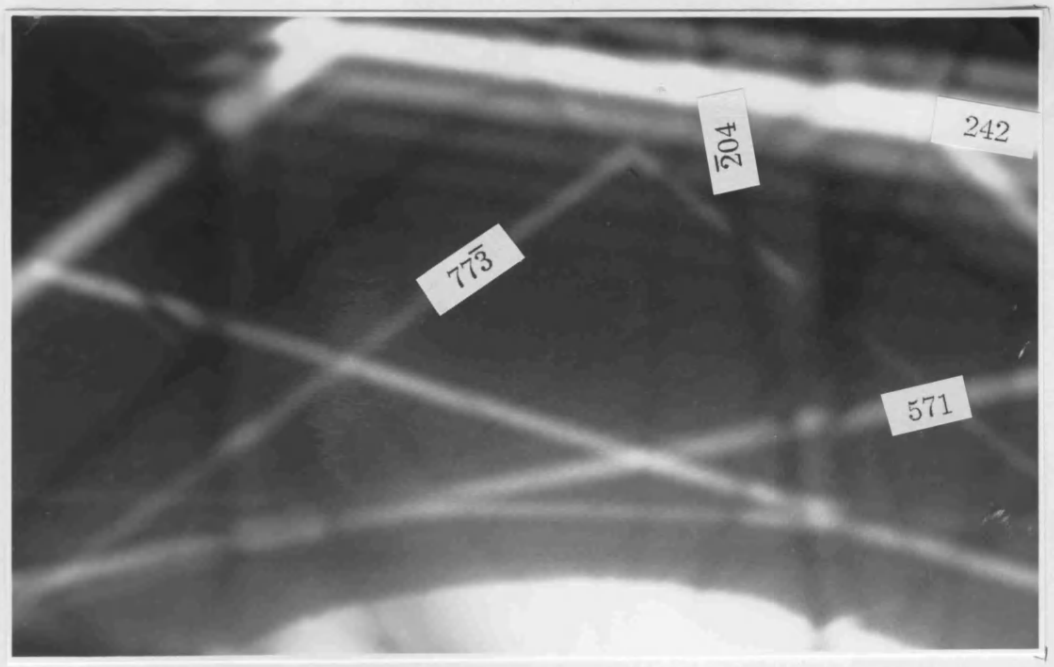

Figure 3.4.1. Long camera length micrograph showing a portion of a 200kV InP $[6\bar{5}3]$ Vincent pattern. The region chosen for analysis is where the $(77\bar{3})$ excess line crosses the $(20\bar{4})$ Kikuchi line. This region corresponds to position C in figure 3.2.2. B is directly across the Kikuchi band, where the (571) excess line crosses. [Picture courtesy A G Wright.]

This difference is essentially the one exploited by Ishizuka and Taftø (1984) in proposing a method to determine the polarity of zincblende crystals. Note also that in the notation used here, $\mathbf{u} = [6\bar{5}3]$ is parallel to the surface normal, and not anti-parallel. Thus $\mathbf{G}.\mathbf{u} = -2$ for the HOLZ reflections studies.

To predict the value of θ which should be measured, the Doyle and Turner (1968) and Bird and King (1990) form factors have been used, for the elastic and absorptive parts respectively. Table 3.4.1 shows the elastic (Doyle-Turner) structure factors at an accelerating voltage of 200kV, in the chosen polarity. The form factors include a Debye-Waller correction $\exp(-M_\kappa g^2)$, taken from the calculations of Reid (1983). Note that both the Doyle-Turner and the Reid data use $s = g/4\pi$, and not g, as the amplitude of the scattering wavevector, so that,

for example, a Reid Debye-Waller figure is B in the exponential $\exp(-Bs^2)$. M is given by $M = B/16\pi^2$. At 300K in InP, Reid gives $B_{In} = 0.897, B_P = 0.587$.

g	$U_{\mathbf{g}}^R$	$U_{\mathbf{g}}^I$	$\lvert U_{\mathbf{g}}\rvert$	$\phi_{\mathbf{g}}$
$77\bar{3}$	−0.167	−0.076	0.183	204.5
571	−0.273	0.113	0.295	157.5
$20\bar{4}$	−0.566	0.000	0.566	180.0

Table 3.4.1. Calculated elastic structure factors in InP. Units are Å^{-2} and degrees. See text for sources and details.

The point to notice about the potentials in table 3.4.1 is that, since the interaction between a fast electron and a crystal is basically attractive, the $\phi_{\mathbf{g}}$ tend to be centred about 180° and not 0°. The elastic structure factors of table 3.4.1 predict a value of phase triplet measured at the $\mathbf{G} = (77\bar{3})$ anomaly of

$$\theta_{el} = \phi_{571} - \phi_{77\bar{3}} + \phi_{20\bar{4}} = 133.0°. \qquad (3.4.1)$$

Table 3.4.2 shows the same structure factors, with the inclusion of the absorptive form factors of Bird and King (1990).

g	$U_{\mathbf{g}}^R$	$U_{\mathbf{g}}^I$	$\lvert U_{\mathbf{g}}\rvert$	$\phi_{\mathbf{g}}$
$77\overline{3}$	−0.163	−0.104	0.193	212.5
571	−0.278	0.073	0.287	165.3
$20\overline{4}$	−0.566	−0.073	0.571	187.3

Table 3.4.2. InP structure factors including absorptive form factors. Units are Å^{-2} and degrees. See text for sources and details.

The phase triplet predicted by these data is

$$\theta_{ab} = 140.1°. \tag{3.4.2}$$

Note that each phase, and therefore the phase triplet, is shifted from its elastic value by some $7-8°$. In this case the TDS form factors suggest a correction very similar to the 6° correction for $U = 10U'$! θ_{ab} will serve as our best prediction of the phase triplet under investigation, since this is a measurement, and not a fitting, technique.

Before going on to make a measurement of the phase triplet θ_{ab}, it is first useful to determine the specimen thickness t, to give an indication of the magnitude of the diffraction strengths β in this case. t may be measured from the fringes of the excess line in the bottom right-hand corner of figure 3.4.1 (see eg Kelly *et al.* 1975). This line may be indexed using the same kinematic simulation shown in §3.1, and is found to be (242). Now, from §2.4, the two-beam deviation parameter in the direction perpendicular to this excess line is $W_{242} = G_{242}\delta K$, and well away from $\delta K = 0$ the two-beam intensity (2.4.1) is given by

$$I_{\mathbf{G}_{242}} \propto \sin^2\left(\frac{W_{242}t}{2k}\right). \tag{3.4.3}$$

The separation ΔK of two adjacent minima well away from the excess line is therefore equivalent to a change in the argument of this expression of π, so the thickness t is given by

$$t = \frac{2\pi k}{G_{242}^2} \cdot \left(\frac{G_{242}}{\Delta K} \right). \tag{3.4.4}$$

G^2 may be calculated for this known structure, and $k = 250\text{Å}^{-1}$ at 200kV [see (2.2.7)]. Thus only the ratio of the tramline separation to the fringe separation need be measured for a determination of t. In this case it is found that $t \approx 1040$Å. It should be noted that since Vincent patterns are taken from a rather large area of a specimen, the thickness may well vary over the pattern. Thus the actual thickness associated with the three-beam point of interest may be different to that measured at some other region. Clearly the best fringes to use would be those either side of a line originating from close to the three-beam point; either the **G** or the **H** line would therefore be perfect. Unfortunately, such fringes are almost undetectable in the negatives used in this preliminary study. The other point to note is that the fringe determination of thickness relies on a defined distance in terms of deviation parameters, almost identical in form to the parameters x and y. Thus it proves possible to define a distance scale only by comparison of two such deviations, thus circumventing the need for a direct measurement of t, though not necessarily avoiding the problem of t variation.

The diffraction strengths associated with the structure factors of table 3.4.2 are (assuming $t = 1040$Å)

$$\beta_{77\bar{3}} = 0.401 \qquad \beta_{571} = 0.579 \qquad \beta_{20\bar{4}} = 1.188 \tag{3.4.5}$$

[see 3.2.5)]. Although the last of these is larger than ideal, the mean diffraction

strength, defined via (3.3.5), is $\overline{\beta} = 0.49$.

Figure 3.4.2a is a positive intensity scan taken along the centre of the $(77\overline{3})$ excess line, using a digital microdensitometer. This work was performed courtesy of Bristol University, and with the help of I K Jordan. The scan is approximately 100μm wide, and is taken from the outside to the inside of the Kikuchi band $(20\overline{4})$; from the definition (3.2.4) the scan is seen to be in the $+x$-direction, along the line $y = 0$. All the scans taken are rather noisy, since the negative used was darker than optimum for the microdensitometer.

Figure 3.4.2b is a scan taken inside and parallel to figure 3.4.2a, and shows the Kikuchi band profile close to the excess line. It is assumed that this is very similar to the Kikuchi profile underlying the excess line itself; care has therefore been taken to ensure that the centre of both scans is at the same distance from the Kikuchi band, so that the two may be subtracted to give a scan corrected for diffuse scattering. This corrected scan is shown in figure 3.4.2c.

Note that in figure 3.4.2c there is a large maximum toward the inside of the band, and a weaker minimum outside. Now, the Kikuchi band $\mathbf{G} - \mathbf{H}$ has indices $h + k + l = 4n + 2$ (n is an integer). The two crystal polarities in this case correspond to $\mathbf{G} = 4n + 1, \mathbf{H} = 4n - 1$ and $\mathbf{G} = 4n - 1, \mathbf{H} = 4n + 1$. The latter has been adopted so far. If only elastic form factors are used, it is easily shown that in the opposite polarity, $\theta_{el} = 227°$ rather than 133°. As mentioned before, electron structure factor phases are centred about 180°, so the two polarities are in fact $\theta_{el} = 180° \pm 47°$. With the inclusion of absorptive form factors, this exact symmetry between polarities is lost. However, reference

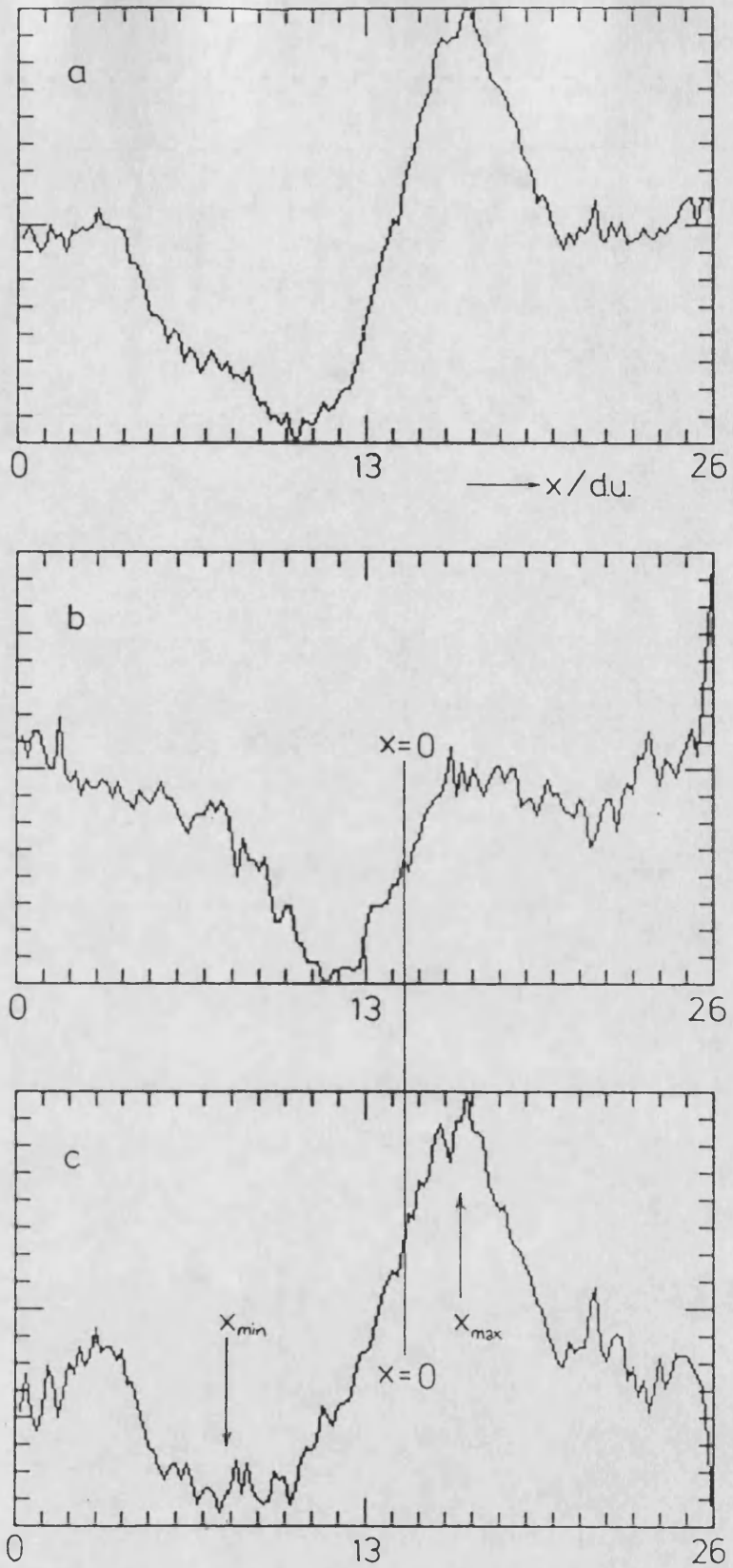

Figure 3.4.2. Digital microdensitometer line scans of the region close to the three-beam anomaly being studied. (a) is the raw data, scanned along the $(77\bar{3})$ excess line. (b) is the $(20\bar{4})$ Kikuchi line profile parallel and close to (a), and (c) is (a)-(b). The vertical scales in these plots are inconsistent.

to figure 3.2.6 shows that the measured anomaly is much more like that for $\theta = 150°$ than for $\theta = 210°$. Since absorption is unlikely to cause a large shift in the triplet, it is concluded that the polarity of the specimen is as given.

From now on it is possible to work in the "densitometer units" (d.u.) along the x-direction, as indicated on each of the plots in figure 3.4.2. The first task is to define the distance Δx in d.u. which is equivalent to π in the naturalised units of the prescription. Assuming the maximum and minimum to be in the positions indicated in figure 3.4.2c, this gives from (3.2.27)

$$\Delta x = |16.6 - 7.9| = 8.7 \text{ d.u.} \tag{3.4.6}$$

The final piece of information required is the position $x = 0$ of the exact three-beam point. As already mentioned, this is situated in the "centre" of the underlying Kikuchi line. For a line such as $(20\bar{4})$ with h+k+l even, symmetric Kikuchi bands in the zincblende structure have their maximum gradient at $x = 0$ (Bird and Wright 1989). $x = 0$ is also the approximate position halfway between the maximum and minimum values in the Kikuchi profile intensity. As figure 3.4.2b shows, the selection of such a position in a noisy scan cannot be achieved with any certainty, even for this rather strong band. The figure shows one possible position of the origin, at $x = 14.4$d.u. From the prescription (3.2.28) this gives a measured value of the relevant phase triplet as

$$\theta_{ab} \approx \left(\frac{2.2}{8.7} + \frac{1}{2}\right)\pi = 2.37^c = 136°. \tag{3.4.7}$$

Measured from 180°, $\theta_{ab} \approx -44°$. This apparently accurate agreement of the measured and predicted phase triplet (3.4.2) may well just be a coincidence. Of

course, even the prediction itself is an approximation. From figure 3.3.5, the expected systematic error for $\overline{\beta} \approx 0.5$ at $\theta_{out} = 136°$ is $\sim -7°$, giving $\theta_{in} \approx 129°$. As an indiction of the measurement error to expect, note that a shift of the origin $x = 0$ of 0.1d.u. in (3.4.7), keeping all else constant, changes θ_{out} by some 2.5°; a shift of the value of Δx is less drastic, but still has an effect.

Conclusions

The conclusion to be gained from this example is that, even with a set of noisy scans from a dark negative, the prescription of §3.2 gives a measurement of a phase triplet which is probably within $10-15°$ of the true answer. This is a very similar result to that found by Bird, James and Preston (1987) on a different sample, using an analogue microdensitometer. It is expected that with more analysis these errors could be reduced (or at least quoted with more certainty), and that if a better method could be found of pinpointing $x = 0$ (especially in terms of elastic features), this would certainly be so. Finally, it should be said that any determination of phase triplets, however accurate, must be of use in the direct methods of crystallography, where even a knowledge of the *sign* of some of the structure factors would be of benefit. At the very least this technique should provide a quick means of finding approximate phase triplets, especially in the trivial centrosymmetric crystal case.

Chapter 4

RESONANCE EFFECTS IN RHEED

4.1 INTRODUCTION

The aim of this chapter is to provide a satisfactory explanation of the position and nature of features in convergent-beam RHEED patterns associated with so-called "surface resonance". Figure 4.1.1 shows examples of such CB-RHEED patterns taken from the [231] axis of a Platinum $(\bar{1}1\bar{1})$ surface, and the [116] axis of a $(\bar{1}10)$ Gallium Arsenide surface, both at an accelerating voltage of 200kV. The features of particular interest in these patterns are marked in the figure. The parabolic curves, frequently referred to as "resonance parabolas", are associated with electrons travelling parallel to the specimen surface. These are the features of primary concern in this chapter; the straight-line envelopes surrounding these parabolas will also be studied, as will those regions where a parabola crosses an excess diffraction line running parallel to the shadow edge of the specimen. Such lines will be referred to as "surface-parallel Bragg lines". These features have all been studied before at some length (see later), but under widely varying experimental conditions, most notably microscope voltage. Unfortunately, there has been a tendency to transport the language used to describe electron diffraction at crystal surfaces rather freely between different energy régimes. Thus work performed at microscope voltages (typically 100-200keV) has been described in terms of the "resonant" behaviour supposedly observed at conventional RHEED camera energies (10-20keV) and LEED ener-

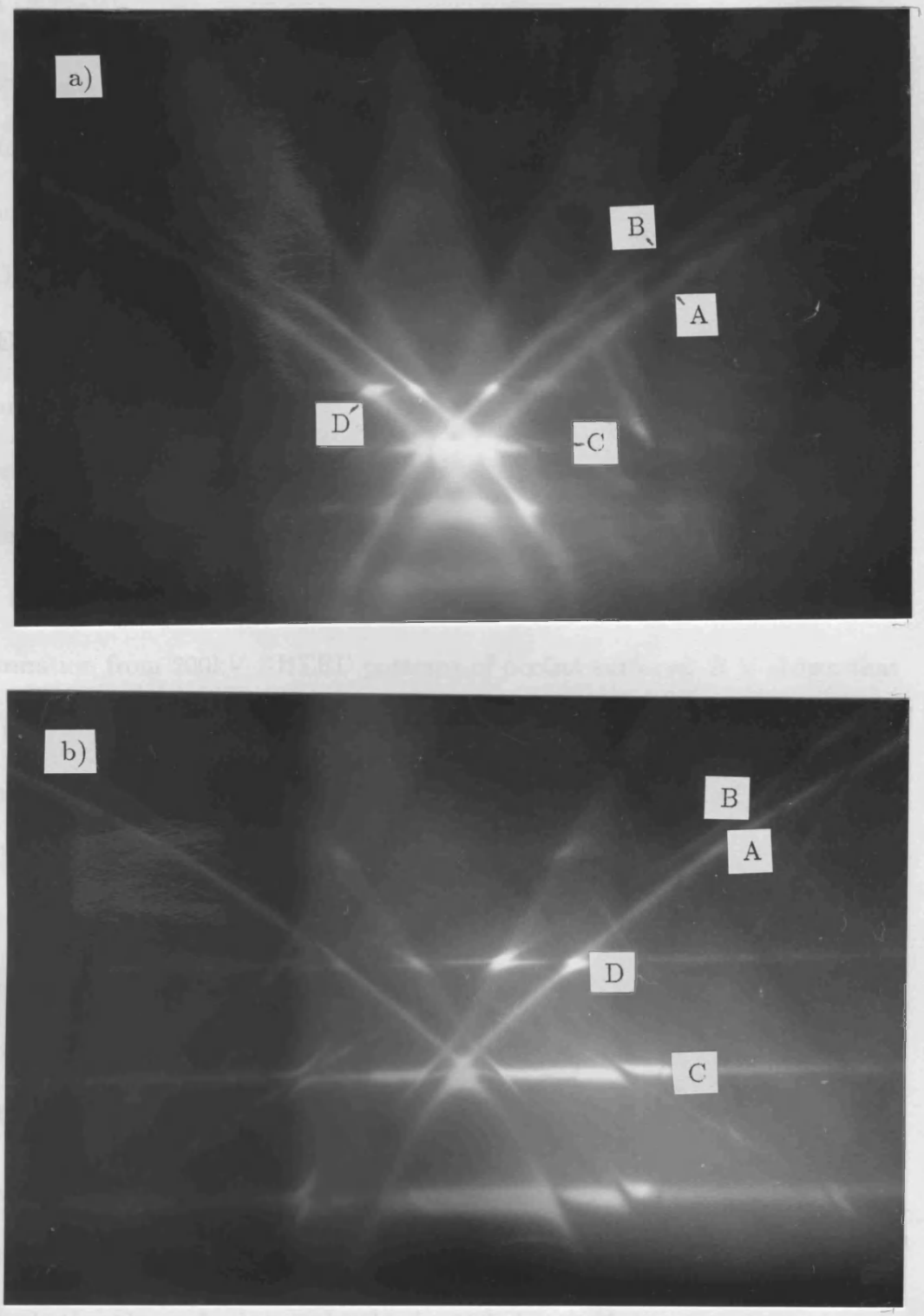

Figure 4.1.1. 200kV CB-RHEED patterns (courtesy A G Wright). (a) is from close to the [231] axis of a Pt$(\bar{1}1\bar{1})$ surface. (b) is from close to GaAs[116], from a $(\bar{1}10)$ surface. The parabolas (marked A), their envelopes (B), the surface-parallel Bragg lines (C), and the bright regions (D) are all studied.

gies (0-1keV).

Associated with this transfer of language is the assumption that if a feature is surface sensitive in LEED, say, in that only a few outermost atomic layers contribute, then the same is likely to be true of a geometrically similar feature in a RHEED pattern at any energy. As will shortly be explained more fully, both LEED and conventional "low-voltage" RHEED can be used to obtain useful information from surfaces, but either phenomenologically or by means of laborious fitting procedures. It will be argued that "high-voltage" RHEED at microscope voltages should be easier to analyse, and is therefore potentially more useful. We therefore present an investigation of the possibilities of retrieving surface information from 200kV RHEED patterns of perfect surfaces. It is shown that (at this voltage), the incident electrons penetrate far enough into the specimen for most, if not all, of the resulting diffraction features to be more characteristic of the bulk than of the surface. This means that surface and bulk information will be mixed in these patterns, which will tend to negate the analytical advantages. It should be stressed at this point that the term "surface" may or may not include a few selvedge layers beneath the outermost layer of atoms, depending on the application.

The analysis is based upon a perturbation expansion of the Kambe equations (2.3.18) which is particularly appropriate at high energies. In this application perturbation theory leads to a simple physical picture of the scattering processes responsible for the features in figure 4.1.1, which is masked in the "black-box" numerical techniques required for LEED and low-voltage RHEED. This chapter therefore contains what is believed to be the first full explanation of the ZOLZ

RHEED pattern geometry, including the parabolas, their envelopes, and their intersections with surface-parallel Bragg lines. Also, this approach facilitates a discussion of the term "resonance", which been used in many papers (for references see later) to describe features in RHEED patterns at all energies, without explanation. Judgement is left until considerably later in the chapter as to which of the diffraction features mentioned, if any, are "resonant", and which may be surface sensitive under the right experimental conditions, and therefore of potential use in quantitative surface crystallography. However, for the sake of consistency with other authors, the term "surface resonance" will for the present be employed.

4.1.1 General features of RHEED analysis

Clearly, the attraction of performing RHEED experiments lies in the possibility of extracting information about a crystal surface. One of the major uses of low-voltage RHEED is in the in-situ monotoring of crystal growth by molecular beam epitaxy (MBE), where oscillations of RHEED intensities have a period that nearly always corresponds to the growth of a single atomic or molecular layer (see eg Joyce *et al.* 1988). RHEED is particularly suited to this application since its glancing-incidence, small-angle scattering geometry is complementary to the surface-normal geometry of the MBE equipment. This is clearly a case where surface information (from an *imperfect* surface) is deduced directly and simply from a RHEED pattern. However, this application is based upon an *empirically* established relationship between diffracted intensities and layer growth, and not on an *ab initio* study of RHEED.

Other successes in low-voltage RHEED nearly all derive from fitting experiment to numerical simulation. As an early example, Maksym and Beeby (1981) have related surface-layer spacings to absolute intensities in RHEED rocking curves. Other examples include the observation at 12.5kV that RHEED intensities are different for various reconstructions of a GaAs(001) surface (Larsen *et al.* 1986). More recently, Horio and Ichimiya (1989) have made kinematic fits of RHEED rocking curves to those observed from the reconstructed Si(111)7 × 7 surface. Unfortunately it is difficult to find very many successful and simple applications of RHEED, so that interest in the subject has tended to wax and wane over the last 50 or 60 years.

One of the reasons for the conspicuous lack of success using RHEED by comparison with THEED is that the latter is much easier to analyse. This is partly due to the differences in the starting equations, as highlighted in §2.3; RHEED presents a genuine *scattering* problem, governed by a set of coupled second-order differential equations. The THEED problem can be reduced to first-order equations, such as those of Howie and Whelan (1961, and see §2.3), and is therefore much easier to tackle, both analytically and numerically. Furthermore, the presence of the surface in one of the directions perpendicular to the incident beam (see figure 2.2.1) interrupts the periodicity of the scattering potential in that direction. Thus a 2-dimensional projected potential cannot be considered periodic, so even the description of *elastic* scattering in RHEED is rather complicated. In addition, the *inelastic* contributions to the scattering potential will be important, since they govern the absorption length, or penetration depth, of an electron in any given state. It therefore follows that if the absorptive poten-

tials are not well known, it will in general be far from easy to identify whether the features observed in a RHEED pattern have come from the surface, from the bulk material beneath the surface, or from a mixture of the two. As will be discussed later, it is indeed difficult to determine the components of the absorptive potential which control penetration, so quantitative figures for the number of atomic layers over which a "surface" wave is spread are not easily found.

An additional factor which prevents the easy analysis of low-voltage RHEED is that the Ewald sphere is too small for the projection approximation to be used with anything like the same confidence as for typical microscope voltages (200kV, say). As a consequence, a realistic calculation of RHEED intensities at these energies must incorporate the effect of many HOLZ reflections (see eg Zhao and Tong 1988). The diffraction equations must remain 3-dimensional, and far too many beams must be included for anything other than a numerical simulation to be useful. The same problem exists in LEED theory, which is almost exclusively numerical. In principle, then, RHEED at microscope voltages should be easier to analyse since, to a good approximation, it is a two-dimensional problem and, as we shall see, more amenable to treatment by perturbation theory.

Many of the early attempts at producing a numerical dynamical theory of RHEED were based on a second-order version of the transmission multislice method (see eg Cowley 1981), in which the governing differential equations are solved by integration across thin slices of the specimen. The programs of Maksym and Beeby (1981), Ichimiya (1983) and others take these slices parallel to the crystal surface, while Peng and Cowley (1986) slice in the perpendicular direction, in an attempt to model surface steps. In this latter case it is neces-

sary to construct a supercell consisting of the specimen and the vacuum outside it. Programs based on a multislice method and applied to RHEED would all appear to have problems with numerical instabilities. In an attempt to improve matters, more complicated numerical algorithms have been conceived and implemented (eg Zhao, Poon and Tong 1988), but these do nothing to improve the possibility of inversion or to aid an understanding of the basic physical processes responsible for phenomena such as resonance; if anything these methods are even more "black-box" than earlier ones. Some progress would appear to have been made with Bloch-wave calculations (see eg Bleloch 1989 and references therein), though they have yet to produce much more insight into the causes of the principal RHEED features than have other techniques. In addition, it is almost universal practice to produce only 1-dimensional scans or "rocking curves" of the diffracted intensities. This makes it rather difficult to establish whether the important features are well simulated or not, since in the cases we are considering they tend to be extended over the whole 2-dimensional pattern. Also, it is found that not all the diffracted lines can be described in terms of simple Bragg diffraction, so the indexing of the features will not be easy unless an overall simulation is available.

It is, of course, a logical step to make use of electron microscopes in the investigation of RHEED, and many have done so (see eg Ichimiya, Kambe and Lehmpfuhl 1980, Wang *et al.* 1989, Bleloch 1989). In addition to the analytical advantages of using the projection approximation, the facility to rock the beam, or to take convergent-beam patterns, may provide 2-dimensional intensity scans. However, it is to be expected that the penetration of the incident electrons will

increase with energy, so there must be some trade-off between experimental and analytical elegance and surface sensitivity. A brief and far-from-rigorous investigation of this trade-off will be given later in the chapter.

4.1.2 RHEED and surface resonance

The first report of enhanced intensity at certain orientations in RHEED patterns was made as long ago as 1933 by Kikuchi and Nagakawa. These effects were shown by Miyake, Kohra and Tagaki (1954) to be associated with the excitation of a diffracted wave parallel or nearly parallel to the crystal surface. "Resonance" in such a picture is due to the surface-parallel waves having a long path-length, leading to strong, dynamical diffraction, and hence to an intensity enhancement. The most appealing description of how a surface-parallel wave leads to a parabolic diffraction feature is given by Ichimiya, Kambe and Lehmpfuhl (1980), and is the description used in §4.1.3. As will be shown there, the basic geometrical argument is a kinematic, zero-potential one, corresponding to a description of all electron states as plane waves. The parabolic equation produced by such an argument was extended by Bird (1987) to include Bloch-wave effects, in response to the work of Marten and Meyer-Ehmsen (1985), who showed that the parabolas are associated with the coupling of the diffracted wave-field into the bound states of a 1-dimensional potential of the crystal. (This is the "rod" potential of §2.3.3. The single dimension is in the surface-normal direction x.)

Unfortunately, most of the attempts to explain in detail the nature of these parabolic features, their envelopes and intersections have been contradictory and sometimes misleading. Although some authors have correctly identified

the cause of parts of the geometrical make-up of patterns such as figure 4.1.1, (eg Marten and Meyer-Ehmsen 1985, Lehmpfuhl and Dowell 1986, Wang, Lu and Cowley 1987, Yao and Cowley 1989) it is suggested here that a complete description has never been given. For example, Marten and Meyer-Ehmsen (1985) interpret the parabola envelopes as simple Kikuchi lines, which is found not to be the case, and also make the false assumption that since a monolayer is sufficient to produce a parabola, the parabolas seen in experiment are therefore produced by a monolayer. In fact, of course, "surface parallel" and "surface localised" will be completely synonymous only if the incident electrons penetrate no further than the topmost layer; this is shown later to be much less likely at microscope voltages than at the RHEED camera voltages used by Marten and Meyer-Ehmsen. For their part, Yao and Cowley (1989) confuse the discussion of RHEED diffraction by describing it in terms of the channelling of electrons in different mean inner potentials, rather than the more elegant and obvious description in terms of the variations of electron dispersion as seen in the relevant branch structure.

It should be noted in passing that one of the features already of use in RHEED patterns are those regions, marked "D" in figure 4.1.1, where the parabola crosses one of the surface-parallel Bragg lines. These regions seem to have an enhanced intensity, which is investigated later in the chapter. The practical use of these enhancements, as pointed out by Uchida, Lehmpfuhl and Jaeger (1984) is that an image formed from such an orientation will have increased intensity and contrast. It has now become common practice for surface images to be taken from such orientations, and reflection electron microscopy (REM) is developing

into a useful means of imaging features such as surface steps (see eg Larsen and Dobson 1988 and references therein). The appearance of surface-step contrast in high-voltage REM clearly shows that surface information *is* present, but not whether it is mixed with bulk information. It does not automatically follow that extractable surface information will be present in high-voltage RHEED patterns from the same surface.

The failure to produce a complete description of the RHEED geometry is not surprising, because of the exclusive use of numerical techniques. The aim of this chapter is to show that the features of high-voltage CB-RHEED patterns such as figure 4.1.1 *can* be explained in physical terms if the investigation is begun using perturbation theory to point the way. As expected, this means we must choose particular conditions which aid our approximations. The specimens are assumed perfectly flat and infinite in the surface-parallel directions. Unlike many authors, we also choose to investigate crystals with a large atomic number (and hence a strong surface-normal or "rod" potential), since it is found that these most clearly divide the diffraction into its basic constituent parts. Platinum is used for this purpose; in addition, patterns from a "medium strength" scatterer, Gallium Arsenide, are used since they tend to be somewhat sharper. [A risk taken by working at higher energies is that the incident electrons will cause beam-damage to the specimen surface. However, the analysis of Bradley and Zaluzec (1987) of the beam-damage thresholds for elemental specimens suggests that for both Pt and GaAs an accelerating voltage of more than 300kV is needed to sputter off the surface atoms. It is therefore hoped that 200kV electrons will cause minimal damage, if any, to the surface.]

Finally, and most importantly, we choose to explain the geometry of RHEED patterns by analogy with almost identical features observed in off-axis transmission patterns (Lehmpfuhl and Dowell 1986, James, Bird and Wright 1989). It will be shown in due course that the geometry of nearly all the features in RHEED and off-axis THEED patterns is the same. Since THEED is well understood and RHEED is not, the former will be used to determine which parts of RHEED patterns are truly surface specific, and need a surface-diffraction theory to model them, and which are produced by diffraction predominantly from the bulk beneath. §4.2 is therefore given in entirety to a study of such transmission patterns within a theoretical framework chosen for its compatibility with the rod description of RHEED. The rest of the chapter is then spent on an analysis of RHEED itself, using the similarity between the THEED and RHEED perturbation expansions to understand the geometry.

4.1.3 Resonance geometry in the projection approximation

Before the analysis of off-axis transmission patterns is begun, it is necessary to explain in the simplest terms how the parabolic features in CB-RHEED patterns come about. This will then set the framework within which the THEED analysis of the next section will be performed.

As promised in Chapter 2, projection is taken down the z-direction in both the RHEED and THEED geometries. The two remaining directions are labelled x and y. † The y direction is taken to be parallel to the surface in RHEED, and is thus perpendicular to the reciprocal lattice rods, which run along the x direction

† x and y are real space coordinates, and should not be confused with the reciprocal space deviation parameters used in Chapter 3.

(see figure 4.1.3). In THEED, the analogue of the rod is the systematic row, again perpendicular to y. In both geometries, then, the y-component of the 2-d orientation vector $\mathbf{K}$, namely K_y, is conserved to within a 2-d reciprocal lattice vector component G_y. The remaining x-direction is taken to point along the systematic row or rod. As mentioned earlier, the relaxation of periodicity in this surface-normal direction in RHEED leads to the "smearing" of the Bragg spots to form reciprocal lattice rods, labelled by G_y. Some smearing will occur due to the presence of the surface. In addition, a finite penetration depth inside the crystal will further reduce the periodicity seen by an incident electron, causing greater smearing. RHEED is explained in terms of these rods on the assumption that the smearing is sufficient for there always to be significant diffraction into any value of K_x along each rod, subject to the constraints of energy conservation. It turns out that in a projected geometry the features associated with resonance can be explained with reference to just two rods.

In projection the governing equations will be those due to Kambe (1967) in the form derived in §2.3, viz.

$$\frac{d^2\psi_{G_y}}{dx^2} + K_x^2(G_y)\psi_{G_y} = \sum_{G'_y} U_{G_y - G'_y}(x)\psi_{G'_y}(x) \qquad (4.1.1)$$

where

$$K_x^2(G_y) = K^2 - (K_y + G_y)^2 . \qquad (4.1.2)$$

The form of the 1-dimensional surface-normal potential $U_0(x)$ is sketched in figure 4.1.2. The positions of the vacuum potential, the real part of the mean inner potential $\overline{U}$ and a possible bound state of the potential are all indicated. $\overline{U}$ is just the average elastic potential inside the crystal, given by the $\mathbf{g} = \mathbf{0}$

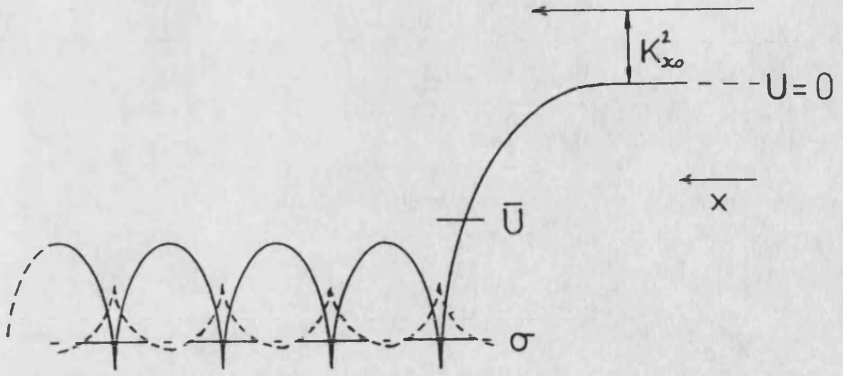

Figure 4.1.2. Schematic of the rod potential $U_0(x)$. The level of the vacuum zero, the mean inner potential and a bound state eigenvalue σ are all marked. The form of the deepest bound eigenstate is shown dashed. Also shown is the energy K_{xo}^2 of an incident plane wave.

structure factor;

$$\overline{U} = U_0 = \frac{1}{\Omega_c} \int_{\Omega_c} d^3\mathbf{r} \; U(\mathbf{r}), \tag{4.1.3}$$

where Ω_c is the unit cell volume. If $U(\mathbf{r})$ is allowed to become complex, a mean absorptive potential $\overline{U'}$ may be defined in exactly the same way. It is this mean absorptive potential which basically governs the penetration of incident electrons into a specimen. We return to this later, but for the moment ignore $\overline{U'}$ (assumed small), for the sake of convenience.

The (zero-potential) construction for Bragg diffraction in projection (see figure 4.1.3) is the intersection of the Ewald sphere with the plane of the zero-layer reciprocal lattice rods. This intersection describes what may be considered an Ewald circle, whose radius *changes* with incident orientation $\mathbf{K}$, since in RHEED both k and its z-component k_z are conserved quantities.

Figure 4.1.4 shows one such Ewald circle which cuts both the inside and outside

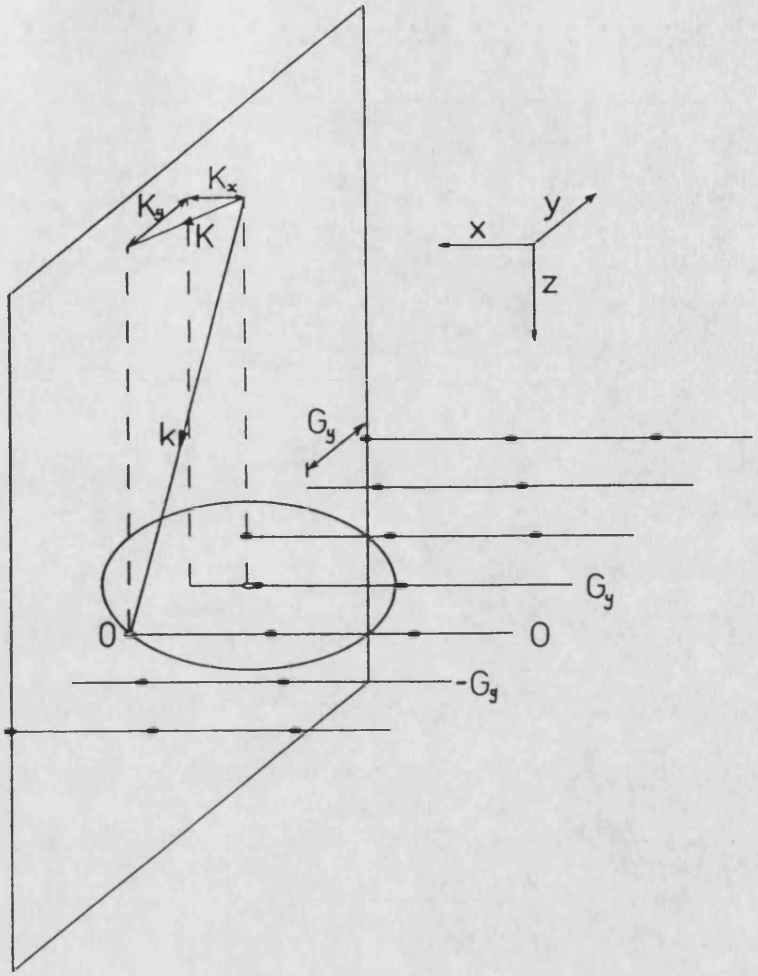

Figure 4.1.3. Schematic showing the circular intersection of an Ewald sphere with the zeroth layer of the reciprocal lattice, lying in the xy plane. (After Ichimiya, Kambe and Lehmpfuhl 1980) Each rod (of which $0, G_y$ and $-G_y$ are labelled) is drawn with *bulk* reciprocal lattice points marked on it.

of the specimen. The centre of the circle lies at the projection of the centre of the Ewald sphere onto the ZOLZ plane.

For convenience the circle in figure 4.1.4 is made the same radius inside as outside, though in practice $\overline{U}$ has the (refractive) effect of changing the x-component of the wavevector $\mathbf{K}$ from K_{xo} outside, to K_{xi} inside the crystal, via

$$K_{xi}^2 = K_{xo}^2 - \overline{U}. \tag{4.1.4}$$

Since the potential $U(\mathbf{r})$ is everywhere negative, so too is $\overline{U}$. The incident

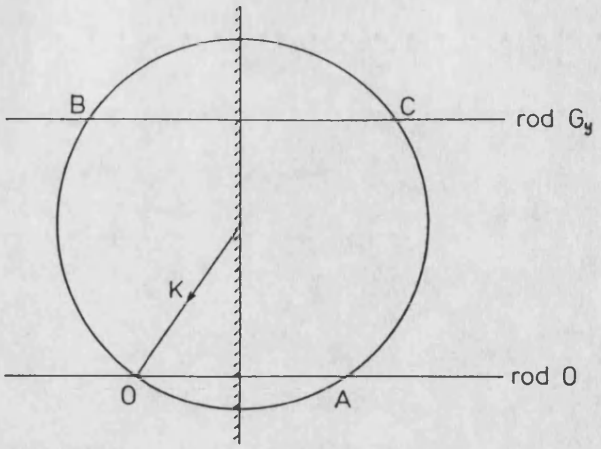

Figure 4.1.4. Ewald circle for the incident orientation **K**. The (real-space) surface is shown schematically to indicate that electrons incident at O on the zeroth rod will be reflected to A. Transitions to and from positions such as B and C on rod G_y, are also possible.

energy component in the x direction, K_{xo}^2, is clearly positive, so it follows that all incident electrons are able to enter the crystal, but only those inside with $K_{xi}^2 > |\overline{U}|$ are able to leave. If the Ewald circle is tangential to a rod nG_y, where n is an integer, then a diffracted wave will be excited parallel to the crystal surface. It is this wave which is responsible for "surface resonance". As figure 4.1.5 shows, (and see Ichimiya, Kambe and Lehmpfuhl 1980) the locus of the centres of the Ewald circles tangential to a given rod describes a parabola, which is of course the parabola under discussion.

These parabolas come in pairs, corresponding to the Ewald circle being tangential to the $+nG_y$ and $-nG_y$ rods. From now on, n is taken as a positive integer, and $\pm nG_y$ describes a pair of rods giving rise to a pair of parabolas. In order to derive an equation for the locus of the parabolas, it is necessary only to write down an expression for energy conservation between the surface-parallel wave and the plane wave outside the crystal, as observed in experiment.

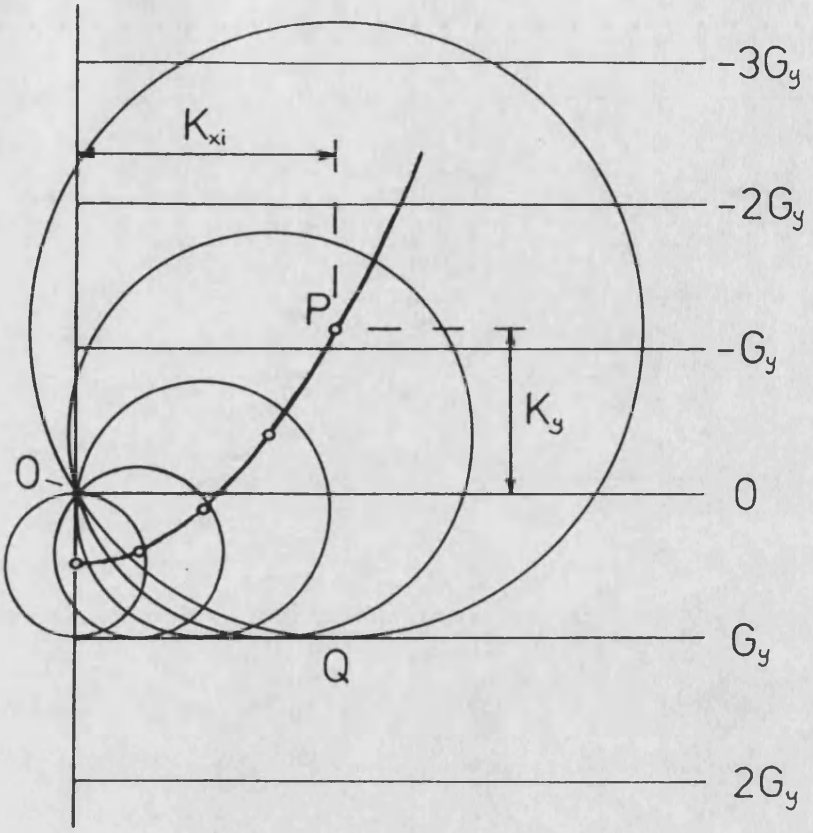

Figure 4.1.5. Zero-potential construction showing that the locus of the centre of Ewald circles tangential to a rod and passing through the origin describes a parabola in reciprocal space. (After Ichimiya, Kambe and Lehmpfuhl 1980.)

Unfortunately, in this plane wave description there is an ambiguity associated with whether the surface-parallel wave is treated as being inside or outside the crystal (eg Ichimiya, Kambe and Lehmpfuhl 1980). Each possibility gives rise to a parabola, with a gap between the two, caused by $\overline{U}$. Peng and Cowley (1986) suggest that this explains the gap between a parabola and its envelope, though this will be shown not to be the case. In fact, the ambiguity will disappear altogether in a moment, when the surface-parallel state is treated more carefully. For now, it is assumed for the sake of argument that the surface-parallel wave is inside the crystal, so $K_{zi} = 0$ for this wave. Since in figure 4.1.5 OP=QP,

energy conservation then gives

$$(K_y \pm nG_y)^2 = K_{xi}^2 + K_y^2 \tag{4.1.5}$$

or, transforming K_{xi}^2 via (4.1.4) to represent an orientation outside the crystal,

$$K_{xo}^2 = \pm 2nG_yK_y + n^2G_y^2 + \overline{U}. \tag{4.1.6}$$

This is the equation of the parabolic locus of the Ewald circle centres, as derived by Ichimiya, Kambe and Lehmpfuhl (1980), Peng and Cowley (1987) and others. Of course, as has been stated, the Ewald circles are a zero-potential construction, yet the Marten and Meyer-Ehmsen (1985) explanation for resonance is in terms of the surface-diffracted wave coupling into the *bound states* of the surface-normal or rod potential $U_0(x)$. As pointed out by Bird (1987), the electrons coupled into any such state are unlikely to be well described using plane waves in both the x- and y-directions. In the x-direction electrons will be in an eigenstate of the rod potential which may indeed be bound. This apparent loss of energy of the incident electrons is possible using the y-direction energy as a "sink", since only the 2-dimensional energy K^2 need be conserved. Note that in all the examples studied below, the systematic *row* potential has only one bound state, which will be the 1-dimensional equivalent of a $1s$ state. Although extra states may exist at the surface (see later), their form and eigenvalue will essentially be the same. It is the coupling into any of these bound states, sketched in figure 4.1.2, which is of interest in this chapter.

Since the surface-parallel wave is now an eigenstate of the whole potential, both inside and outside the crystal, it has a definite energy eigenvalue, without ambiguity. Let the eigenvalue of such a bound state be σ relative to the mean

inner potential, $U = \overline{U}$. Then the Ewald circle construction no longer expresses energy conservation; instead

$$\sigma + (K_y \pm nG_y)^2 = K_{xo}^2 - \overline{U} + K_y^2 \tag{4.1.7}$$

or

$$K_{xo}^2 = \pm 2nG_yK_y + n^2G_y^2 + \sigma + \overline{U}. \tag{4.1.8}$$

As will be discussed in much greater detail in later sections, the effect of this extra energy term is to shift a parabola from its free-electron position (4.1.6). In this case, the parabolas may be pictured, if helpful, as being constructed from Ewald circles tangential to a line *parallel* to the $\pm n$th G_y rod. Note that all this may (and later will) be derived directly from the Kambe equations (4.1.1).

So far, then, consideration has been made of the conservation of energy and of crystal momentum in the K_y direction. Much of the remaining physics of the problem lies in determining to what extent the momentum component K_x is conserved in RHEED patterns. The framework within which this conservation is investigated will now be introduced.

4.1.4 The two-rod model

The two-rod model will be at the heart of both the transmission and reflection analysis which follows. By definition, each incident wavevector **K** terminates on the zeroth rod. Each of the parabolas, and indeed nearly all the other RHEED features, can be constructed geometrically by including just one more rod, labelled by $nG_y = H$, say. In this case, the Kambe equations (4.1.1) reduce to the coupled "two-rod equations"

$$\left[-\frac{d^2}{dx^2} + U_0(x) - K_{xo}^2\right]\psi_0 = -U_{-H}\psi_H \tag{4.1.9}$$

and

$$\left[-\frac{d^2}{dx^2} + U_0(x) - \left(K_{xo}^2 \pm 2K_y H - H^2\right)\right] \psi_H \;=\; -U_H \psi_0. \qquad (4.1.10)$$

In the perturbation expansion of these equations, the potentials $U_{\pm H}$ will be treated as small. The basis states from which we expand are the solutions to (4.1.9&10) with the right-hand sides set to zero; these are the eigenstates of the zeroth rod potential $U_0(x)$. ψ_0 and ψ_H are therefore just states of $U_0(x)$ with *different energies*. Since these basis states need not be plane waves, what follows will be a distorted wave Born approximation (eg Schiff 1968), in which the intra-rod scattering will be incorporated into the unperturbed Hamiltonian, and the inter-rod contributions, governed in strength by $U_{\pm H}$, will be treated as a perturbation.

These two-rod equations are identical in form to those given by Ohtsuki (1968) and McRae (1979) for the analysis of surface resonance in low energy electron diffraction (LEED). McRae's mechanism for resonance is very similar to that suggested by Marten and Meyer-Ehmsen (1985) for RHEED. However, the kinetic energy of a LEED electron ($\leq$ 1keV) is much more comparable with that of the specimen electrons, so scattering in LEED tends to be very strong. At such energies there are further complications, since (for example) exchange effects between the incident and crystal electrons should not be ignored. It is therefore felt that if anything, the two-rod approximation should be more suited to RHEED than LEED. Finally, it should be said that there may be differences in the shape of the rod potential $U_0(x)$ close to the surface (both in the real and the absorptive imaginary parts) between the two energy régimes. These differences may

play a vital rôle in determining both the boundary conditions and the penetration depths of the incident electrons, and the states close to the surface into which these electrons may couple. Thus it should not be assumed that surface effects in LEED automatically translate to surface effects in RHEED.

4.2 ANALYSIS OF OFF-AXIS TRANSMISSION PATTERNS

4.2.1 Introduction

This section deals with the analysis of off-axis transmission patterns, with a view to transcribing the results to the RHEED case. The justification for this is that all the types of feature seen in CB-RHEED patterns at microscope voltages are observable in a transmission pattern taken from the same orientation. It is therefore the *geometry* of the patterns which we wish to explain on physical grounds. No suggestion is made in this section that the relative *intensities* of features in RHEED patterns may be described by direct comparison with THEED. However, as will become clear, it is possible to eliminate some of the possible causes of the RHEED features, and to deduce their possible surface-sensitivity, by first understanding off-axis transmission patterns.

The first detailed observation that the parabolic features of interest are present in equivalent transmission patterns was given by Lehmpfuhl and Dowell (1986), for the rather weak Silicon (111) surface. Similar observations have been reported by the Arizona group, notably Peng, Cowley and Yao (1988), and Yao and Cowley (1989). Although the patterns in these papers are taken from stronger scattering surfaces, namely GaAs(110) and Pt(111), the analysis offered is rather confused, and some of the crucial points would appear to have been missed.

One common feature of these papers is that the THEED patterns shown are all off-axis Kossel-Möllenstedt patterns, similar in construction to the Vincent patterns of Chapter 3. Although the features of interest are certainly visible in such patterns (and just about any other pattern taken at the correct orientation), the geometry is not nearly so clear as in bright-field, large-angle convergent-beam (LACBED) patterns, as introduced by Tanaka *et al.* (1980). These patterns are produced by over- (or under-) focusing a large-angle incident probe, and using the selected-area aperture to pick out the zeroth beam at a position where the (otherwise overlapping) discs are separated. The drawback of the over-focusing is that a large, flat area of the specimen is required, perhaps thousands of Ångstroms in diameter. However, the additional feature of the patterns, that both image and diffraction information are present, makes the search for an acceptable area, and the interpretation of distortions incurred, somewhat easier.

One of the differences between the THEED and RHEED analyses which follow should now be outlined. "Resonance" is at least a second order effect in the inter-rod potentials $U_{\pm H}$; it is necessary to scatter into and out of a bound state in order to observe intensity changes due to the resonance mechanism. However, as will become clearer, the *geometry* of the patterns is contained within first order expressions, either for scattering into *or* out of a bound state. In RHEED, at least one scattering event ("reflection") must occur for there to be any observed flux. Thus in §4.1.3 attention was limited to the scattering *from* a state out into the vacuum, without much caring how the electrons first became surface-parallel. By contrast, the LACBED patterns of this section are all taken in the bright-field. In this case we look at the first scattering event, *from* the incident beam

into bound (and other) states, and there is no need to keep track of the scattered orientation of the electrons in order to determine the diffraction geometry.

Figure 4.2.1 shows 200kV bright-field LACBED patterns taken from close to the Pt[231] and the GaAs[116] axes. In order to mimic the reflection geometry, these patterns are centred about a position shifted from the band which plays the equivalent rôle to the surface planes in RHEED. These patterns are very similar to their RHEED equivalent; *each line or curve in the RHEED patterns of figure 4.1.1 may be seen in the equivalent THEED pattern here.* Although the converse is not true, the extra lines in the latter are all HOLZ lines, which are assumed weak and therefore to have no effect on the *positions* of the ZOLZ lines. It should be stressed that the similarities are observed at all axes, and the ones exhibited are chosen only because they show the features clearly. It will be seen later that the two sets of patterns can be simulated geometrically by the same method, based on simple perturbation arguments, derived first for the transmission case.

It should be reiterated that the equivalent of a "rod" potential in THEED is a systematic row potential, as formed for example by the Fourier components $U_{\pm n\mathbf{g}}, n = 1 \rightarrow \infty$. [In a transmission systematic Laue geometry, the component $U_{\mathbf{0}} = \overline{U}$ affects all beams uniformly, and need not, therefore, be included.] To ensure consistency with the RHEED description, the systematic rows used will be those through reciprocal lattice points of constant K_y. Thus for the Pt[231] patterns, the "rods" from the $(\bar{1}1\bar{1})$ surface become a $(\bar{1}1\bar{1})$-type systematic row. Of course, this potential is *completely periodic* in THEED, so it is necessary to satisfy the Bragg law when making "inter-rod" transitions (ie $K_x \rightarrow K_x + G_x$);

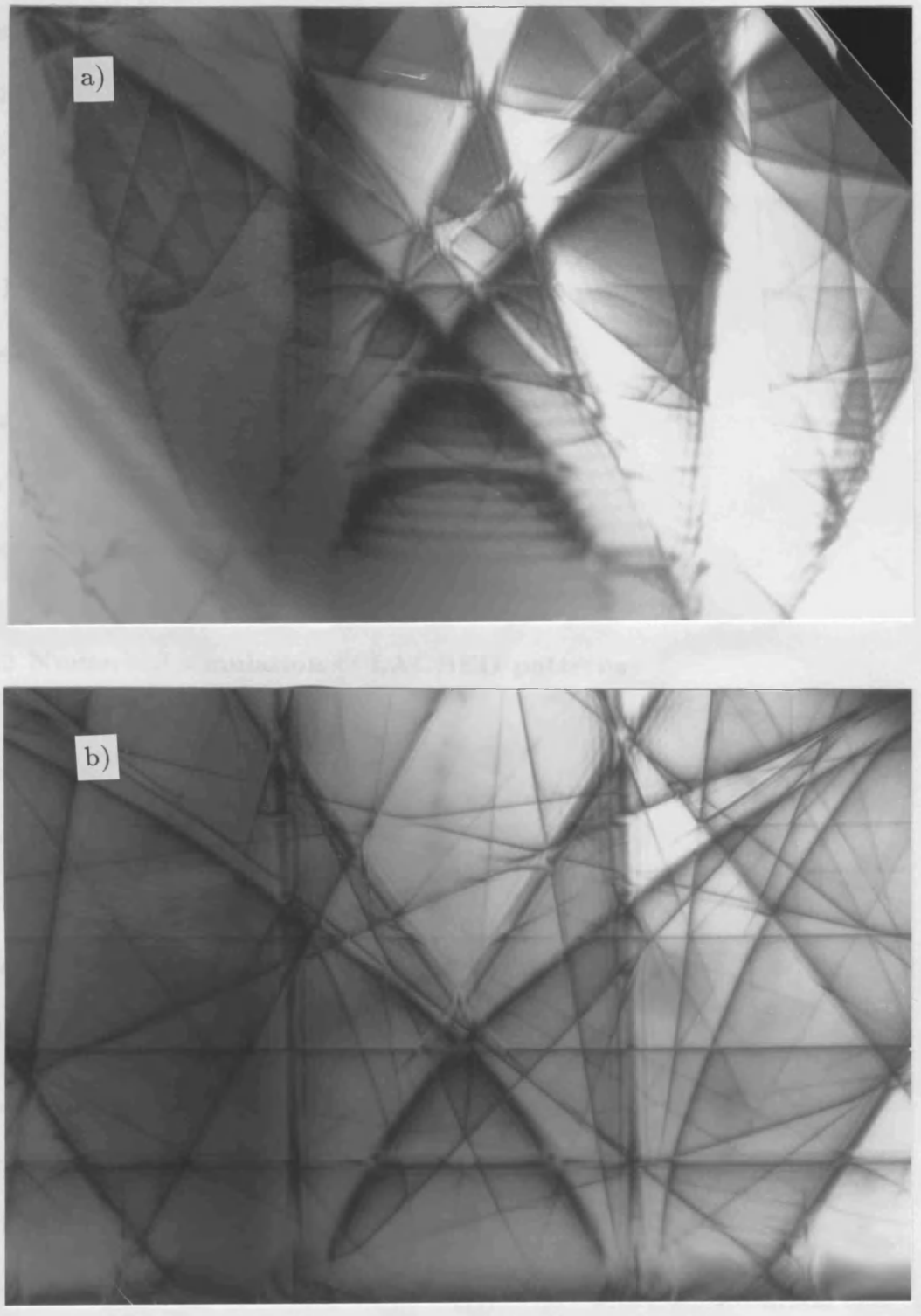

Figure 4.2.1. 200kV off-axis LACBED transmission patterns (courtesy A G Wright). These patterns are taken from the same materials and orientations as the CB-RHEED patterns in figure 4.1.1. (a) is from close to Pt[231], and (b) from close to GaAs[116].

in principle this condition is relaxed in the RHEED case. Once it has been shown in this section that RHEED and THEED patterns are geometrically similar, it will be seen in the next that many of the causes of dissimilarity between the two arise from the differences between the 1-dimensional potentials, and how in the RHEED case the electron wavefield is matched from the vacuum to the rod potential. Following the work of Marten and Meyer-Ehmsen (1985), the main thrust of this transmission study will be to understand the effects of coupling into the deepest (and, if appropriate, other) bound states of the systematic row potential, and to what features this coupling leads in a diffraction pattern.

4.2.2 Numerical simulation of LACBED patterns

As in the three-beam analysis of Chapter 3, it will prove useful to have a full, numerical theory with which to compare our approximations. Again the many-beam equations are used to provide this. Since the HOLZ lines of the LACBED patterns are not observed in the RHEED patterns, and are assumed to be too weak to alter the line geometry, all the simulations will be performed in projection, so the potential and the Bloch-waves will be 2-dimensional. It is important to note that the 2-dimensional eigenvalues and eigenvectors introduced in §2.3.1, and here labelled by the branch index (m), are *not* the same as those of the 1-dimensional systematic row, here labelled (j), to which the discussion will later be confined. Absorption will also be ignored at this stage, again because the aim of this analysis is to understand only the *position* of the diffracted lines and curves. Therefore, the diffracted amplitudes at the exit face of a perfect transmission specimen in the symmetric Laue geometry, as a function of the

2-dimensional orientation **K**, are given by (2.3.10):

$$A_{\mathbf{G}}(\mathbf{K},t) = \sum_m C_{\mathbf{0}}^{(m)*}(\mathbf{K}) C_{\mathbf{G}}^{(m)}(\mathbf{K}) \exp\left(\frac{-is^{(m)}t}{2k}\right), \qquad (4.2.1)$$

where t is of course the specimen thickness. Since in a bright-field pattern only the component $\mathbf{G} = \mathbf{0}$ is of interest, the diffracted intensity at any orientation **K** is given by

$$I_{\mathbf{0}}(t) = |\sum_m |C_{\mathbf{0}}^{(m)}|^2 \exp\left(\frac{-is^{(m)}t}{2k}\right)|^2 = \sum_{m,n} |C_{\mathbf{0}}^{(m)} C_{\mathbf{0}}^{(n)}|^2 \cos[(s^{(m)} - s^{(n)})\frac{t}{2k}]. \qquad (4.2.2)$$

The cosine term in the second of these expressions is an interference term, and is responsible for the fringes seen parallel to, and either side of the main diffraction lines. For the purposes of finding only the positions of these main lines, the time-consuming double summation in (4.2.2) is unnecessary. The interference term between different branches is therefore ignored, by setting $m = n$, leaving as the quantity to be calculated

$$I_{\mathbf{0}}(\mathbf{K}) \approx \sum_m |C_{\mathbf{0}}^{(m)}(\mathbf{K})|^4, \qquad (4.2.3)$$

which is *independent* of the specimen thickness. Note that this simplified intensity expression still contains all the ZOLZ pattern geometry; for example, at orientations **K** close to a Bragg condition, $C_{\mathbf{0}}(\mathbf{K})$ will be reduced (assuming weak diffraction), so (4.2.3) will give a reduced bright-field intensity, corresponding to a point close to a deficiency line.

In principle, then, the LACBED patterns of figure 4.2.1 could be simulated by calculating the Bloch-wave coefficients $C_{\mathbf{0}}$ (via diagonalisation of the many-beam matrix) and performing the sum (4.2.3) at as many orientations **K** as

required. It should be borne in mind that experimental LACBED patterns cover a large range of incident orientations, some of which may be well away from a zone axis. Unfortunately, the standard methods of performing a many-beam simulation of diffracted intensity are not really suited to analysis well away from the "centre" of a pattern. This is because it is customary to use the many-beam equations to simulate zone-axis patterns, in which the strength of the structure amplitudes may be considered to fall off at the same rate in all directions. Hence all the ZOLZ reciprocal lattice points within a given radius of the zone centre are included in the calculation; the off-diagonal (potential) part of the many-beam matrix is filled up once and stays the same throughout the calculation. The stronger the zone axis, the more beams N must be included, and the longer it takes for the diagonalisation to be performed ($\propto N^3$). This is bad enough at a zone axis, but is even worse for off-axis analysis of a strong scatterer such as Pt. For an orientation vector $\mathbf{K}$ well away from the origin O, the Ewald circle, centred on $\mathbf{K}$ and passing through O, is rather large and extends to a maximum distance $2K$ from the origin. If all of the reciprocal lattice vectors inside *all* such Ewald circles were included in a single many-beam matrix, it could become enormous. Diagonalisation at many orientations, as is necessary to simulate the LACBED patterns, would then take a prohibitively long time.

One solution to this problem is to be selective about which beams to include in the many-beam matrix at any given orientation. As a guide to how to perform this selection, it is again useful to look first at the zero-potential limit. In this limit, the only beams which will be excited are those for which the diagonal terms in the many-beam matrix match the diagonal term of the incident electrons; that

is, only those $\mathbf{G}$ for which $(\mathbf{K}+\mathbf{G})^2 = K^2$ need be included. Geometrically, this is equivalent to excluding all zero-layer reciprocal lattice points which do not lie exactly on the Ewald circle. If a weak potential is now "switched on", there will be additional coupling of the incident beam into directions other than those exactly on the Ewald circle, though such a circle will still describe the locus of maximum coupling. The simplest and most natural way to reduce the size of the many-beam matrix at any one orientation $\mathbf{K}$ is therefore to select only those beams $\mathbf{G}$ for which

$$|(\mathbf{K}+\mathbf{G})^2 - K^2| \leq \lambda, \tag{4.2.4}$$

where λ is a single parameter to be determined. Geometrically, the constraint (4.2.4) is equivalent to putting a strip either side of the Ewald circle, of a width determined by the value of λ. Because of the square dependence of K on λ, this strip gets narrower as the orientation gets further from the origin, so the number of beams required is more or less uniform over a whole pattern, for a given choice of λ.

For the particular application under discussion here there is a perfectly natural way in which to determine the parameter λ. Since the mechanism of most interest is the coupling of electrons into the deepest bound state of the 1-dimensional systematic row potential, it is necessary that such a state be well approximated. Sufficient Fourier components of the systematic row potential must therefore be included for the deepest parts of the real-space potential to be well simulated. Since these deep regions have the fastest variation of potential with distance, a Fourier series expansion which produces accurate bound states will automatically simulate the higher energy states even better. One way to monitor the

convergence of the potential is to look at the variation of the eigenvalue $\sigma^{(1)}$ of the deepest bound state of the row potential. If insufficient potential components are used, the sharp regions of the real-space potential will become smeared, and the solution of the diffraction equations will produce a less bound eigenvalue. As the number of beams (and hence the number of potential components) is increased, the value of $\sigma^{(1)}$ gets deeper until it converges. A criterion for the choice of λ for this application is therefore that, for an orientation whose Ewald sphere is tangential to a systematic row, the outer portion of the Ewald "ring" should intersect a length of the row containing sufficient reflections to produce a converged value of the deepest bound eigenvalue $\sigma^{(1)}$.

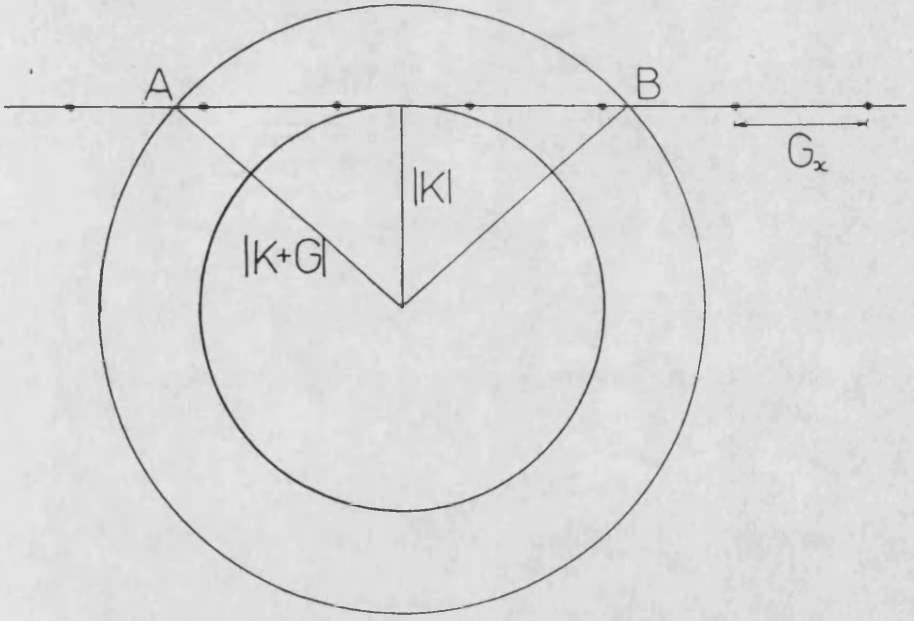

Figure 4.2.2. Schematic of the convergence criterion. The inner Ewald circle is tangential to a systematic row. The chord AB of the outer circle must contain enough beams to produce a converged eigenvalue of the row's deepest bound state. The separation of the circles is determined by the parameter λ.

This criterion is illustrated schematically in figure 4.2.2. If the gap between

reciprocal lattice points along the systematic row is G_x, and N_c is the number of beams required for convergence, then from figure 4.2.2,

$$AB = (N_c - 1)G_x \; = \; 2\left[(\mathbf{K}+\mathbf{G})^2 - K^2\right]^{\frac{1}{2}}. \qquad (4.2.5)$$

Now, the outer circle in figure 4.2.2 represents an extreme value of the inequality (4.2.4). The term in square braces is therefore just λ, and (4.2.5) leads to the simple convergence criterion

$$\lambda \geq \frac{1}{2}\left[(N_c - 1)G_x\right]^2 \qquad (4.2.6)$$

For the simulation of the Pt[231] pattern, the "surface" planes are $(\bar{1}1\bar{1})$. In this case 11 $(\bar{1}1\bar{1})$-type beams are found to give a satisfactory convergence of $\sigma^{(1)}$, leading to the value $\lambda = 180$ Å^{-2}. This produces a many-beam matrix for the 2-dimensional LACBED simulations which is up to 40×40 beams in size. On a SUN4 computer, using optimised diagonalising routines, this means a 101×101 orientation 2-dimensional scan can be performed in about eight hours. The calculations are much quicker for weaker scatterers such as GaAs, since N_c (and hence λ) is smaller.

For the particular range of orientations shown in the Pt simulation below, close to the [231] axis, this method is only slightly faster than a conventional zone-axis calculation. Should we wish to scan further out from the zone axis, the gain in time would soon become apparent. This selection process may be of use in other diffraction problems, in which case λ must be chosen so that the real-space potential responsible for the features of interest is well simulated.

Figures 4.2.3 and 4.2.4 show experimental and simulated LACBED patterns from the [231] axis of Pt and the [116] axis of GaAs. The "surface" systematic

Figure 4.2.3. Experimental 200kV LACBED pattern (courtesy A G Wright) and many-beam simulation from close to Pt[231]. See text for details.

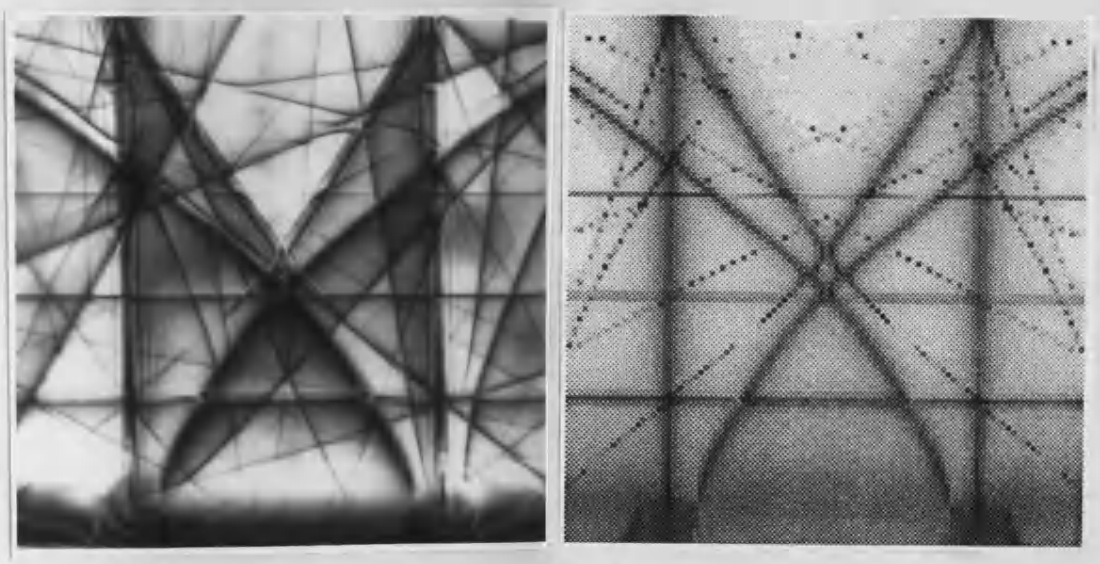

Figure 4.2.4. Experimental 200kV LACBED pattern (courtesy A G Wright) and many-beam simulation from close to GaAs[116]. See text for details.

row for GaAs[116] contains $(\bar{2}20)$-type reflections. This row is well simulated by a 7-beam calculation, leading to a strip-width $\lambda = 90\text{Å}^{-1}$. In both cases, the orientation scan is for $-4 \leq K_y/\text{Å}^{-1} \leq 4$ horizontally and $1 \leq K_x/\text{Å}^{-2} \leq 9$ vertically. As a guide to the area of the reciprocal lattice covered by these scans,

$G_{111} = 2.77\text{Å}^{-1}$ in Pt, and $G_{220} = 3.15\text{Å}^{-1}$ in GaAs. In both simulations, the intensity given by (4.2.3) has been scaled to cover the range $[0, 1]$ to highlight the contrast between the deficit lines of interest and the background. The experimental patterns are similar to those in figure 4.2.1. Clearly, this method of orientation-dependent beam selection produces satisfactory agreement with experiment in terms of producing the correct positioning of the major zero-layer features. These simulations will provide the full numerical back-up to the perturbation work which will now be introduced.

4.2.3 A perturbative two-rod theory in transmission

This section contains a development of two-rod theory in transmission. The essential differences between what follows here and the RHEED two-rod theory outlined in §4.1 are as follows:

(i) Rod potentials are replaced by systematic row potentials, so there is no relaxation of Bragg's Law in the x-direction. That is, crystal momentum is conserved.

(ii) The boundary conditions are at $z = 0$ and $z = t$, not at $x = 0$.

(iii) The perturbation expressions will contain thickness-dependent terms, which contribute only a shape function to the diffraction lines.

(iv) The mean inner potential will be ignored

(v) Absorption will be ignored.

(vi) Emphasis will be placed on scattering *from* the incident beam into other states.

As in RHEED two-rod theory, the basis states for expansion will be the states of the zeroth rod potential, and the coupling between rods will be treated as

a perturbation. This rather artificial separation into scattering along the rods which may be strong, and in between rods, which is assumed weak, will clearly ignore the dynamical effects due to other sets of systematic rows. Such effects may be minimised by working at axes where the the "surface" systematic row gives the strongest diffraction, and are further reduced by the fact that the patterns are off-axis, so it is unlikely that a significant portion of any other ZOLZ row will be excited.

As the potential will be split into systematic row contributions, it is convenient to write the starting diffraction equation (2.2.22) as

$$\left[-\nabla_{\mathbf{R}}^2 + U_0(x) + U(x,y)\right]\varphi(x,y,z) \;=\; 2ik\frac{\partial\varphi}{\partial z} \tag{4.2.7}$$

where $-\nabla_{\mathbf{R}}^2 + U_0(x)$ is treated as the unperturbed Hamiltonian, with eigenstates φ_0, and the perturbation is [compare with (2.2.23)]

$$U(x,y) \;=\; \sum_{G_y \neq 0} U_{G_y}(x)\exp(iG_y y). \tag{4.2.8}$$

Since the potential for the basis states φ_0 depends only on x, the diffraction equations are now separable into x, y, and z components, rather than just $\mathbf{R}$ and z, as was the case in Chapter 2. Writing $\varphi_0 = \psi(x)Y(y)Z(z)$ and forcing the y dependence (giving inter-row scattering) to be plane-wave like, leaves the $\psi(x)$ as Bloch states of the 1-dimensional, zeroth systematic row, satisfying

$$\left(-\frac{d^2}{dx^2} + U_0(x)\right)\psi^{(j)}(x,K_x) = \sigma^{(j)}(K_x)\psi^{(j)}(x,K_x). \tag{4.2.9}$$

The 1-dimensional eigenvalues $\sigma^{(j)}$ of $\psi^{(j)}$ are related to the 2-dimensional eigenvalues $s^{(m)}$ of $\tau^{(m)}$ via

$$\sigma^{(j)}(K_x) \;=\; s^{(m)}(K_x,K_y) \;-\; K_y^2, \tag{4.2.10}$$

since a plane-wave K_y dependence has been assumed. Denoting the excitation amplitude of each 1-dimensional Bloch state by $\varepsilon^{(j)}(K_x)$, the unperturbed eigenstates may be written down by comparison with (2.3.7):

$$\varphi_0 = \sum_j \varepsilon^{(j)}(K_x)\psi^{(j)}(x, K_x)\exp(iK_y y)\exp\left(-\frac{iz}{2k}\left\{\sigma^{(j)} + K_y^2\right\}\right). \quad (4.2.11)$$

These basis states may now be perturbed by the potential $U(x, y)$, which, by analogy with the analysis in Chapter 3, will transform K_y by a G_y, and cause intra-rod scattering between branches (j), with an amplitude which must be depth-dependent. The perturbed wavefunction is therefore

$$\varphi = \sum_{j,G_y} a_{j,G_y}(z)\psi^{(j)}\exp\left[i(K_y + G_y)y\right]\exp\left(-\frac{iz}{2k}\left\{\sigma^{(j)} + (K_y + G_y)^2\right\}\right), \quad (4.2.12)$$

with boundary conditions in this symmetric Laue geometry determined by comparison of (4.2.11) and (4.2.12):

$$a_{j,G_y}(0) = \varepsilon^{(j)}\delta_{0,G_y}. \quad (4.2.13)$$

Note that if the projected reciprocal lattice around the axis of interest is not rectangular, then a perpendicular transition between rods will not satisfy the Bragg condition $K_x \rightarrow K_x + G_x$. In this case, the eigenvalue on rod $\pm H$ into which we must couple is related to the eigenvalue on rod 0 via

$$\sigma_{\pm H}^{(j)} = \sigma_0^{(j)}(K_x \mp \Delta), \quad (4.2.14)$$

where Δ is the offset between rods 0 and H, as defined in figure 4.2.5. The inclusion of this offset is largely a matter of book-keeping; since it only lengthens the equations yet further, it will consequently be omitted until needed. Note that such an offset applies to the labelling of eigenstates as well as eigenvalues.

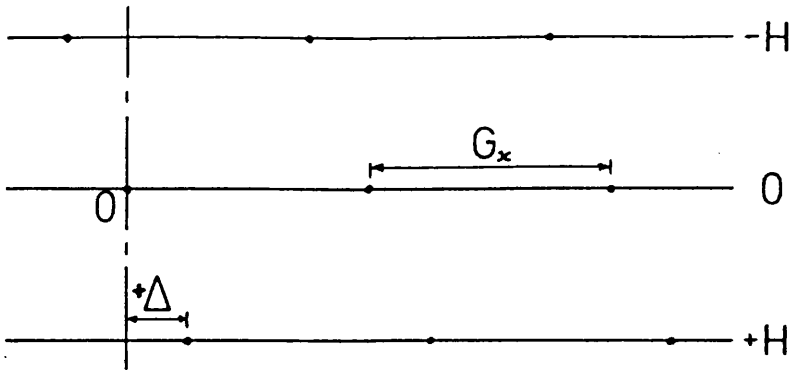

Figure 4.2.5. Schematic showing, and defining the sense of, the offset Δ between reciprocal lattice rods for a pole without mirror symmetry about rod 0.

The wavefunction (4.2.12) may now be substituted into the starting equation (4.2.7). The processing of the resulting expression to produce the required form is entirely analogous to the derivation of the Howie-Whelan equations in §2.3, except that sifting integrals in the x- and y-directions are performed separately. As might be expected, the (plane-wave) y-components are sifted out altogether, and the x-dependent Bloch-states form a 1-dimensional matrix element about the inter-rod potentials:

$$\frac{da_{j,G_y}}{dz} = \frac{1}{2ik}\sum_j \sum_{G'_y \neq G_y} a_{j',G'_y} \langle \psi^{(j)} | U_{G_y - G'_y} | \psi^{(j')} \rangle_x \times \exp\left(\frac{iz}{2k}\left\{\sigma^{(j)} - \sigma^{(j')} + (K_y + G_y)^2 - (K_y + G'_y)^2\right\}\right). \tag{4.2.15}$$

The matrix element in this equation contains most of the physics of the problem; it is this term which governs the strength of inter-rod transitions, and from which the crucial K_x conservation arises. Although the states $\psi^{(j)}$ and $\psi^{(j')}$ will both be Bloch states of the zeroth-rod potential, the matrix element may be thought of as describing the transfer of flux from a Bloch state on one rod to a different state on another rod $G_y - G'_y$ away, with a strength given by the inter-rod potential $U_{G_y - G'_y}$. Before splitting the equations (4.2.15) into perturbation

orders $a^{(n)}$, as in §3.2, the two-rod equations for THEED may first be derived. In this case only 0 and H need be included as possible values of G_y and G'_y. To keep the size of these equations manageable, it is convenient to write

$$\sigma^{(j)} - \sigma^{(j')} - 2K_y H - H^2 = \Omega^{jj'}, \tag{4.2.16}$$

though care must be taken to ensure that the ordering of the labels (j) and (j') is kept absolutely consistent. The resulting two-rod equations are

$$\frac{da_{j,0}}{dz} = \frac{1}{2ik} \sum_{j'} a_{j',H} \langle \psi^{(j)} | U_{-H} | \psi^{(j')} \rangle_x \exp\left(i \frac{\Omega^{jj'} z}{2k} \right) \tag{4.2.17}$$

and

$$\frac{da_{j',H}}{dz} = \frac{1}{2ik} \sum_{j} a_{j,0} \langle \psi^{(j')} | U_{H} | \psi^{(j)} \rangle_x \exp\left(-i \frac{\Omega^{jj'} z}{2k} \right). \tag{4.2.18}$$

First order terms

The amplitude coefficients may be split up into orders $a^{(n)}$ in precisely the same way as for the normal Howie-Whelan equations in Chapter 3. Again, the zeroth order terms are the initial conditions, this time given by (4.2.13). Since there is no incident excitation onto the H rod, the first order term on rod 0 is zero, and on rod H is given by

$$\frac{da^{(1)}_{j',H}}{dz} = \frac{1}{2ik} \sum_{j} \varepsilon^{(j)} \langle \psi^{(j')} | U_{H} | \psi^{(j)} \rangle_x \exp\left(-i \frac{\Omega^{jj'} z}{2k} \right). \tag{4.2.19}$$

Integration of this expression between the top surface $z = 0$ and some intermediate thickness z_1 yields

$$a^{(1)}_{j',H}(z_1) = \sum_{j} \varepsilon^{(j)} \langle \psi^{(j')} | U_{H} | \psi^{(j)} \rangle_x \left[\frac{\exp\left(-i \frac{\Omega^{jj'} z_1}{2k} \right) - 1}{\Omega^{jj'}} \right]. \tag{4.2.20}$$

It turns out that this expression already contains all the information required to determine the geometry of the LACBED patterns, within the denominator $\Omega^{jj'}$.

The whole term in square braces describes what may be considered a *modified Bragg condition*; it is a maximum when $\Omega^{jj'}$ is zero, and gives an oscillating fall-off of intensity either side. Since the terms in $\Omega^{jj'}$ are not necessarily plane-wave like, the condition $\Omega^{jj'} = 0$ is not a simple Bragg condition, but is a similar condition in which the 1-dimensional Bloch state eigenvalues play an important rôle. The locus of the (K_x, K_y) satisfying this condition will give the positions of the various lines in LACBED patterns, even though there is no first order intensity change in the bright field. To produce an intensity change, the approximation is taken to one extra term; this will then put flux back onto the zeroth rod, and so introduces double scattering terms analogous to the two-rod LEED amplitudes of McRae (1979). As we shall see, though, the modified Bragg condition $\Omega^{jj'} = 0$ will not be altered, which is why first order expressions predict the geometry correctly.

Second order terms

The second order amplitude required is that on rod 0. It is found by integration of the first order term on rod H, (4.2.20). In the general case described first, (j'') labels states "on" rod 0 into which the incident beam couples, (j') labels states "on" H, and (j) final states back on 0. [Of course each such state is actually a state of the zeroth rod potential, but this picture of propagation on a particular rod is useful.]

If the intent of this section were to simulate intensities, then the Bloch-waves $|\psi^{(j)}\rangle$ would need to be matched to plane waves underneath the specimen. This is an unnecessary complication; instead only the second order amplitude inside

the specimen need be calculated. Performing an iteration of the first order term (4.2.20) gives

$$a_{j,0}^{(2)}(t) = \sum_{j'j''} \varepsilon^{(j'')} \langle \psi^{(j)} | U_{-H} | \psi^{(j')} \rangle_x \langle \psi^{(j')} | U_H | \psi^{(j'')} \rangle_x \frac{it}{2k} \quad \times$$
$$\frac{1}{\Omega^{j''j'}} \left\{ \frac{1}{\Omega^{jj'}} \left[\exp\left(\frac{i\Omega^{jj'}t}{2k} \right) - 1 \right] - \frac{1}{\sigma^{(j)} - \sigma^{(j'')}} \left[\exp\left(\frac{i(\sigma^{(j)} - \sigma^{(j'')})t}{2k} \right) - 1 \right] \right\}. \tag{4.2.21}$$

The first line of this equation gives the basic strength of second-order diffraction associated with the zeroth rod, which is modulated by the "shape function" of the second line. This shape function contains three inter-dependent Bragg-type conditions. The first of these is the first-order condition $\Omega^{j''j'} = 0$. Noting from (4.2.16) that $\Omega^{jj'} = \Omega^{j''j'} + (\sigma^{(j)} - \sigma^{(j'')})$, these conditions may be expressed as

$$\Omega^{j''j'} = 0, \qquad \Omega^{j''j'} + (\sigma^{(j)} - \sigma^{(j'')}) = 0, \qquad \sigma^{(j)} - \sigma^{(j'')} = 0. \tag{4.2.22}$$

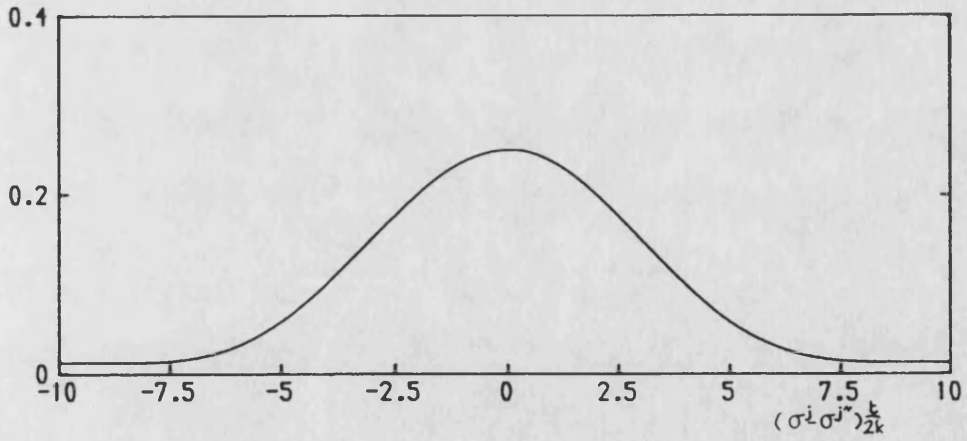

Figure 4.2.6. Probability shape function for the satisfaction of three inter-dependent modified Bragg conditions, given that one is satisfied. See text for details.

Let us assume that one of these conditions is satisfied, for example the first. Figure (4.2.6) is a plot of the modulus squared of the second line of (4.2.21)

as a function of $(\sigma^{(j)} - \sigma^{(j'')})\frac{t}{2k}$. Essentially, this plot indicates the probability shape function given that the first modified Bragg condition is satisfied. What it clearly shows is that the strongest intensity back on rod 0 will occur when an electron returns to a state with the same 1-dimensional energy as the one from which it left. Thus it makes no difference whether we consider scattering into or out of the state of interest. We shall for the moment ignore the possibility of degeneracies and assume that if $\sigma^{(j)} = \sigma^{(j'')}$, then the *states* $\psi^{(j)}$ and $\psi^{(j'')}$ are also the same. This simplifies (4.2.21), and as promised, leads to an amplitude with only one modified Bragg condition, identical to that in the first order term:

$$a_{j,0}^{(2)}(t) \approx \varepsilon^{(j)} \sum_{j'} \langle \psi^{(j)} | U_{-H} | \psi^{(j')} \rangle_x \langle \psi^{(j')} | U_H | \psi^{(j)} \rangle_x \frac{t}{2k} \quad \times$$
$$\frac{1}{\Omega^{jj'}} \left\{ \frac{1}{\Omega^{jj'}} \left[\exp\left(\frac{i\Omega^{jj'}t}{2k} \right) - 1 \right] - \frac{it}{2k} \right\}. \tag{4.2.23}$$

This expression will be compared with the second order RHEED amplitude in §4.3.

4.2.4 Branch-by-branch simulation of LACBED patterns

As mentioned before, the geometry of LACBED patterns can be deduced by mapping out the loci of the orientations (K_x, K_y) which satisfy the modified Bragg condition $\Omega^{jj'} = 0$. This may be achieved directly and simply by assuming the starting (and hence finishing) state to be the plane wave $\exp(iK_x x)$ on rod 0, with eigenvalue $\sigma^{(j)} = K_x^2$. Note that by choosing the initial state to be a plane wave, those Bragg lines corresponding to the systematic row reflections G_x will not be simulated. For these to appear, the states $\psi^{(j')}$ would need to be expressed as the sum of at least two plane waves, or in a full-blown Bloch-wave expansion. Also, therefore, this method will not simulate those positions

of enhanced intensity in RHEED patterns where a parabola crosses a G_x line. The analysis of these regions will require a "three-state" theory (though still two-rod), akin to that used in the three-beam work of Chapter 3; this is left until the section on RHEED, §4.3.

The equations to be solved for the line positions (K_x, K_y) in this case, then, may be found from (4.2.22) and (4.2.16), and using (4.2.14), to be

$$K_x^2 \mp 2K_y H - H^2 - \sigma^{(j')}(K_x \mp \Delta) = 0, \qquad (4.2.24)$$

which, not surprisingly, bears a striking resemblance to the RHEED parabola equation (4.1.8), apart from the insertion of K_x as a good quantum number for the eigenvalues $\sigma^{(j')}$, the associated shift Δ between neighbouring rod potentials, and the omission of $\overline{U}$. The most illuminating type of LACBED pattern to simulate is one taken from the surface of a strong scatterer, since then the features to be discussed are both prominent and distinct, and one in which the offset Δ is non-zero. Both requirements are satisfied by the Pt[231] pattern, figure 4.2.4. The reason for choosing such a pole is that with $\Delta = 0$, the equations (4.2.24) must necessarily produce a pattern with mirror symmetry about $K_y = 0$. The only way to avoid the effects of Δ for an asymmetric pole is to have no variation of the energy $\sigma^{(j')}$ with K_x. This may be achieved in THEED only by coupling into a completely flat band of the dispersion curve; in RHEED it should also be possible if, for whatever reason, a bulk-like branch-structure is not seen by the electrons. It follows that there must be some correlation between the symmetry of a diffraction pattern taken from a $\Delta \neq 0$ pole, and the degree of periodicity seen by incident electrons.

Figure 4.2.7 shows the first 7 branches of the dispersion surface of the Pt($\bar{1}1\bar{1}$) systematic row, from an 11 beam numerical calculation.

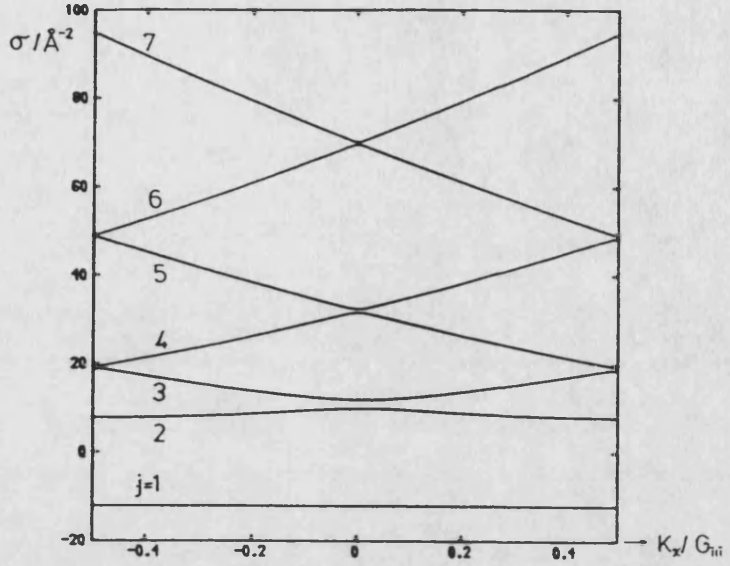

Figure 4.2.7. The first seven branches of the Pt($\bar{1}1\bar{1}$) systematic row dispersion surface at 200kV, generated by an 11-beam dynamical calculation. The 1-d eigenvalues are measured relative to the mean inner potential U'.

This is the same number of beams as used to calculate the strip-width λ in the numerical simulations of §4.2.2. The most notable feature of this figure is that the first branch is extremely flat, and well split off from the other branches. These values of $\sigma^{(j')}(K_x)$ may be inserted numerically and branch-by-branch into (4.2.24), which is then solved for K_y as a function of K_x, using the appropriate value of H for the particular pole. The loci (K_x, K_y) satisfying (4.2.24) are plotted in figure 4.2.8 for the same region close to the Pt[231] pole as simulated before. Apart from the expected absence of the "surface-parallel" ($\bar{1}1\bar{1}$)-type lines, these simulations bear a strong resemblance both to the experimental and theoretical patterns of figure 4.2.3. Each line in figure 4.2.8 is in the same position as in the full dynamical simulation of figure 4.2.3.

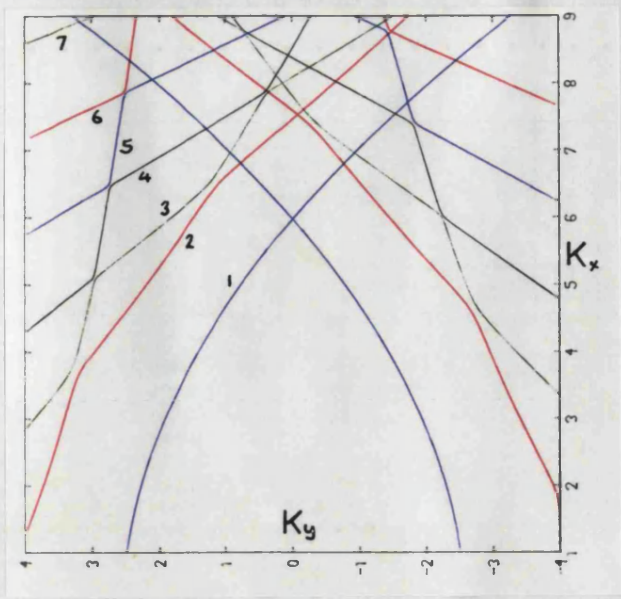

Figure 4.2.8. Branch-by-branch simulation of 200kV Pt[231] LACBED pattern using two-rod theory. Each line is labelled with the branch of the dispersion surface (figure 4.2.7) which produces it. The scale of the simulation is the same as in figure 4.2.3.

The conclusion to be drawn here is clearly that, for a strong scatterer such as Pt, the LACBED diffraction geometry may be understood in terms of a perturbative, two-rod, branch-by-branch analysis.

In particular, it is concluded that the inner, smooth parabolas may be generated entirely from branch 1 contributions; note that this is the only flat band, and the resulting parabolas are the only features symmetrical about $K_y = 0$. In addition, the envelope of the parabolas is seen to be a product of branch 2. This is also a strongly dynamical branch in the Pt($\bar{1}1\bar{1}$) system. It cannot, therefore, be assumed that such envelopes are normal Kikuchi lines, since Kikuchi lines are maps of *plane-wave* dispersion Bragg conditions. Instead, the envelopes are the loci of orientations satisfying the dynamically modified Bragg condition for branch 2. The higher branches become progressively weaker, displaying approximately parabolic dispersion and giving rise to straight lines in the diffraction

pattern at normal Bragg positions. Such features can only arise in any diffraction pattern if the real-space potential is periodic, in which case the reciprocal space is periodic and K_x must be conserved. Thus a qualitative test of the penetration of RHEED electrons is to look for features which rely on periodicity in the x-direction.

How do these arguments become changed for weaker scatterers? Figure 4.2.9 shows the first 7 branches of the GaAs($\bar{2}20$) systematic row dispersion curve, and the corresponding [116] branch-by-branch simulation.

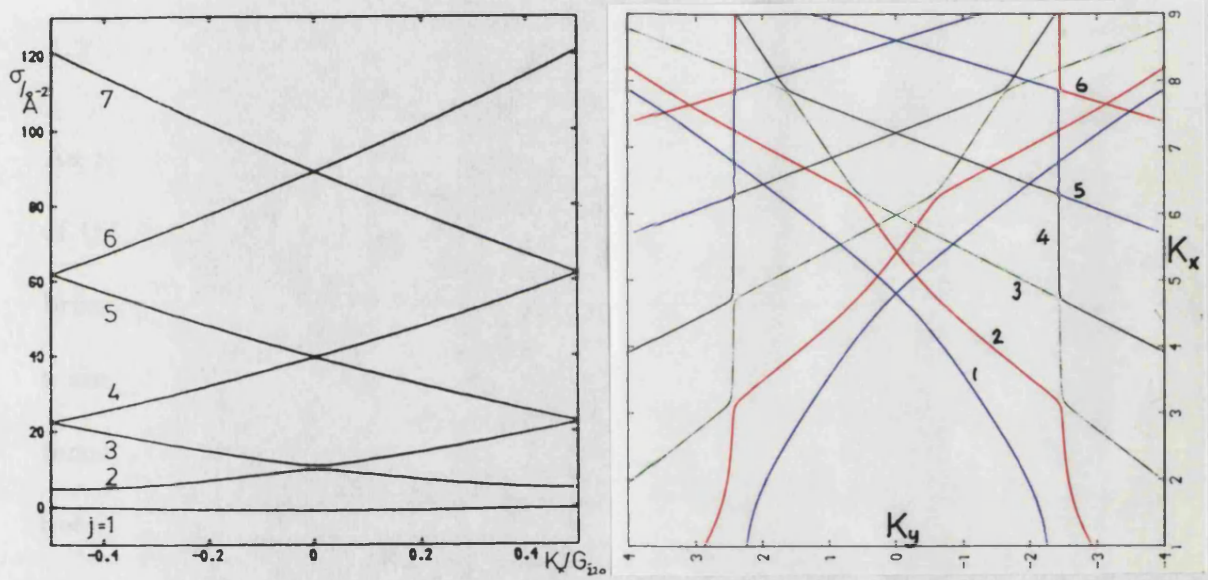

Figure 4.2.9. (a) GaAs($\bar{2}20$) systematic row dispersion surface at 200kV. (b) Branch-by-branch simulation of GaAs[116] LACBED pattern, using (a). This simulation and figure 4.2.4 are to the same scale.

It is clear here that, since the first branch is not quite flat, the inner curve is not quite parabolic, and that apart from the dynamical rearrangement of branches 1 and 2, the whole pattern consists of straight lines, characteristic of a nearly-free electron branch structure. As may be expected, the dynamical effects exhibited by branches 1 and 2 become weaker for materials containing lighter elements.

This result will now be used to suggest a straightforward and quick method of simulating both THEED and RHEED patterns. Before this, it should first be mentioned that the [116] pole on a $(\bar{2}20)$ surface has $\Delta = 0$. Were we to choose a pole with non-zero Δ, the parabolas for medium-strength and weak scatterers would themselves be asymmetric in THEED patterns, though not in the associated RHEED pattern if the x-direction periodicity is lost completely. This is the sort of THEED-RHEED difference which should be used in the investigation of surface-sensitivity in the latter.

4.2.5 Semi-kinematic LACBED simulations

As already mentioned, it is clear from figures 4.2.8 and 4.2.9 that the envelope of the inner parabolas consists of branch 2 contributions. For the higher index branches, the lines produced are approximately in their kinematic positions, so a simple method is suggested for a semi-kinematic simulation of THEED patterns which shows all lines, and is easily corrected for refraction for comparison between THEED and RHEED in §4.3.

Figure 4.2.10 is a series of two-rod, branch-by-branch simulations of the [231] pole LACBED patterns, in which the strength of the scattering potential in the $(\bar{1}1\bar{1})$ systematic row is artificially set to various fractions of the "true" potential for Platinum, U_{Pt}. Thus the first plot (which is the same as figure 4.2.8) simulates the full Pt potential, and the last gives the type of pattern expected from an imagined scatterer 100 times weaker. The dispersion surface produced by this latter potential is virtually free-electron like, so the lines in the simulation are all in their kinematic positions.

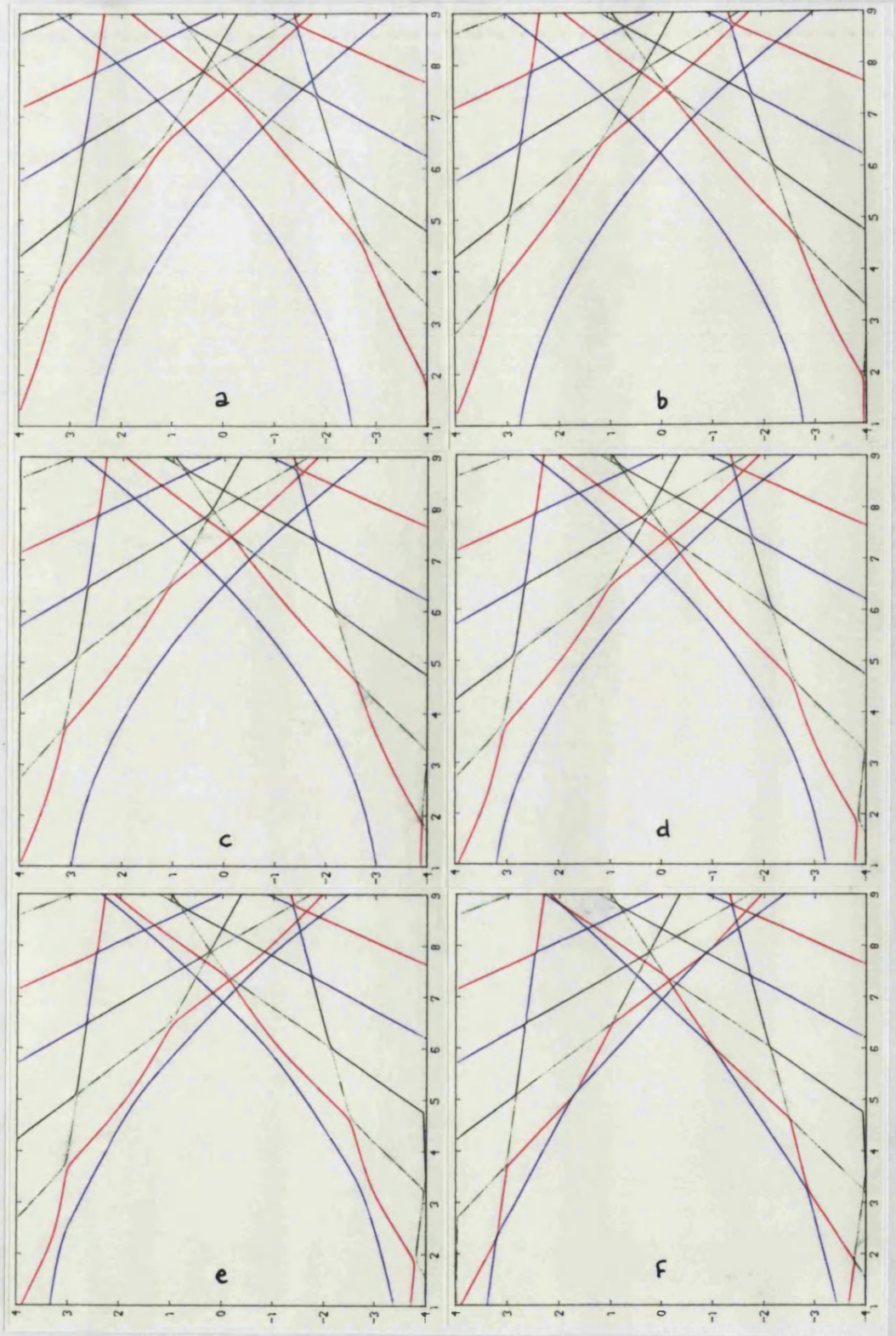

Figure 4.2.10. Series of two-rod, Branch-by-branch simulations of Pt[231] at 200kV, for various fractions c of the true scattering potential U_{Pt}. (a) to (f) correspond to c =1.0, 0.8, 0.6, 0.4, 0.2 and 0.01 respectively.

The points to observe from figure 4.2.10 as the potential is increased are

- ⋆ The position of the branch 1 contribution moves away from the branch 2 envelope, and becomes more parabolic as the potential is increased.
- ⋆ The branch 2 envelope itself changes shape, producing a *different* set of straight-line segments to those seen at "zero" potential.
- ⋆ The other lines remain straight, and approximately in their kinematic positions. The slight adjustment to this at large potentials is that, close to the "surface" where the dynamical effects are strongest, and where two-rod theory is most likely to break down, the lines are shifted slightly. Each then makes a slightly different angle with the surface than at zero potential.

These observations may also be made using the full 2-dimensional LACBED simulations, which show that the surface-parallel Bragg lines $(\overline{n}n\overline{n})$ also remain in approximately the same place (especially for large n), regardless of the strength of the potential. In §4.3, much of the discussion of RHEED patterns will be centred around the similarities and differences with THEED patterns. It is therefore useful to have a simple method of simulation which will prove to be applicable to either geometry. Such a method is suggested by the lack of movement of the high-branch diffraction lines from their kinematic positions. Figure 4.2.11 shows a plot of all diffraction lines in their kinematic positions (which are of course the bisectors of each reciprocal lattice vector in the zero-layer), similar to those drawn by Lehmpfuhl and Dowell (1986) and others, for a [231] pole. The branch 1 contributions to these lines are shown dashed, as they are replaced by smooth parabolas, added in a position corresponding to the eigenvalue $\sigma^{(1)}$ of the Pt$(\overline{1}1\overline{1})$ systematic row. This addition of a dynamical feature is somewhat

artificial, but does help in the indexing of RHEED patterns later. The branch 2 envelopes are not well simulated by these kinematic line diagrams, as can be seen in figure 4.2.10. Instead they consist of the dynamical "hybridisation" of the free-electron Kikuchi envelope.

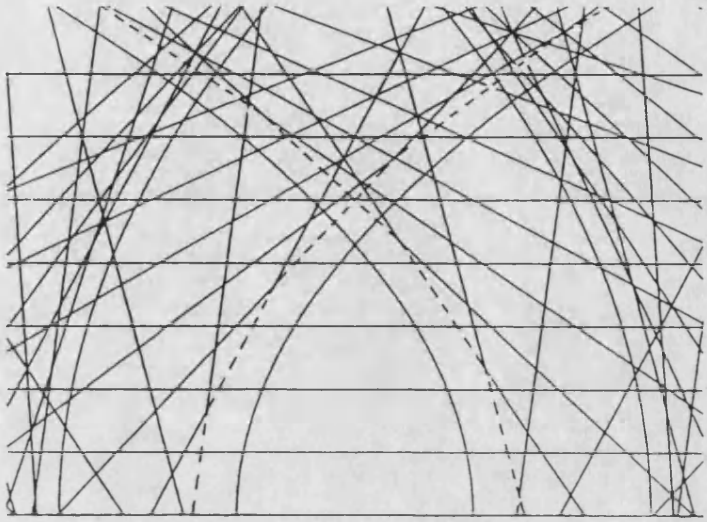

Figure 4.2.11. Semi-kinematic simulation of off-axis 200kV Pt[231] LACBED pattern. See text for details.

In order to apply such a simple simulation to the RHEED case, it is necessary only to correct the K_x coordinate for refraction, via (4.1.4). This correction is a non-uniform one-way stretch, which is considerably easier to implement in a simulation where the lines have an analytic form than in the grey-scaled plots produced from the numerical analysis, where each orientation contributes intensity to a fixed, square region. Since the THEED features best simulated are among those which are easiest to see in a RHEED pattern, and the transformation from THEED to RHEED is so easy, these simulations are used as the first aid in comparing the transmission and reflection pattern geometries in §4.3.

4.2.6 Summary

It has been shown that the ZOLZ geometry of off-axis bright-field LACBED patterns can be understood entirely in terms of the satisfaction of a modified Bragg condition, in which the branch structure of a 1-dimensional systematic row potential plays a crucial rôle. This systematic row potential is itself the transmission analogue of a rod potential in RHEED, so the methods of this section are transferable to the RHEED case. Various simulation techniques have been introduced which illustrate how a LACBED pattern is formed, especially for a strong scatterer (Platinum), where the effects are most clear.

4.3 ANALYSIS OF RHEED PATTERNS

This section begins with the application of semi-kinematic fits to 200kV RHEED patterns. It is found that these transmission-based simulations fit the reflection patterns well. On the basis of this, the main conclusions of the chapter are drawn. From then on, attention will be confined to RHEED itself, in an attempt to justify the use of the transmission arguments of §4.2, and to further understand the nature of the parabolic features, with reference to their surface-sensitivity and whether or not they are resonant. Finally, it is suggested that it may be possible to use the position of a parabola to determine surface Debye-Waller factors.

4.3.1 A semi-kinematic fit to experiment

The similarity of the off-axis THEED and RHEED pattern geometries may be established using the semi-kinematic plots introduced in §4.2.5. It is found that, with the application of a simple correction for the refractive mean inner potential

$\overline{U}$, these simulations fit the RHEED patterns rather well. Since all the electrons contributing to a RHEED pattern have emerged from orientations inside the crystal, the 2-dimensional orientations outside (where the pattern is observed) must be transformed via [see (4.1.4)]

$$K_{yo} = K_{yi} \tag{4.3.1}$$

and

$$K_{xo} = \sqrt{K_{xi}^2 - |\overline{U}|}, \tag{4.3.2}$$

where the subscripts $_o$ and $_i$ again indicate a wavenumber outside or inside the crystal respectively. From (4.1.3) and (3.1.2) it is seen that $\overline{U}$ is given by

$$\overline{U} = U_0 = \sum_{\kappa} u_{\kappa}(0), \tag{4.3.3}$$

where u_κ is the atomic form factor of the atom κ in the unit cell. $\overline{U}$ could therefore be deduced simply by adding the appropriate atomic form factors. Unfortunately, the "straight through" form factors are the least reliable of all in the calculations of Doyle and Turner (1968) and others; in practice it is better to fit a value of $\overline{U}$ from the refracted positions of known features. The best lines to use for a $\overline{U}$ fit are those associated with reciprocal lattice vectors **G** whose G_y component is zero; these are the "surface-parallel Bragg lines", which for a $(\overline{1}1\overline{1})$ surface are just $(\overline{n}n\overline{n})$, with n a positive integer. Note that some of these surface-parallel reflections will have K_{xi} too small for any reflected electrons to escape the surface.

A value of $\overline{U}$ has been fitted for the Pt[231] pattern of figure 4.1.1 by considering the position of the 7 surface-parallel lines $(\overline{3}3\overline{3})$ to $(\overline{9}9\overline{9})$. Let the distance

between the $(\overline{3}3\overline{3})$ and the $(\overline{n}n\overline{n})$ line be K_n. Then, since the Bragg condition for reflection by $G_{\overline{n}n\overline{n}}$ is $K_{xi} = -G_{\overline{n}n\overline{n}}/2$, it follows from (4.3.2) that

$$\left[\frac{1}{4}G^2_{\overline{n}n\overline{n}} - |\overline{U}|\right]^{\frac{1}{2}} - \left[\frac{1}{4}G^2_{\overline{3}3\overline{3}} - |\overline{U}|\right]^{\frac{1}{2}} = K_n. \qquad (4.3.4)$$

$\overline{U}$ cannot be evaluated by direct solution of this equation, but may be found, for example, by minimisation of the error function

$$\sum_n [K_n(\text{calculated}) - K_n(\text{measured})]^2$$

as a function of $\overline{U}$. It is found from figure 4.1.1 that at 200kV, the mean inner potential for Pt is $\overline{U} = -11.0 \pm 0.2\text{Å}^{-2}$. This may be converted to volts by application of (2.2.8), to give $\overline{V} = -30.2 \pm 0.6\text{V}$, in good agreement with the value calculated by Radi (1970) [$\overline{V} = -30.0\text{V}$], and used by Marten and Meyer-Ehmsen (1985) in their study of the Pt(111) surface. Note that the Doyle-Turner calculations give $\overline{U} = -12.1\text{Å}^{-2}$.

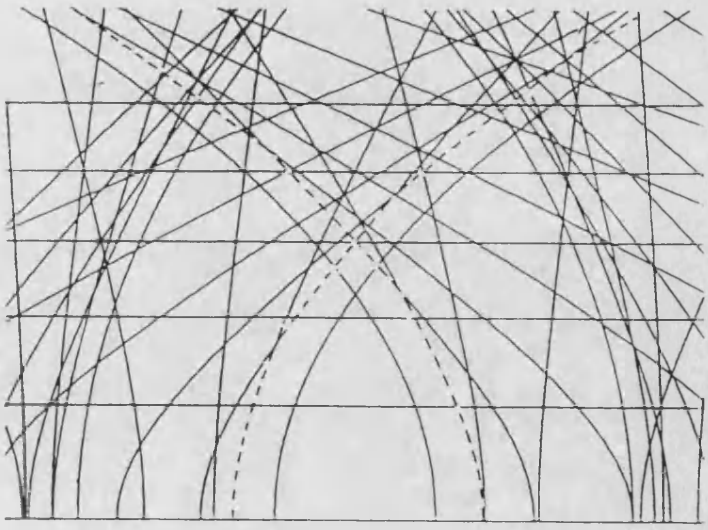

Figure 4.3.1. Semi-kinematic simulation of 200kV Pt[231] RHEED pattern. This is the plot of figure 4.2.11 with a refractive correction applied. See text for details.

Figure 4.3.1 is a semi-kinematic simulation of the Pt[123] CB-RHEED pattern figure 4.1.1, with the identical parameters as for the THEED simulation in figure 4.2.11, except for the inclusion of a refraction correction, $\overline{U} = -11\text{Å}^{-2}$. The kinematic "branch 1" contribution is again dashed, and replaced by parabolas with the *same* bound-state eigenvalue as in transmission. Note that refraction causes some of the Bragg lines to be bent close to the surface; however, these lines are still the analogue of the straight lines in the transmission case. This simulation provides as good a fit of the experimental pattern (especially on the negative, where more Kikuchi bands are detectable) as does the THEED simulation of the THEED patterns. A similar result is found at all poles in all the other materials investigated, at an accelerating voltage of 200kV (Wright 1989).

4.3.2 Conclusions

The main conclusion of this chapter may now be drawn. It is evident that 200kV RHEED patterns exhibit both straight lines and asymmetries about $K_y = 0$. Neither of these features is possible unless the electrons producing them have penetrated far enough into the crystal to see a bulk-like potential, since both are a product of K_x being conserved to within a reciprocal lattice vector. The similarity between the lines produced by 1-dimensional dispersion surface branches $j > 1$ in THEED and those in RHEED suggest that any information from the outermost, surface layer will be averaged in these features with information from the selvedge and bulk layers beneath. As will be seen later, the number of layers over which this averaging occurs, and the weighting which should be given to the contribution from each layer are both rather difficult to quantify, so it is not

reasonable to expect these features to yield useful surface information. The only way in which this information *could* be extracted in principle is via a detailed simulation of diffracted intensity, in which case high-voltage RHEED would offer no advantage, and possibly some disadvantages, over LEED and other surface techniques.

These same conclusions cannot be made regarding the parabolas from strongly scattering surfaces. This is because in the transmission case, the deep bound states are associated with a flat band in the dispersion surface. With a flat band, K_x conservation does not affect the *position* of diffracted features. Thus it is impossible to tell from the arguments given so far whether K_x is being conserved, and therefore equally impossible to tell whether the parabolas come solely from the surface or from a mixture of surface and bulk. Both a single bound state at the surface and a bulk flat branch with the same eigenvalue would give the same pattern geometry, As an aside to which we return in §4.3.6, it would seem that the parabolas in RHEED patterns are in a position slightly further from their envelopes than in THEED, consistent with coupling into a slightly less deeply bound state. The existence of any difference at all would of course imply that the surface has some effect on these features. What the above does tell us about the parabolas is that they *are* associated with coupling into bound states, which may or may not resemble bulk Bloch states. The fact that the parabola-envelope gap is almost the same in RHEED and THEED disproves the suggestion (see eg Peng and Cowley 1987) that both are parabolas separated by an amount dependent upon $\overline{U}$.

The next part of this chapter is now given to a study of some of the ways in which

features (particularly parabolas) could be different in RHEED. The study will be based upon two-rod theory. In the process, the similarities between THEED and RHEED, and the conclusions drawn from these similarities, will be put on a firmer footing.

4.3.3 Two-rod theory in RHEED

The two-rod equations in RHEED for the rods $G_y = 0$ and $G_y = H$ are those given in (4.1.9) and (4.1.10). With the energies $K_x^2(G_y)$ expanded as in (2.3.19), they are

$$\left[-\frac{d^2}{dx^2} + U_0(x) - K_x^2\right]\psi_0 \;=\; -U_{-H}\psi_H \tag{4.3.5}$$

and

$$\left[-\frac{d^2}{dx^2} + U_0(x) - (K_x^2 - 2K_yH - H^2)\right]\psi_H \;=\; -U_H\psi_0, \tag{4.3.6}$$

These are second order equations, and therefore describe a scattering problem. The formal solutions will be written in terms of Green's functions, which are particularly suited to the perturbation treatment of the inter-rod transitions which will follow. The unperturbed Hamiltonian will be taken as

$$\mathcal{H}^\circ \;=\; -\frac{d^2}{dx^2} + U_0(x), \tag{4.3.7}$$

where the rod potential $U_0(x)$ (see figure 4.1.2) is *not* perfectly periodic, due to the presence of the surface. The Green's functions are defined as (eg Economou 1983)

$$\mathcal{G}_0 \;=\; \left[K_x^2 - \mathcal{H}^\circ\right]^{-1} \tag{4.3.8}$$

and

$$\mathcal{G}_H = \left[(K_x^2 - 2K_yH - H^2) - \mathcal{H}^\circ\right]^{-1}. \qquad (4.3.9)$$

These Green's functions may be thought of as electronic wavefunction propagators on rods 0 and H respectively. As with the transmission perturbation theory, however, the states of propagation are always those of the unperturbed Hamiltonian $\mathcal{H}^\circ$. The only difference between the Green's functions $\mathcal{G}_0$ and $\mathcal{G}_H$ is that they are associated with the propagation of electrons at different *energies*.

The states of a single rod potential

It is instructive to look first at the form of the basis states, which are of course the eigenstates of $\mathcal{H}^\circ$. The states of interest are those which satisfy (4.3.5) and (4.3.6) with the right-hand side set to zero. The energies of these states are K_x^2 (which is positive since it represents the energy of the incident electrons) and $K_x^2 - 2K_yH - H^2$ which may in principle take any value.

Let the initial state on rod 0, with energy K_x^2 determined by the incident beam, be ψ_{00}. For the moment the potential $U_0(x)$ is taken as real. Even without the presence of atomic modulation, the step potential of height $\overline{U}$ will cause ψ_{00} to contain both transmitted and reflected components. Perhaps more significantly, the incoming wave (with $U_0(x)$ real) will see the periodicity of the atomic wells and will undergo diffraction. ψ_{00} will therefore produce, for example, surface-parallel Bragg lines. As in the THEED case, ψ_{00} should be expanded as a linear combination of many terms, but for ease will be represented by the single plane wave, without a reflected component,

$$\psi_{00} = \exp(+iK_xx) \equiv |K_x\rangle. \qquad (4.3.10)$$

Now, in transmission, the inclusion of absorption is largely a matter of choice, yet it is necessary that it be included in any meaningful description of RHEED, at least to some extent. The fact that only one surface of the crystal provides a boundary condition in a system governed by a second order equation may be justified on the grounds that no electrons ever reach the "back" surface of the specimen due to absorption. Since in RHEED the main direction of interest is the surface-normal (x) direction, a given U' will be relatively large compared with the incident kinetic energy K_x^2, so absorption is likely to play a significant rôle.

If absorption is included in the zeroth rod potential, ψ_{00} must still match to a real energy outside the crystal, so its energy must remain real inside. However, it may pick up an imaginary wavenumber, which gives rise to absorption, and therefore to finite penetration of the incident beam.

At the Bragg condition for surface-parallel lines the penetration depth of incident electrons will be affected both by anomalous absorption contributions, and by the size of the bandgap, governed by U_{G_x}. However, by solving the many-beam equations "backwards", for K_x given the energy σ, Wright (1989) has shown that the penetration depth is basically governed by the *mean* absorption term $\overline{U'}$. [At large G_x, $\overline{U'}$ exceeds both U'_{G_x} and U_{G_x} and is therefore the dominant factor.] To see how $\overline{U'}$ causes absorption, extend (4.1.4) by writing

$$K_{xi} = \sqrt{K_{xo}^2 + |\overline{U}| + i|\overline{U'}|} \approx \chi \left(1 + \frac{i|\overline{U'}|}{2\chi^2}\right), \qquad (4.3.11)$$

where $i|\overline{U'}|$ has been assumed smaller than the other terms, and where $\chi = \sqrt{K_{xo}^2 + |\overline{U}|}$ is the propagating part of the wavenumber K_{xi} inside the crystal.

From (4.3.11) the imaginary, absorptive, part of this wavenumber is

$$K'_{zi} \approx \frac{|\overline{U'}|}{2\chi} \equiv \frac{1}{\delta}, \tag{4.3.12}$$

where the defined quantity δ is the penetration depth. As a useful guide, consider the penetration of incident plane waves at an orientation corresponding to the position of the nth surface-parallel Bragg line. At the Bragg condition, $|\chi| = |\frac{n}{2}G_x|$, where $G_x = 2\pi/d$, and d is the spacing of the surface planes. The number of planes penetrated is then given by

$$m = \frac{\delta}{d} \approx \frac{2\pi n}{d^2|\overline{U'}|}. \tag{4.3.13}$$

That is, the number of layers penetrated is proportional to the angle of incidence (through n) and inversely proportional to the mean absorptive potential $\overline{U'}$. This penetration of an incident plane wave does not necessarily determine the surface sensitivity of a RHEED feature, which may arise through coupling into other states which are not absorbed in a similar way. However, as will be shown, the penetration depth of the incident beam is a contributory factor to this sensitivity. Ideally, of course, $m \approx 1$. Unfortunately, it is rather difficult in practice to determine accurate values of $|\overline{U'}|$. The mean absorption is the least well modelled using thermal diffuse scattering calculations (eg Bird and King 1990), and may be difficult to predict by other means. On the measurement side, Howie, Milne and Walls (1985) have determined the penetration depth of 100kV electrons at various incidence angles to a GaAs(220) surface, using classical dielectric theory to fit the surface and bulk plasmon peaks found using reflection electron energy-loss spectroscopy (REELS). Similar work has been

reported by Wang (1988), and produces values of penetration depth consistent with the crude analysis which follows:

Let us suppose that at 200kV, $U = 10U'$. In the negative used to produce figure 4.1.1a, the visible surface-parallel Bragg lines are for $3 \leq n \leq 9$. At Pt($\bar{1}1\bar{1}$), $|\overline{U}| = 11\text{Å}^{-2}$ and $d = 2.26\text{Å}$, so (4.3.13) gives $3.3 \leq m \leq 10.0$ over this range of n. It is generally accepted (eg Humphreys and Hirsch 1968) that U' scales with energy as γ/β, where γ is the ratio of the incident electron mass to its rest mass, and β is the ratio of the incident electron velocity to that of light. This scaling rule suggests that at a typical RHEED camera voltage of 20kV, we should expect $1.7 \leq m \leq 5.2$ for the same range of orientations as used above. A similar analysis for a lighter material, GaAs, using $2 \leq n \leq 6$ (see figure 4.1.1b) gives approximate penetration $5 \leq m \leq 16$ at 200kV, reducing to $3 \leq m \leq 8$ at 20kV.

The other states of $U_0(x)$ of interest are of course the deeply bound states. These are inaccessible to ψ_{00} by virtue of its high energy. However, they may be accessed by means of inter-rod transitions, via the Green's function $\mathcal{G}_H$ of (4.3.9). These states will clearly look like tight-binding Bloch states well into the bulk of a strong scatterer such as Platinum, and must be matched to a decaying wave in the vacuum. At the surface, additional states are allowed ("Tamm" states - see eg Appelbaum 1975) which are truly localised to the surface and which reside in the bandgaps of the bulk dispersion surface. For Pt($\bar{1}1\bar{1}$), there is very little overlap between the deepest bound states of neighbouring wells. Thus the outermost well would have to be considerably different from the others for its energy to be far from that in the band.

If absorption is "switched on" for these states, it is likely that they will pick up a complex energy, though it is not obvious that they will in any sense be "absorbed". That is, these states will continue to exist as perfectly good states into which an electron may couple, regardless of absorption. This point is returned to later. First though, it is necessary to add a second rod, and derive the two-rod solution for RHEED, which will contain the matrix element which *does* control the surface sensitivity of RHEED features.

Coupling between two rods

The right-hand sides of (4.3.5) and (4.3.6) are now re-introduced to produce inter-rod transitions. The Green's functions (4.3.8) and (4.3.9) are substituted in these two-rod equations to provide the formal solution to the problem. The one addition which is made is to insert the initial wavefunction ψ_{00}. The resulting solutions on each rod are

$$\psi_0 = \psi_{00} + \mathcal{G}_0 U_{-H} \psi_H \tag{4.3.14}$$

and

$$\psi_H = \mathcal{G}_H U_H \psi_0. \tag{4.3.15}$$

The second of these may be substituted into the first to give the Lippman-Schwinger equation for the wavefunction on rod 0:

$$\psi_0 = \psi_{00} + \mathcal{G}_0 U_{-H} \mathcal{G}_H U_H \psi_0. \tag{4.3.16}$$

This equation states that the contributions to the wavefunction on rod 0 are due to incident electrons, plus electrons which have at some stage been on rod 0, been scattered onto H, propagated along H, and scattered back to 0. Iteration

of this equation leads to a perturbation expansion for ψ_0, namely

$$\psi_0 = \psi_{00} + \mathcal{G}_0 U_{-H} \mathcal{G}_H U_H \psi_{00} + \cdots . \tag{4.3.17}$$

Truncated at the second term, this is the precise analogue to the second order transmission amplitude derived in §4.2. Since the scattering has been monitored from the incident beam, then into and out of another state, this second order term is the first which will display the features of interest. To make clearer the analogy between the scattering perturbation expressions and those of §4.2, it is necessary to expand the Green's functions in terms of the eigenstates φ of the unperturbed Hamiltonian $\mathcal{H}^\circ$. We therefore write the G_yth Green's function as (Economou 1983)

$$\mathcal{G}_{G_y} = \sum_p \frac{|\varphi_p\rangle\langle\varphi_p|}{s'_p - s} + \int_0^\infty ds' \, \frac{|\varphi(s')\rangle\langle\varphi(s')|}{s' - s + i\eta}, \tag{4.3.18}$$

where the (1-dimensional) energy variable s is given by

$$s = K_x^2 - 2K_y G_y - G_y^2. \tag{4.3.19}$$

The zero energy point $s = 0$ is of course at vacuum zero. Hence the integral in (4.3.18) is over the continuum of states with energy $s' > 0$. The small imaginary quantity $i\eta$ is included in the denominator to facilitate the choice of direction ($+K_x$ or $-K_x$) of these waves. The summation is over the bound states of $U_0(x)$.

This expansion of the Green's function is now used in the formal solution, (4.3.17). ψ_{00} will be restricted to the plane wave (4.3.10). Following McRae (1979) and §4.2, we pick out a single state from $\mathcal{G}_H$ for analysis. This is a bound state τ with eigenvalue σ. The expression (4.3.17) for the wavefunction on rod

0 then becomes

$$\psi_0 \approx |K_x\rangle + \mathcal{G}_0 U_{-H} \frac{|\tau\rangle\langle\tau|U_H|K_x\rangle}{(K_x^2 - 2K_y H - H^2 - \sigma)}. \qquad (4.3.20)$$

To construct the equivalent of the THEED amplitude (4.2.23), we assume that the wavefunction back on rod 0 is again a plane wave. In terms of energy conservation, both $|-K_x\rangle$ and $|K_x\rangle$ are accessible plane-wave states, as in THEED. Since in this case *reflected* waves are of interest, the former is chosen. With attention limited to plane waves, $\mathcal{G}_0$ is just a free-particle propagator, so

$$\psi_0 \approx |K_x\rangle + \frac{|-K_x\rangle}{2iK_x} \cdot \frac{\langle -K_x|U_{-H}|\tau\rangle\langle\tau|U_H|K_x\rangle}{(K_x^2 - 2K_y H - H^2 - \sigma)}. \qquad (4.3.21)$$

Not surprisingly, this is almost identical to the plane-wave version of the THEED result of §4.2, (4.2.23). The important similarity is that the denominator describes exactly the same modified Bragg condition, which in this case, with the single eigenvalue σ taken to be constant, gives rise to smooth parabolas. In RHEED, however, the choice of constant σ need not imply a flat *branch*, as a single bound state (such as a Tamm state) would produce the same result. Equation (4.3.21) also shows that if all the terms were subject to K_x conservation, the whole RHEED geometry would be the same as in the THEED case. This justifies the earlier arguments of the chapter, and will be returned to in a discussion of resonance mechanisms in §4.3.4.

Surface sensitivity of the parabolas

The matrix element $\langle\tau|U_H|K_x\rangle$ is of course an integral over all x. In transmission, ignoring absorption, the integrand is finite and periodic for all x, so the integral limits may be reduced to cover a single layer spacing d. In RHEED,

various features render the limits of this integral finite. In the vacuum, the exponential tail of the bound state $|\tau\rangle$ makes the integrand small. Inside the crystal, absorption must be applied to the initial wavefunction ψ_{00}, represented here by $|K_x\rangle$. This causes exponential decay into the specimen, and therefore reduces the range of x making a significant contribution to the matrix element.

To determine the surface sensitivity of the parabolas in CB-RHEED patterns, it is also necessary to know the spatial extent of the bound state $|\tau\rangle$. As mentioned before, if Tamm states are ignored, the bound states of $U_0(x)$ will remain accessible states throughout the bulk, even when absorption is included. In this scenario the limiting factor on surface sensitivity must be the spatial extent of $|K_x\rangle$, in which case parabolas in 200kV patterns cannot be considered to come from the surface alone (see §4.3.3).

By contrast, a Tamm state is truly localised at a surface. If only a Tamm state were excited, its own spatial extent, and *not* that of $|K_x\rangle$ would be the limiting factor. However, for the Pt($\bar{1}1\bar{1}$) surface, the eigenvalue of a bulk state and a Tamm state would have to be very close unless the outermost well was significantly different from the bulk wells. Thus one could not be excited without the other, and both would produce parabolas at the same place. §4.3.5 contains a brief study of one feature which could cause the outermost well to differ. However, figure 4.1.1 only displays a single parabola, so the conclusion must be drawn that at 200kV the parabolas contain a mixture of surface and bulk information. Deconvolving this mixture would be extremely difficult, since it would require knowledge of $\overline{U'}$, and a fitting procedure over all possible Tamm state contributions. On the other hand, low-voltage RHEED, in which the

incident beam penetration may be only a few monolayers, especially for strongly scattering materials, should produce parabolas which come from coupling into the surface layers alone.

4.3.4 Resonance, enhancement and momentum conservation

It is now time to comment upon whether the parabolas seen in RHEED patterns are "resonant", as seems to be assumed (without explanation) in most of the published papers dealing with the phenomenon. Resonance is of course a common feature in many branches of physics, and its occurrence in a given system may be explained in any number of equivalent descriptions. For example, resonance is associated with an extremal impedance of a system, with the excitation of a pole of the system's governing equations, or as a state in which some phase difference becomes zero. The term resonance should not automatically be applied every time a system produces a strong response, though such a response is frequently a feature of resonance.

For the application studied here, the excitation of a pole of the system has already been shown to give nothing more than a modified Bragg condition. Since the specimen in considered infinite in the z direction, a surface-parallel wave in perturbation will have a divergent path length when this condition is satisfied. This is similar to divergent amplitudes predicted in transmission kinematic theory for an infinitely thick specimen. It is not clear from a perturbation theory written in projection how to express the strength of diffraction expected from electrons with long path lengths, though the fact that the σ for bound states are allowed to be complex prevents complete divergence.

All this suggests that a modified Bragg condition *is* a resonance, but not a particularly special one. However, the analysis *does* suggest that there will be an enhancement of amplitude, contained in the *residue* of the pole for coupling into a bound state. This residue contains the matrix elements discussed in §4.3.3. The deepest bound state of a one dimensional potential well will be approximately as sketched in figure 4.1.2, with one antinode at each atomic position. Thus, independent of the number of wells excited, the wavefunction $|\tau(x)\rangle$ will be at its strongest at the same positions as the potential $U_{\pm H}(x)$. The matrix elements $\langle K_x|U_{-H}|\tau\rangle$ and $\langle\tau|U_H|K_x\rangle$ will therefore be larger than for plane-waves and for other states not centred on the atomic positions.

This effect is also observed in HOLZ reflections in transmission. In that case the 2-d ZOLZ branch structure dictates the position and strength of the HOLZ lines; if the states of a given branch and the relevant scattering potential both have a large amplitude at the same positions, the HOLZ amplitudes will be enhanced with respect to a plane-wave transition. This enhancement, known as a "concentration" factor, is typically 2-3 for a 2-dimensional 1*s* state (see Baker 1982, Vincent, Bird and Steeds 1984b). Given that the amplitude diffracted into and out of rod H is second order in these matrix elements, a similar amount of enhancement in this 1-d case could produce intensities in the parabola perhaps 10 to 100 times larger than in surrounding, plane-wave, features. This is precisely the sort of intensity anomaly reported by Marten and Meyer-Ehmsen (1985) and others. It should be concluded that "enhancement" is perhaps a better term to describe the behaviour of surface-parallel electrons than is "resonance".

Unfortunately, it is evident from figure 4.1.1 that the parabolas will *not* neces-

sarily be anomalously strong diffraction features in a RHEED pattern. Indeed the portions of parabolas between the surface-parallel Bragg lines are all rather weak and diffuse at 200kV; this is in agreement with the experimental and computational results of Bleloch (1989) taken from GaAs at 100kV. This result may be understood with reference to the construction sketched in figure 4.3.2. This zero-potential picture is more useful than might at first seem likely.

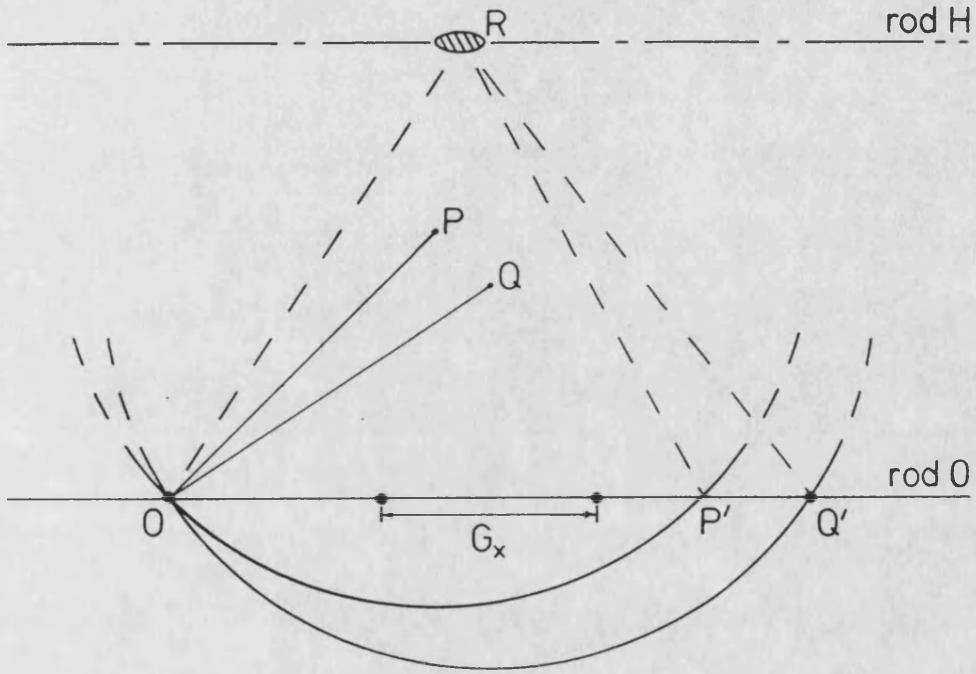

Figure 4.3.2. Construction used to indicate which parts of a parabola will give strong diffraction if K_x is conserved. See text for details.

Figure 4.3.2 shows two incident orientations P and Q which lie on a parabola. In the zero-potential limit, this means that their Ewald spheres are tangential to rod H; in reality this is not the case, but the H rod part of the construction is not necessary to the argument; instead we apply the algebraic condition that at P and Q the modified Bragg condition for scattering from $|K_x\rangle$ on 0 to $|\tau\rangle$ on H is exactly satisfied. The state coupled into on rod H is nominally labelled by

the position R, though in fact it may be completely delocalised along the rod. Note that the geometry is almost identical to that of the three-beam diffraction studied in Chapter 3, except that two of the transitions are governed by modified Bragg conditions; the situation may therefore be thought of in terms of "three-state" diffraction. As just discussed, the amplitude of the transition OR is likely to be anomalously large.

Also shown in figure 4.3.2 are the positions of reciprocal lattice points along rod 0, as would be seen by an electron penetrating into the bulk of the crystal. The states of interest on rod 0 are well approximated by the plane waves $|K_x\rangle$ and $|-K_x\rangle$; these high-energy states are likely to penetrate some distance into the crystal, and must therefore obey some degree of momentum conservation. In addition, energy conservation requires that the final state sits at the intersection of the Ewald circle and rod 0. As a consequence, electrons incident at orientations such as P, whose K_x component is away from a G_x Bragg condition, may scatter strongly onto rod H but will then only have a route to the point of observation P' (either OP' or RP') associated with a large deviation parameter on rod 0. This means that the intensity at P' will be rather weak, as observed, and that a significant contribution to this intensity may come from electrons whose momentum has been shifted by inelastic or diffuse scattering mechanisms, so that the other Bragg conditions become satisfied (see for example Peng and Cowley 1988).

The orientation Q in figure 4.3.2 represents the intersection of a parabola and a surface-parallel Bragg line. At orientations such as this, all three Bragg-type conditions are satisfied. Intensity therefore reaches Q' not only via the

normal Bragg transition OQ', but also via the anomalously strong two-path route OR, RQ'. The intensity around these regions will therefore be large, as is observed at these enhancement orientations in high-voltage RHEED patterns. [In addition, three-beam effects are likely to produce an anomaly in the *shape* of the intensity distribution in these regions.]

All this argument may be put on a slightly firmer footing by comparing the second order amplitudes in transmission (4.2.23) and reflection (4.3.21). In both, the denominators are the same, so the geometry predicted by each is the same. However, in the latter, the final state is $|-K_x\rangle$. If K_x conservation *is* imposed, then the difference in the momentum of the initial and final states for strong diffraction must be

$$-K_x = K_x + G_x. \tag{4.3.22}$$

In other words, the incident wave must be at the Bragg condition for a surface-parallel Bragg line. If K_x conservation is not necessary, this condition will be relaxed.

Of course, the degree of smearing of the reciprocal lattice points along rod 0 varies reciprocally with the penetration depth of the electrons. The inference of the above argument must therefore be that at lower incident energies, with less penetration, K_x conservation is at least partially relaxed, so the transitions back from the bound state on rod H will be more strongly excited. It is therefore predicted that the parabolas in a Pt[231] RHEED pattern taken at 20kV, say, will be much brighter between the surface-parallel lines than at 200kV. This extra bright region should appear as a lengthening of the enhancement region

along the parabola, but not across it. In addition, relaxation of K_x conservation on rod 0 will smear out the surface-parallel lines themselves. Although only a few 1-dimensional rocking curves are given, the results of Marten and Meyer-Ehmsen (1985) show strong parabolas at 20kV, at all orientations.

4.3.5 Surface Debye-Waller factors

Much of this chapter has been concerned with proving that high-voltage RHEED patterns are unlikely to contain much information which is not averaged with several layers of bulk material below the surface. However, there does appear to be one geometrical difference between THEED and RHEED patterns taken from Pt[231] at 200kV which cannot be accounted for by a refractive correction. It is found that the separation of a parabola from its envelope is smaller in RHEED than in THEED, consistent with coupling into a less bound state. This section contains a brief outline of one possible cause of such a shift.

Unfortunately, many of the Bragg lines which are of most use in deducing the exact position of features are hard to pick out in the LACBED pattern from Pt[231] in figure 4.2.1. Thus it is necessary to use a semi-kinematic fit to aid the eye. In addition, LACBED patterns are taken from rather large regions of a specimen, and are therefore susceptible to distortions. All of this means that the magnitude of the shift is difficult to quantify. The effect is seen most easily at the point where the $n = 1$ parabolas from $+H$ and $-H$ cross. This is always at $K_y = 0$, and at a K_x coordinate given by [see (4.1.8)]

$$K_{xo}^2(\text{crossover}) - H^2 = \sigma, \tag{4.3.23}$$

where the bound state energy σ is relative to the vacuum. Although it is difficult

to determine the exact value of K_{xo} at this crossover, it does appear that there is at least some shift between THEED and RHEED patterns. While the position of the parabolas in the former is well simulated using a systematic row Bloch-wave calculation, with $\sigma_T = -23.1\text{Å}^{-2}$, the RHEED parabolas are found to fit a value $\sigma_R \approx -20 \pm 2\text{Å}^{-2}$.

Now, the crude analysis of §4.3.3 gives that the penetration at crossover for Pt[231] is approximately 3-4 monolayers. Thus any difference between THEED and RHEED caused by the surface will be averaged with at least one or two layers beneath. As a consequence, the estimated difference between σ_T and σ_R may be rather large. As a preliminary source of investigation, the transmission many-beam equations have been solved numerically for a somewhat artificial systematic row, in which features of the whole row are varied to simulate the effect of a variation in a single atomic potential. It is found that absorption and simple surface relaxation have virtually no effect on $\sigma^{(1)}$. Bleloch (1989) has shown that the termination of $U_0(x)$ with different exponential tails also has little effect. One variation which does produce some difference, however, is in the mean squared vibrational amplitude, or Debye-Waller figure.

The outermost atomic layer of a crystal may be expected to be less bound to its neighbour than is a typical bulk layer surrounded by two neighbours. Consequently, it is free to vibrate about its equilibrium position with greater amplitude. This will smear out the sharp variation in the atomic potential of this surface layer, making the potential well more shallow, and hence the bound state less bound. The LEED experiments of Lyon and Somorjai (1966) and Morabito, Steiger and Somorjai (1968) suggests that for transition metals at

room temperature, the root mean squared displacement at the surface should be approximately twice that of the bulk. For Pt($\bar{1}1\bar{1}$), this would produce a reduction in $\sigma^{(1)}$ of some 2Å^{-2}. Although this may not be as large a reduction as needed because of the averaging with non-surface layers, this is the only mechanism tried so far which could in principle shift the parabolas by such a large amount. It is hoped that further investigation, and more careful measurement of the position of the parabolas, will lead to a clarification of this situation.

4.4 SUMMARY

In this chapter, 200kV RHEED has been shown to be remarkably similar to off-axis THEED. It must be inferred that genuine surface studies at such voltages will be rather difficult using RHEED. Apart from a refraction correction due to the mean inner potential $\overline{U}$, the geometry of the two types of pattern is virtually identical. In terms of this geometry, both are well explained using two-rod theory, which enables us to explain the position of most diffracted features as contributions from different branches j of a 1-dimensional, systematic row (or rod) dispersion curve. In both geometries the incident electron energy K_x^2, and the surface-parallel momentum K_y are conserved quantities. The observed similarity between off-axis THEED and RHEED patterns indicates that for $j > 1$, the RHEED electrons are penetrating far enough into the crystal to see a bulk-like branch structure. This argument is ambiguous as to the depth of crystal contributing to the branch 1 smooth parabolas in RHEED patterns.

Although some suggestion has been made as to the *probable* solution to this problem, there is room for further work. A test of the model given will be the

appearance or otherwise of bright portions of parabolas between surface-parallel Bragg lines at lower voltages. It will also be an advantage for future work to use genuine RHEED "black-box" calculations for full a numerical back-up to approximations. In this chapter, the only numerical back-up is for the transmission study in §4.2. Such a numerical calculation could then be compared with a computation of the two-rod perturbation intensity, from (4.3.21). It would then be more reasonable to compare intensities as well as line geometry.

Finally, it should be said that the conclusions reached in this chapter all refer to high-voltage RHEED from perfect surfaces. It does not follow that the technique will be of little use in the study of adsorbates, surface steps and so on. Neither does it follow that the associated techniques of REM and REELS are not capable of producing surface information (see eg Wang and Egerton 1988 and Wang and Cowley 1988), though care should be taken with these when they are used in conjunction with RHEED at microscope voltages.

Chapter 5

CONCLUSION

The content of this thesis is two specific examples in which perturbation theory has been used to extract information from HEED patterns. In each case it has been all or part of the scattering potential U which has been the perturbation term in the Hamiltonian. For this to be a useful approach a certain amount of selection must occur, particularly in terms of the experimental geometry used. It is generally accepted that zone-axis diffraction is sufficiently strong always to warrant full dynamical theory for its explanation. In the two examples presented here, off-axis patterns have been studied, with some success.

There can be little doubt that in these specific examples a perturbative expansion of the electron wavefunction has lead to a quicker and better understanding of the physical processes occurring, and of the best way in which useful information may be extracted from the wavefunction, than was possible using numerical, fully dynamical techniques. It is equally apparent that confidence in the approximate solutions is much easier to achieve if such numerical techniques are available for comparison.

The most positive result of this approach is found in Chapter 3. In this case the experimental geometry has been reduced to one in which only three beams make significant contributions to the diffracted wavefunction intensity. While many others (see Chapter 3 for references) have tried to extract the crystallographic phase information which must be present in this three-beam intensity,

none have resorted to an entirely perturbative approach of the situation in its simplest form. In Chapter 3 it is shown that this approach leads to a prescription whereby crystallographic phase invariants (θ) may be *measured* directly from a convergent-beam electron diffraction pattern. This prescription relies on the inversion of the simplest possible Born expansion of the diffracted amplitudes which gives a phase-preserving three-beam intensity. Such a truncation of a Born expansion would normally be considered too crude to entertain, but with the aid of the full theory it is shown that the method may produce measured values of θ to an accuracy of within $\pm 15°$ in experimentally reasonable circumstances. It is hoped that the method will shortly be tested more thoroughly on a metastable alloy phase of unknown structure (see Exelby and Vincent 1989).

The RHEED example in Chapter 4 has not lead to such a positive result in terms of deducing quantitative information directly from a micrograph. However, RHEED is a considerably more difficult problem than THEED, and many authors have been confused as to the origin of more than one of the features frequently observed in RHEED patterns (again, see the chapter for references). The main result of Chapter 4 is that these features may be understood if perturbation theory is used to simplify the analysis. The selection used to advantage in this case was to analyse a strongly scattering surface [Pt($\bar{1}1\bar{1}$)] so that the features of interest were well separated. The high voltage used in microscopes also made the analysis easier, but was found to produce RHEED patterns which were not particularly surface sensitive. However, it is believed that with better understanding of RHEED patterns produced by this high-voltage work, it may be easier to approach the truly interesting problem in low-voltage RHEED, of

how to extract surface information directly from an experimental pattern.

In the broader view, one of the aims of HEED must be to become a more quantitative, and less visual science. As outlined in Chapter 1, the ability to form small probes in a controlled manner makes electrons potentially useful in this respect. Since HEED is a multi-parameter problem, in which many small, and some not-so-small effects are ignored or not treated properly (see Chapter 2), this movement towards quantification is not easy. Since the inversion of a whole pattern is unlikely to be possible, selective analysis of parts of diffraction patterns would seem to the way to proceed. However, there seems to be a tendency to stick to a proper treatment of the multiple scattering part of the problem. This means that the starting point for most HEED analysis is numerical, and it is difficult to make any quantitative deduction without exclusive use of fitting procedures, in which forward-going theories are compared with experiment, as a function of however many parameters happen to be relevant. It is suggested here that there may often be some reward in pursuing approximation methods when tackling the multiple scattering problem. At the very least such an approach may lead to a better understanding of which parameters *are* relevant; more optimistically it may lead to approximate inversion of the problem, which should simplify subsequent fitting and refinement procedures considerably.

Finally, care should be taken when using approximation methods such as the ones presented here that the "small" effects included as a perturbation are indeed smaller than other effects not included. In this respect it is of considerable use to have a dynamical forward-going theory for comparison which incorporates as many different effects as possible.

REFERENCES

Appelbaum J A. (1975). in *Surface Physics of Materials*,**1**, ed. J M Blakely, Academic, New York, 79.

Ashcroft N W and Mermin N D. (1976). *Solid State Physics*, Holt, Rinehart And Winston, New York.

Bacon G E. (1975). *Neutron Diffraction*, Clarendon, Oxford.

Baker J R. (1982). Ph. D. thesis, University of Bristol.

Berry M V. (1971). J. Phys. C **4**, 697.

Berry M V. (1984). Proc. R. Soc. Lond. **A392**, 45.

Bethe H A. (1928). Ann. Phys. **87**, 55.

Bird D M. (1981). Ph. D. thesis, University of Cambridge.

Bird D M. (1987). Inst. Phys. Conf. Ser. No. 90 (EMAG '87), 119.

Bird D M. (1989). J. Elec. Mic. Tech. **13**, 77.

Bird D M. (1990). Acta Cryst. A. In press.

Bird D M, James R and King Q A. (1989). Phys. Rev. Lett. **63**, 1118.

Bird D M, James R and Preston A R. (1987). Phys. Rev. Lett. **59**, 1216.

Bird D M and James R. (1988). Ultramic. **26**, 31.

Bird D M and King Q A. (1990). Acta Cryst. A. In press.

Bird D M and Preston A R. (1988). Phys. Rev. Lett. **61**, 2863.

Bird D M and Wright A G. (1989) Acta Cryst. **A45**, 104.

Bleloch A L. (1989). Ph. D. thesis, University of Cambridge.

Bradley C R and Zaluzec N J. (1987). in *Analytical Electron Microscopy 1987*, ed. D C Joy, San Francisco Press, 117.

Buxton B F. (1976). Proc. Roy. Soc. London. **A350**, 335.

Buxton B F, Eades J A, Steeds J W and Rackham G M. (1976). Phil. Trans. **281**, 171.

Carpenter R W and Spence J C H. (1984). J. Microsc. **136**, 165.

Cowley J M. (1981). *Diffraction Physics*, 2^{nd} rev. ed. North-Holland, Amsterdam.

Dirac P A M. (1958). *The Principles of Quantum Mechanics*, 4^{th} ed. Clarendon, Oxford.

Dederichs P H. (1972). Solid State Physics **27**, 135.

Doyle P A and Turner P S. (1968). Acta Cryst. **A24**, 390.

Economou E N. (1983). *Green's Functions in Quantum Physics*, Springer-Verlag, Berlin.

Exelby D R and Vincent R. (1989). Inst. Phys. Conf. Ser. No. 98 (EMAG '89), 127.

Fujiwara K. (1961). J. Phys. Soc. Japan **16**, 2226.

Fujiwara K. (1962). J. Phys. Soc. Japan **17**, suppl. **B-II**, 118.

Hall C R and Hirsch P B. (1965). Proc. Roy. Soc. **A286**, 158.

Hart M and Lang A R. (1961). Phys. Rev. Lett. **7**, 120.

Hashimoto H, Howie A and Whelan M J. (1962). Proc. Roy. Soc. London **A269**, 80.

Hirsch P B, Howie A, Nicholson R B, Pashley D W and Whelan M J. (1965). *Electron Microscopy of Thin Crystals*, Butterworths, London.

Høier R and Marthinsen K. (1983). Acta Cryst. **A39**, 854.

Horio Y and Ichimiya A. (1989). Surface Science **219**, 128.

Howie A. (1963). Proc. Roy. Soc. **A271**, 268.
Howie A. (1966). Phil Mag. **14**, 223.
Howie A, Milne R H and Walls M G. (1985). Inst. Phys. Conf. Ser. No. 78 (EMAG '85), 117.
Howie A and Whelan M J. (1961). Proc. Roy. Soc. **A263**, 217.
Humphreys C J. (1979). Rep. Prog. Phys. **42**, 1825.
Humphreys C J and Hirsch P B. (1968). Phil. Mag. **18**, 115.
Ichimiya A. (1983). Jpn. J. Appl. Phys. **22**, 176.
Ichimiya A, Kambe K and Lehmpfuhl G. (1980). J. Phys. Soc. Japan **49**, 684.
Ishizuka K and Taftø J. (1984). Acta Cryst. **B40**, 332.
James R and Bird D M. (1987). Inst. Phys. Conf. Ser. No. 90 (EMAG '87), 131.
James R, Bird D M and Wright A G. (1989). Inst. Phys. Conf. Ser. No. 98 (EMAG '89), 111.
Jones P J, Rackham G M and Steeds J W. (1977). Proc. Roy. Soc. **A354**, 197.
Joyce B A, Neave J H, Zhang J and Dobson P J. (1988). NATO ASI Series **B188**, 397.
Juretschke H J. (1982). Phys. Rev. Lett. **48**, 1487.
Juretschke H J. (1984). Acta Cryst. **A40**, 379.
Juretschke H J. (1986). Acta Cryst. **A42**, 449.
Kambe K. (1957). J. Phys. Soc. Japan **12**, 13.
Kambe K. (1967). Z.Naturforsch. **22a**, 422.
Kästner G. (1987). Acta Cryst **A43**, 683.
Kelly P M, Jostons A, Blake R G and Napier J G. (1975). Phys. Stat. Sol. (a)**31**, 771.
Kikuchi S and Nagakawa S. (1933). Sci. Papers Inst. Phys. Chem. Res. Tokyo, **21**, 256.
Ladd M F C and Palmer R A. (1977). *Structure Determination by X-ray crystallography*, Plenum, New York.
Larsen P K and Dobson P J. (eds.) (1988). *Reflection High-Energy Electron Diffraction and Reflection Electron Imaging of Surfaces*, elsewhere referred to as NATO ASI Series **B188**.
Larsen P K, Dobson P J, Neave J H, Joyce B A, Bolger B and Zhang G. (1986). Surface Science **169**, 176.
Lax M J. (1974). *Symmetry Principles in Solid State and Molecular Physics*, Wiley, New York.
Lehmpfuhl G and Dowell W C T. (1986). Acta Cryst. **A42**, 569.
Lipscomb W N (1949). Acta Cryst. **2**, 193.
Lyon H B and Somorjai G A. (1966). J. Chem. Phys. **44**, 3707.
McRae E G. (1979). Rev. Mod. Phys. **51**, 541.
Maksym P A and Beeby J L. (1981). Surface Science **110**, 423.
Marten H and Meyer-Ehmsen G. (1985). Surface Science **151**, 570.
Marthinsen K and Høier R. (1986). Acta Cryst. **A42**, 484.
Marthinsen K and Høier R. (1988). Acta Cryst. **A44**, 558.
Miyake S, Kohra K and Tagaki M. (1954). Acta Cryst. **7**, 393.
Moodie A F. (1972). Z. Naturforsch. **27a**, 437.
Morabito J M, Steiger R F and Somorjai G A. (1969). Phys. Rev. **179**, 638.
Ohtsuki Y H. (1968). J. Phys. Soc. Japan **25**, 481.
Pendry J B. (1974). *Low Energy Electron Diffraction*, Academic Press, New York.
Peng L M and Cowley J M. (1986). Acta Cryst. **A42**, 545.
Peng L M and Cowley J M. (1987). J. Elec. Mic. Tech. **6**, 43.

Peng L M and Cowley J M. (1988). Surface Science **204**, 555.
Peng L M, Cowley J M and Yao N. (1988). Ultramic. **26**, 189.
Post B and Ladell J. (1987). Acta Cryst. **A43**, 173.
Preston A R. (1987). Private communication.
Radi G. (1970). Acta Cryst. **A26**, 41.
Reid J S. (1983). Acta Cryst. **A39**, 1.
Reimer L. (1985). *Scanning Electron Diffraction*, Springer Series in Optical Sciences, **45**, Springer-Verlag, Berlin.
Riley K F. (1974). *Mathematical Methods for the Physical Sciences*, CUP.
Rodenburg J M. (1989). Ultramic. **27**, 413.
Schiff L I. (1968). *Quantum Mechanics*, 3rd ed., McGraw-Hill.
Shen Q. (1986). Acta Cryst. **A42**, 525.
Shen Q and Collela R. (1986). Acta Cryst. **A42**, 533.
Shen Q and Collela R. (1988). Acta Cryst. **A44**, 17.
Smith G H and Burge R E. (1962). Acta Cryst. **15**, 182.
Steeds J W. (1979). in *Introduction to Analytical Electron Microscopy*, eds, Hren J J, Goldstein J I and Joy D C, Plenum, New York, 387.
Taftø J. (1983). Phys. Rev. Lett. **51**, 654.
Taftø J. (1987). Acta Cryst. **A43**, 208.
Tanaka M, Saito R, Ueno K and Harada Y. (1980). J. Electron Microscopy **20**, 408.
Thorkildsen G. (1987). Acta Cryst. **A43**, 361.
Uchida Y, Lehmpfuhl G and Jaeger J. (1984). Ultramic. **15**, 576.
Vincent R and Bird D M. (1986). Phil. Mag. **A53**, L35.
Vincent R, Bird D M and Steeds J W. (1984a). Phil. Mag. **A50**, 745.
Vincent R, Bird D M and Steeds J W. (1984b). Phil. Mag. **A50**, 765.
Wang Z L. (1988). Ultramic. **26**, 321.
Wang Z L and Cowley J M. (1988). Surface Science **193**, 501.
Wang Z L and Egerton R F. (1988). Surface Science **205**, 25.
Wang Z L, Liu J, Ping Lu and Cowley J M. (1989). Ultramic. **27**, 101.
Wang Z L, Ping Lu and Cowley J M. (1987). Ultramic. **23**, 205.
Wilkinson J H. (1965). *The Algebraic Eigenvalue Problem*, OUP.
Woolfson M M. (1971). Rep. Prog. Phys. **34**, 369.
Wright A G. (1989) Private communication.
Yao N and Cowley J M. (1989). Ultramic. **31**, 149.
Yoshioka H. (1957). J. Phys. Soc. Japan **12**, 618.
Zhao T C, Poon H C and Tong S Y. (1988). Phys. Rev. **B38**, 1172.
Zhao T C and Tong S Y. (1988). Ultramic. **26**, 151.
Zuo J M, Spence J C H and Høier R. (1989). Phys. Rev. Lett. **62**, 547.
Zuo J M, Spence J C H and O'Keefe M. (1988). Phys. Rev. Lett. **61**, 353.